# NUMERICAL MODELING OF INTERTIDAL MUDFLAT PROFILE EVOLUTION UNDER WAVES AND CURRENTS

by

PATERNO S. MIRANDA AND NOBUHISA KOBAYASHI

RESEARCH REPORT NO. CACR-22-01

SPRING 2022

CENTER FOR APPLIED COASTAL RESEARCH
COASTAL ENGINEERING LABORATORY

University of Delaware
Newark, Delaware 19716

## ACKNOWLEDGMENTS

This study was supported in part by the Philippine-American Educational Foundation (Fulbright Commission in the Philippines). The extension of CSHORE capabilities was partially supported by the US Army Corps of Engineers under Agreement No. W912HZ18P0134.

## TABLE OF CONTENTS

LIST OF TABLES ..... v
LIST OF FIGURES ..... vi
ABSTRACT ..... xii

1 INTRODUCTION ..... 1

2 FIELD DATA ..... 4

2.1 Bed Level Monitoring ..... 4
2.2 Available Oceanographic and Meteorological Data ..... 7
2.3 Mudflat Profile Variation ..... 8

3 NUMERICAL MODEL ..... 17

3.1 Extension of CSHORE to Mudflat ..... 17
3.2 Computation Procedure ..... 23

4 COMPARISON WITH DATA ..... 27

4.1 Erosion interval ..... 27

4.1.1 Base case of equivalent alongshore distance $y_e$ = 100 m ..... 28
4.1.2 Alongshore uniform case of IQYDY = 0 ..... 39
4.1.3 Profile change sensitivity to increased $y_e$ = 200 m ..... 44

4.2 Accretion interval ..... 49

4.2.1 Base case of equivalent alongshore distance (-$y_e$) = 100 m ..... 50
4.2.2 Alongshore uniform case of IQYDY = 0 ..... 60
4.2.3 Profile change sensitivity to increased (-$y_e$) = 200 m ..... 65

5 SENSITIVITY OF COMPUTED RESULTS ..... 70

5.1 Mud Characteristics and Volume Fraction ..... 70
5.2 Tide Amplitudes $A_y$ and $A_t$ ..... 76
5.3 Wave Height, Period, and Direction ..... 83

6 OTHER EFFECTS ON MUDFLAT PROFILE CHANGES ..... 94

6.1 Initial Profile Shape ..... 94
6.2 Alongshore Water Level Gradient ..... 97
6.3 Wind Shear Stresses ..... 100

7 CONCLUSIONS ..... 103

REFERENCES ..... 106

## LIST OF TABLES

Table 2.1: Fitted Parameters for Measured Profiles during Erosion Interval..... 9

Table 2.2: Fitted Parameters for Measured Profiles during Accretion Interval ..... 10

Table 2.3: Eroded Area and Average Erosion Depth for $x = 1{,}950 - 2{,}900$ m during Erosion Interval (negative for accretion) ..... 14

Table 2.4: Accreted Area and Average Accreted Depth for $x = 1{,}950 - 2{,}900$ m during Accretion Interval ..... 16

Table 3.1: Basic input values for Erosion (E) and Accretion (A) Intervals ..... 25

## LIST OF FIGURES

Figure 2.1: Ariake Bay in Kyushu Island, Japan ..... 5

Figure 2.2: Surveyed profile from the seawall in Ariake Bay at the mouth of Shirakawa River..... 6

Figure 2.3: Three fitted and extrapolated profiles on 03 July 2001, 25 January 2002, and 08 August 2002 together with three water levels measured at field site ..... 11

Figure 2.4: Fitted mudflat profiles at the start and end of the Erosion and Accretion intervals (top). Elevation changes after each interval (bottom) ..... 12

Figure 2.5: Elevation changes during Erosion interval ..... 13

Figure 2.6: Temporal change of eroded area (negative eroded area for accretion) ..... 14

Figure 2.7: Elevation changes during Accretion interval ..... 15

Figure 2.8: Temporal change of accreted area..... 16

Figure 3.1: Adopted horizontal coordinate system $x, y$ and incident wave angle, $\theta$ ... 17

Figure 4.1: Time series of water level assumed for Erosion (E) interval of 206 days. 27

Figure 4.2: Hourly cross-shore variation of mean water depth ($h$), significant wave height ($H_{m0}$), mean ($U$) and standard deviation ($\sigma_U$) of cross-shore velocity ($U$) at beginning of E interval ..... 32

Figure 4.3: Hourly cross-shore variation of $\sin\theta$ ($\theta$ = wave angle), mean ($V$) and standard deviation ($\sigma_V$) of longshore velocity ($V$) at beginning of E interval..... 33

Figure 4.4: Hourly cross-shore variation of cross-shore sediment transport rate ($q_x$) and longshore sediment transport rate ($q_y$) at the beginning of E interval..... 34

Figure 4.5: Cross-shore variation of cumulative sediment transport volumes $v_x$ and $v_y$ calculated by integrating $q_x$ and $q_y$ from time $t$ = 0 to $t$ = 64, 109, 122, 150, 177, and 206 days during E interval ..... 35

Figure 4.6: Comparison of fitted and computed mudflat profiles relative to initial profile at $t$ = 64, 109, 122, 150, 177 and 206 days during E interval..... 36

Figure 4.7: Deviation of computed mudflat profile from fitted profile at time $t$ = 64, 109, 122, 150, 177 and 206 days during E interval ..... 37

Figure 4.8: Comparison of fitted and computed eroded areas during E interval..... 38

Figure 4.9: Cross-shore variation of cumulative sediment transport volumes $v_x$ and $v_y$ during E interval for alongshore uniform case of IQYDY = 0..... 40

Figure 4.10: Comparison of fitted and computed mudflat profiles relative to initial profile during E interval for alongshore uniform case of IQYDY = 0 ... 41

Figure 4.11: Deviation of computed mudflat profile from fitted profile at given time during E interval for alongshore uniform case of IQYDY = 0 ..... 42

Figure 4.12: Comparison of fitted and computed eroded areas (negative implies net accretion) during E interval for alongshore uniform case of IQYDY = 0..... 43

Figure 4.13: Cross-shore variation of cumulative sediment transport volumes $v_x$ and $v_y$ during E interval for increased $y_e$ = 200 m..... 45

Figure 4.14: Comparison of fitted and computed mudflat profiles relative to initial profile during E interval for increased $y_e$ = 200 m..... 46

Figure 4.15: Deviation of computed mudflat profile from fitted profile at given time during E interval for increased $y_e$ = 200 m..... 47

Figure 4.16: Comparison of fitted and computed eroded areas (negative implies net accretion) during E interval for increased $y_e$ = 200 m..... 48

Figure 4.17: Time series of water level assumed for Accretion (A) interval of 195 days..... 49

Figure 4.18: Hourly cross-shore variation of mean water depth ($h$), significant wave height ($H_{m0}$), mean ($U$) and standard deviation ($\sigma_U$) of cross-shore velocity ($U$) at beginning of A interval..... 53

Figure 4.19: Hourly cross-shore variation of $\sin\theta$ ($\theta$ = wave angle), mean ($V$) and standard deviation ($\sigma_V$) of longshore velocity ($V$) at beginning of A interval..... 54

Figure 4.20: Hourly cross-shore variation of cross-shore sediment transport rate ($q_x$) and longshore sediment transport rate ($q_y$) at the beginning of A interval ..... 55

Figure 4.21: Cross-shore variation of cumulative sediment transport volumes $v_x$ and $v_y$ calculated by integrating $q_x$ and $q_y$ from time $t$ = 0 to $t$ = 32, 61, 90, 167, and 195 days during A interval ..... 56

Figure 4.22: Comparison of fitted and computed mudflat profiles relative to initial profile at $t$ = 32, 61, 90, 167 and 195 days during A interval ..... 57

Figure 4.23: Deviation of computed mudflat profile from fitted profile at time $t$ = 32, 61, 90, 167 and 195 days during A interval ..... 58

Figure 4.24: Comparison of fitted and computed eroded areas during A interval ..... 59

Figure 4.25: Cross-shore variation of cumulative sediment transport volumes $v_x$ and $v_y$ during A interval for alongshore uniform case of IQYDY = 0 ... 61

Figure 4.26: Comparison of fitted and computed mudflat profiles relative to initial profile during A interval for alongshore uniform case of IQYDY = 0 ... 62

Figure 4.27: Deviation of computed mudflat profile from fitted profile at given time during A interval for alongshore uniform case of IQYDY = 0 ..... 63

Figure 4.28: Comparison of fitted and computed accreted areas (negative implies net erosion) during A interval for alongshore uniform case of IQYDY = 0 ..... 64

Figure 4.29: Cross-shore variation of cumulative sediment transport volumes $v_x$ and $v_y$ during A interval for increased (-$y_e$) = 200 m ..... 66

Figure 4.30: Comparison of fitted and computed mudflat profiles relative to initial profile during A interval for increased (-$y_e$) = 200 m ..... 67

Figure 4.31: Deviation of computed mudflat profile from fitted profile at given time during A interval for increased (-$y_e$) = 200 m ..... 68

Figure 4.32: Comparison of fitted and computed accreted areas during A interval for increased (-$y_e$) = 200 m ..... 69

Figure 5.1: Comparison of fitted and computed eroded areas (negative implies net accretion) during E interval (top) and accreted areas during A interval (bottom) for mud fall velocity $w_e$ = 0.2 and 0.4 mm/s ..... 72

Figure 5.2: Deviation of computed mudflat profile from fitted profile at time $t$ = 64, 109, 122, 150, 177 and 206 days during E interval (top) and time $t$ = 32, 61, 90, 167 and 195 days during A interval (bottom) for $w_e$ = 0.4 mm/s..... 73

Figure 5.3: Comparison of fitted and computed eroded areas (negative implies net accretion) during E interval (top) and accreted areas during A interval (bottom) for mud volume fraction $f_m$ = 0.3 and 0.7..... 74

Figure 5.4: Deviation of computed mudflat profile from fitted profile at time $t$ = 64, 109, 122, 150, 177 and 206 days during E interval (top) and time $t$ = 32, 61, 90, 167 and 195 days during A interval (bottom) for $f_m$ = 0.3..... 75

Figure 5.5: Time series of water level assumed for both E (top) and A (bottom) intervals with yearly water level variation, $A_y$, = 0..... 77

Figure 5.6: Comparison of fitted and computed eroded areas (negative implies net accretion) during E interval (top) and accreted areas during A interval (bottom) for yearly amplitudes $A_y$ = 0.0 and 0.2 m..... 78

Figure 5.7: Deviation of computed mudflat profile from fitted profile at time $t$ = 64, 109, 122, 150, 177 and 206 days during E interval (top) and time $t$ = 32, 61, 90, 167 and 195 days during A interval (bottom) for $A_y$ = 0.0 m..... 79

Figure 5.8: Time series of water level assumed for both E (top) and A (bottom) intervals with semidiurnal amplitude $A_t$ = 0.72 m..... 80

Figure 5.9: Comparison of fitted and computed eroded areas (negative implies net accretion) during E interval (top) and accreted areas during A interval (bottom) for semidiurnal amplitudes $A_t$ = 0.72 and 1.44 m..... 81

Figure 5.10: Deviation of computed mudflat profile from fitted profile at time $t$ = 64, 109, 122, 150, 177 and 206 days during E interval (top) and time $t$ = 32, 61, 90, 167 and 195 days during A interval (bottom) for $A_t$ = 0.72 m..... 82

Figure 5.11: Comparison of fitted and computed eroded areas (negative implies net accretion) during E interval (top) and accreted areas during A interval (bottom) for wave height $H_{m0}$ = 0.1, 0.2 and 0.3 m..... 85

Figure 5.12: Deviation of computed mudflat profile from fitted profile at time $t$ = 64, 109, 122, 150, 177 and 206 days during E interval for $H_{m0}$ = 0.1 and 0.3 m ..... 86

Figure 5.13: Deviation of computed mudflat profile from fitted profile at time $t$ = 32, 61, 90, 167 and 195 days during A interval for $H_{m0}$ = 0.1 and 0.3 m ..... 87

Figure 5.14: Comparison of fitted and computed eroded areas (negative implies net accretion) during E interval (top) and accreted areas during A interval (bottom) for wave period $T_p$ = 2, 3 and 4 s ..... 88

Figure 5.15: Deviation of computed mudflat profile from fitted profile at time $t$ = 64, 109, 122, 150, 177 and 206 days during E interval for $T_p$ = 2, and 4 s ..... 89

Figure 5.16: Deviation of computed mudflat profile from fitted profile at time $t$ = 32, 61, 90, 167 and 195 days during A interval for $T_p$ = 2, and 4 s .. 90

Figure 5.17: Comparison of fitted and computed eroded areas (negative implies net accretion) during E interval (top) and accreted areas during A interval (bottom) for wave angle $\theta$ = 15°, 30°, 45°, and 60° ..... 91

Figure 5.18: Deviation of computed mudflat profile from fitted profile at time $t$ = 64, 109, 122, 150, 177 and 206 days during E interval for $\theta$ = 15°, 45°, and 60° ..... 92

Figure 5.19: Deviation of computed mudflat profile from fitted profile at time $t$ = 32, 61, 90, 167 and 195 days during A interval for $\theta$ = 15°, 45°, and 60° ..... 93

Figure 6.1: Convex initial profile with positive $a$ on 3 July 2001 for E (top) and 25 January 2002 for A (bottom) intervals and hypothetical concave profile with negative $a$ for same elevation at $x$ = 0 and 3,000 m..... 95

Figure 6.2: Computed mudflat elevation changes relative to the initial convex and concave profile at the end of the E (top) and A (bottom) intervals ..... 96

Figure 6.3: Computed mudflat elevation changes relative to the initial profile at the end of the E (top) and A (bottom) intervals for two cases of IAWLG = 0 and 1 ..... 98

Figure 6.4: Deviation of computed final mudflat profile from fitted final profile at the end of E (top) and A (bottom) intervals for IAWLG = 0 and 1..... 99

Figure 6.5: Computed mudflat elevation changes relative to the initial profile at the end of the E (top) and A (bottom) intervals for IWIND = 0 and 1.....101

Figure 6.6: Deviation of computed final mudflat profile from fitted final profile at the end of E (top) and A (bottom) intervals for IWIND = 0 and 1.....102

## ABSTRACT

The erosion and accretion profile changes in an intertidal mudflat were examined using available data and the numerical model CSHORE which was extended for a mixture of sand and mud. The semidiurnal migration of the still water shoreline and surf zone was solved numerically to predict the net cross-shore and longshore sediment transport rates influenced by the small cross-shore (undertow) and longshore currents induced by breaking waves of about 0.2 m. Approximating alongshore sediment gain or loss was observed to be critical to calibration. The alongshore sediment transport gradient utilized an equivalent alongshore length.

The calibrated CSHORE reproduced the erosion and accretion profile changes during their respective intervals. The profile changed about 0.1 m for both intervals over a cross-shore distance of 950 m.

The mudflat profile changes were equally affected by mud characteristics, semi-diurnal tide amplitude, and incident wave height, period, and direction. In addition, profile shape, alongshore water level gradient, and wind stress influenced longshore current and sediment transport.

This study shows the importance of sediment transport in the surf zone which may have been excluded from previous numerical modeling.

# Chapter 1

# INTRODUCTION

Mudflat morphology is a complex phenomenon whose mechanics are still poorly understood compared with sand beach morphology. Mudflats are composed of a mixture of sand and mud. Sandy beach morphology has been well-studied and is driven by breaking waves and wave-induced currents (Kobayashi 2016). Erosion on a sandy beach by severe storms are more pronounced. In contrast, mudflat morphology using erosion and deposition rates published by the US Army Corp of Engineers (USACE 2003) is based on empirical parameters. Mudflats are typically observed in estuaries with small waves where they are affected by tidal range and current, wind waves and wave-induced currents, and river discharge.

A mudflat is characterized by a convex-upward cross-shore profile (Friedrichs and Aubrey 1996). This formation is largely due to the cross-shore tidal current associated with tidally varying shoreline. The profile shape is in contrast to the concave-upward cross-shore profile in sandy beaches (Dean and Dalrymple 2001). The mudflat profile evolution is slow and cumulative thus the prediction requires long-term simulations (Roberts et al. 2000).

Research using 3D ocean models have been used to predict fluvial sediment dispersion by waves and currents (Harris et al. 2008; Uzaki and Kuriyama 2009). These regional models did not include prediction at the intertidal zone.

Numerical models to predict profile evolution in harbors and navigation channels have also been done. These models neglected wind waves in estuaries (Giardino et al. 2009) or excluded the intertidal zone (McAlpin et al. 2019).

Shi (2017) conducted field measurements on intertidal mudflats for 6 days to observe erosion and accretion in shallow water (less than 0.2 m) stages. However, a water depth of 0.2 m only accounted for 11% of the entire tidal cycle and their study found that 35% of the bathymetric changes occurred when the water depth was less than 0.2 m.

The intertidal mudflat profile changes were first investigated using the field data of Yamada and Kobayashi (2003), and the cross-shore numerical model CSHORE (Kobayashi 2016). CSHORE was extended for a mixture of sand and mud. The numerical model was used to predict the movement of sand and mud in the cross-shore and longshore direction within the surf zone. Specifically, mud transport was assessed to determine its contribution to mudflat profile evolution.

Mudflat profile changes are small in magnitude. However, due to the gentle slope of a convex-upward profile, profile changes occur over a large width. The total volume eroded or accreted per unit width is significant despite incremental changes in bed elevation.

The following chapters present and explain the field data, the extension to numerical model CSHORE, and the computational procedure. An alongshore equivalent length parameter (Zhu and Kobayashi 2021) in CSHORE associated with longshore gain or loss was used to calibrate the erosion and accretion observed in the measured data. Sensitivity of the model to changes in mud parameters, tide amplitudes, and wave parameters were summarized and presented. The results

quantified the degree of importance for each input parameter and variable. Similarly, other sensitivity checks were performed to examine the effects of a different initial profile shape, an alongshore water level gradient, and wind shear stress which were neglected for the CSHORE comparison with measured data. The findings of the study were then summarized.

# Chapter 2

# FIELD DATA

## 2.1 Bed Level Monitoring

As presented in Fig. 2.1, the field site of Yamada and Kobayashi (2004) is located at the center of the eastern coast in the Ariake Bay of Kyushu Island, Japan. The enclosed bay has length, width, and depth of approximately 100 km, 20 km, and 20 m, respectively.

The cross-shore survey was performed using 30 wooden stakes driven into the mudflat at 50 m interval (Fig. 2.2). The survey was performed using an electric total station placed at a fixed point on the crest of the seawall adjacent to the Shirakawa River mouth. The mudflat elevations were recorded almost monthly during low tide between February 2001 to December 2002. The measurements could always be taken at the survey points between 100 m and 1,050 m from the seawall. Outside of this range, the mudflats were sometimes too soft.

Sediment characteristics were obtained by collecting six core samples and later using a seismic method (Yamada et al. 2012). Within 2 m of the mudflat surface, the sediment was composed of a mixture of sand and mud. Its characteristics were fairly uniform possibly due to bioturbation.

Mud was defined as sediment (silt and clay) whose median size was smaller than 0.075 mm (Yamada and Kobayashi 2004). The bulk density of the mixed sediment was 1,300 $\mathrm{kg/m^3}$. The sand mass, mud mass, and water mass per unit

volume of the mixed sediment were 400 $\mathrm{kg/m^3}$, 400 $\mathrm{kg/m^3}$, and 500 $\mathrm{kg/m^3}$, respectively. The mixed sediment had a porosity $n_p$ of 0.5.

The sand density, median diameter, and fall velocity were 2,800 $\mathrm{kg/m^3}$, 0.17 mm, and 2 $\mathrm{cm/s}$, respectively. The mud density including organic matter was approximately 1,200 $\mathrm{kg/m^3}$. However, similar to previous numerical modeling of this field site (Uzaki and Kuriyama 2009), the mud fall velocity was not measured by Yamada and Kobayashi (2004).

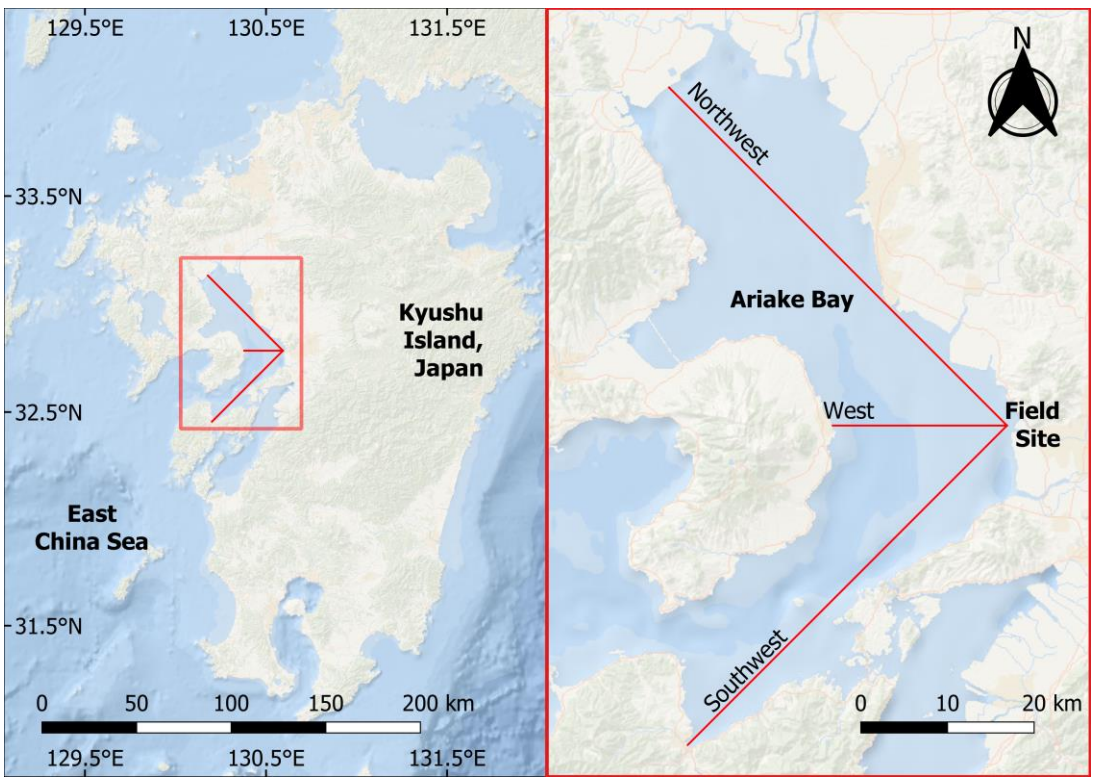


Figure 2.1: Ariake Bay in Kyushu Island, Japan

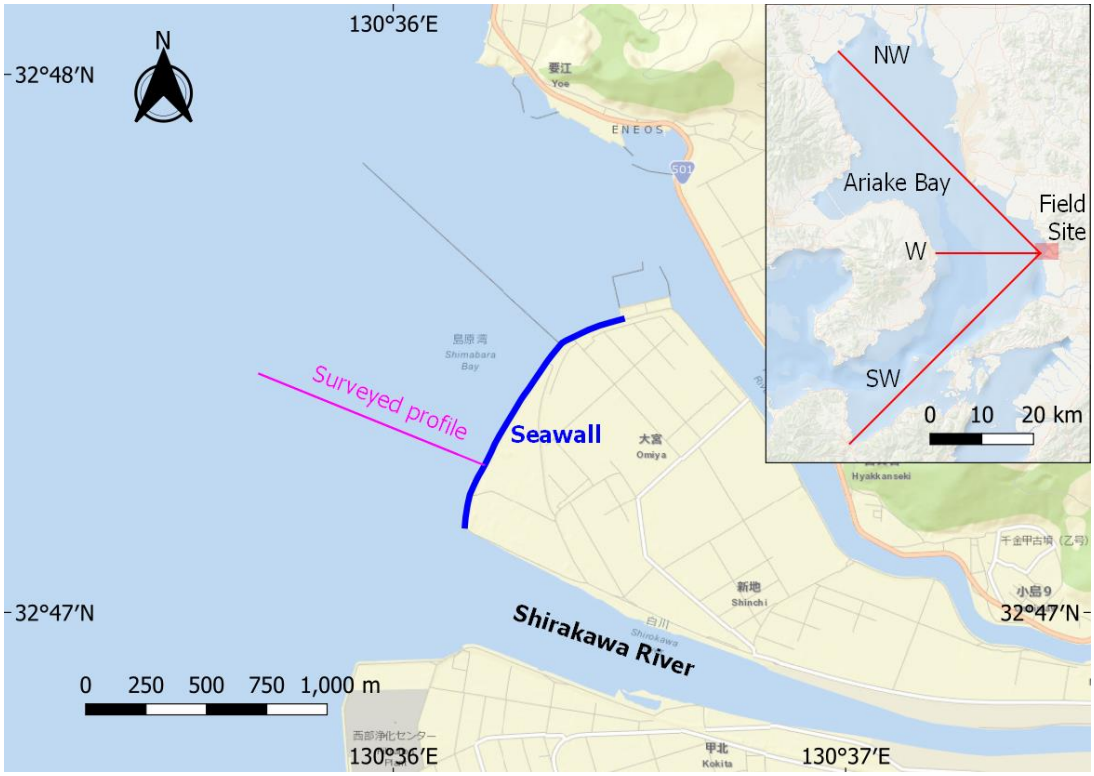


Figure 2.2: Surveyed profile from the seawall in Ariake Bay at the mouth of Shirakawa River

## 2.2 Available Oceanographic and Meteorological Data

The field site was selected because of its proximity to an observation tower at Kumamoto Port. The observation tower is 4 km south of the surveyed profile in Fig. 2.2 and is at a depth of 6.45 m below the Japanese datum.

The water level was measured hourly. The tide is semidiurnal with an average tidal range of 2.88 m and an average water level of 0.14 m above datum. The moving average water level using an averaging duration of 56 days revealed a yearly oscillation of 0.4 m. This showed that water levels were higher during the summer than they were during the winter.

Wind waves were measured every two hours using an ultrasonic wave gauge at the observation tower. The average significant wave height and period were 0.2 m and 3 s, respectively. Small wave heights are expected since fetch lengths are limited (less than 60 km based on Fig 2.1) in a shallow enclosed bay such as Ariake bay. Wave directions were not measured by the ultrasonic wave gauge.

The wind speed and direction were measured hourly using an anemometer at the observation tower. The average wind speed $W_{10}$ at 10 m elevation and dominant wind direction were approximately 5 $\mathrm{m/s}$ and northwest direction, respectively. The dominant wave direction was assumed to be the same as the dominant wind direction in this study.

## 2.3 Mudflat Profile Variation

The measured mudflat elevation $z_b$ above the datum was represented using the following quadratic equation

$$z_b(t,x) = -a(t)(x_s - x)^2 - b(t)(x_s - x) + c(t) \quad (1)$$

where $t$ = morphological time; $x$ = onshore coordinate; $x_s$ = onshore location of the seawall; $a$ = convexity parameter; and $c$ = toe elevation of the seawall. The origin of the onshore coordinate $x$ was taken as the seaward boundary where the time series of the water level and incident waves were specified as input. The measured and fitted profiles for $(x_s - x)$ = 100 – 1,050 m agreed within an error of 3 cm (Yamada and Kobayashi 2003) which was slightly larger than the survey error of 2 cm. The fitted profile was assumed to represent the measured profile and this assumption facilitates the profile extrapolation and integration.

Tables 2.1 and 2.2 list the fitted values of $a$, $b$, and $c$ for the profiles measured between 03 July 2001 and 08 August 2002. During this period, two intervals were determined. The first was from 03 July 2001 (summer) to 25 January 2002 (winter) and the second was from 25 January 2002 (winter) to 08 August 2002 (summer). The fitted profiles were extrapolated to the water depth corresponding to that of the observation tower. The origin of the onshore coordinate was selected so that the location of the seawall was at $x_s$ = 3,000 m and the water depth at the origin was at $z_b$ = -6.3 or -6.4 m on 03 July 2001 and 25 January 2002, respectively. These initial profiles were used in the subsequent computation.

The fitted profiles of 03 July 2001, 25 January 2002, and 08 August 2002 are presented in Fig. 2.3. The change in profile after the first interval (03 July 2001 to 25 January 2002) exhibited an erosion period while the change in the profile after the

second interval (25 January 2002 to 08 August 2002) presented an accretion period. The seasonal elevation change in the order of 0.1 m was in phase with a yearly water level change of 0.4 m.

Fig. 2.3 also presents tidal statistics at the field site. Specifically, the mean monthly highest and lowest water levels, and the average water level above the datum are +2.05 m, -2.45 m, and +0.14 m, respectively. These water levels indicate the tidal range in Ariake Bay. The seawall crest is located at an elevation of 4 m and no wave overtopping occurred during 2001-2002.

An analysis of the fitted profiles' evolution was limited to the zone where the profiles were measured, $x$ = 1,950 – 2,900 m. Generally, the profile changes at the end of the two intervals were larger at the seaward end ($x$ = 1,950 m) than at the landward end ($x$ = 2,900 m). This is evident in Fig. 2.4 where the profile changes after the two intervals are presented and compared.

Table 2.1: Fitted Parameters for Measured Profiles during Erosion Interval

| **Date** | **No. of days** | $\boldsymbol{a} \times \mathbf{10^7(m^{-1})}$ | $\boldsymbol{b} \times \mathbf{10^3(-)}$ | $\boldsymbol{c} \times \mathbf{10(m)}$ |
|---|---|---|---|---|
| **03 July 2001** | 0 | 4.37 | 0.92 | 3.77 |
| **05 September 2001** | 64 | 2.97 | 1.09 | 4.24 |
| **20 October 2001** | 109 | 2.15 | 1.18 | 4.31 |
| **02 November 2001** | 122 | 3.25 | 1.12 | 4.49 |
| **30 November 2001** | 150 | 2.30 | 1.29 | 4.68 |
| **27 December 2001** | 177 | 4.50 | 1.08 | 3.93 |
| **25 January 2002** | 206 | 3.80 | 1.12 | 3.96 |

Table 2.2: Fitted Parameters for Measured Profiles during Accretion Interval

| **Date** | **No. of days** | $\boldsymbol{a} \times \mathbf{10^7}(\mathbf{m^{-1}})$ | $\boldsymbol{b} \times \mathbf{10^3}(-)$ | $\boldsymbol{c} \times \mathbf{10}(\mathbf{m})$ |
|---|---|---|---|---|
| **25 January 2002** | 0 | 3.80 | 1.12 | 3.96 |
| **26 February 2002** | 32 | 3.83 | 1.08 | 4.28 |
| **27 March 2002** | 61 | 2.48 | 1.20 | 4.25 |
| **25 April 2002** | 90 | 4.55 | 0.98 | 3.87 |
| **11 July 2002** | 167 | 3.05 | 1.09 | 4.23 |
| **08 August 2002** | 195 | 3.86 | 0.93 | 4.14 |

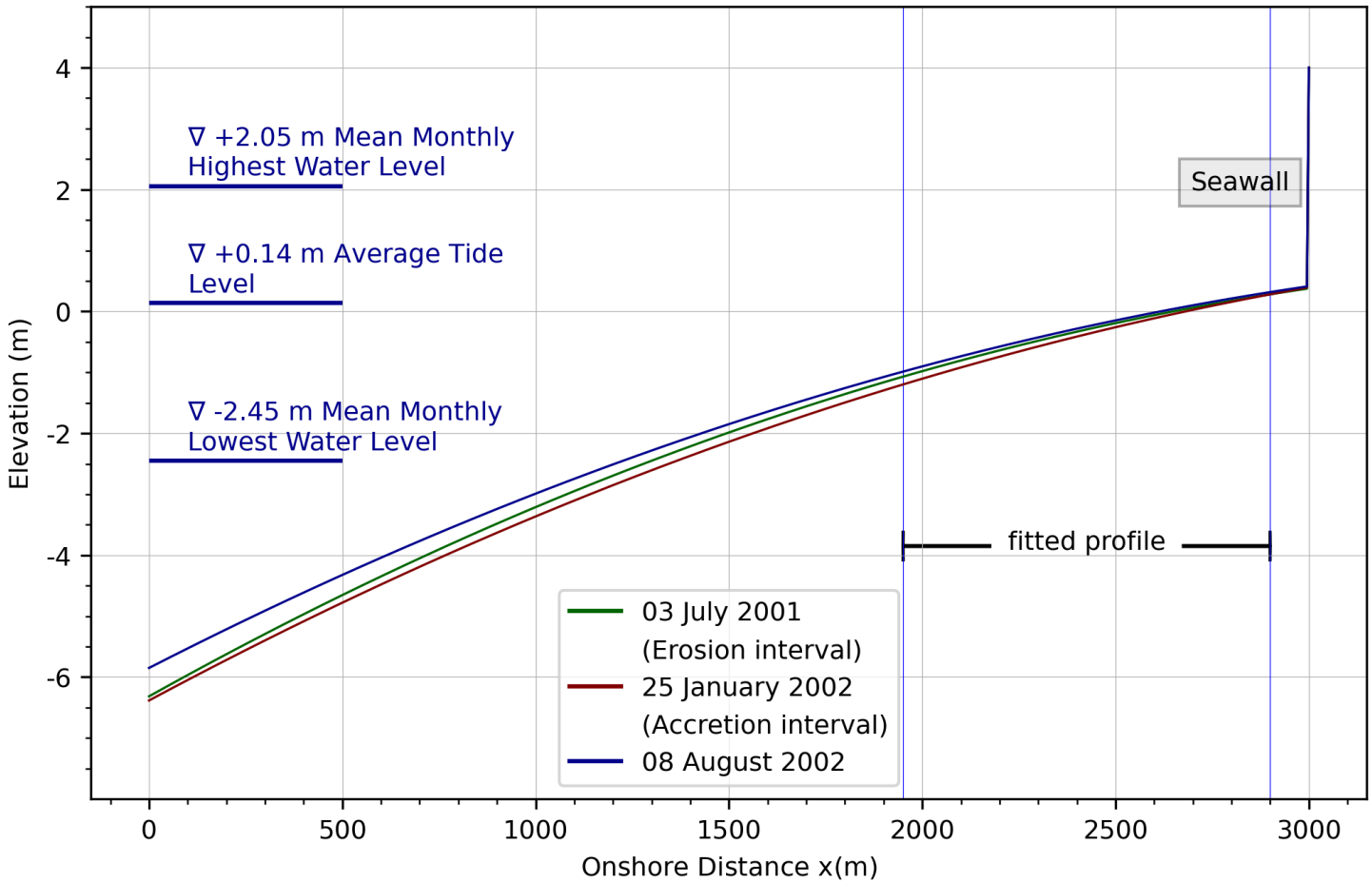


Figure 2.3: Three fitted and extrapolated profiles on 03 July 2001, 25 January 2002, and 08 August 2002 together with three water levels measured at field site

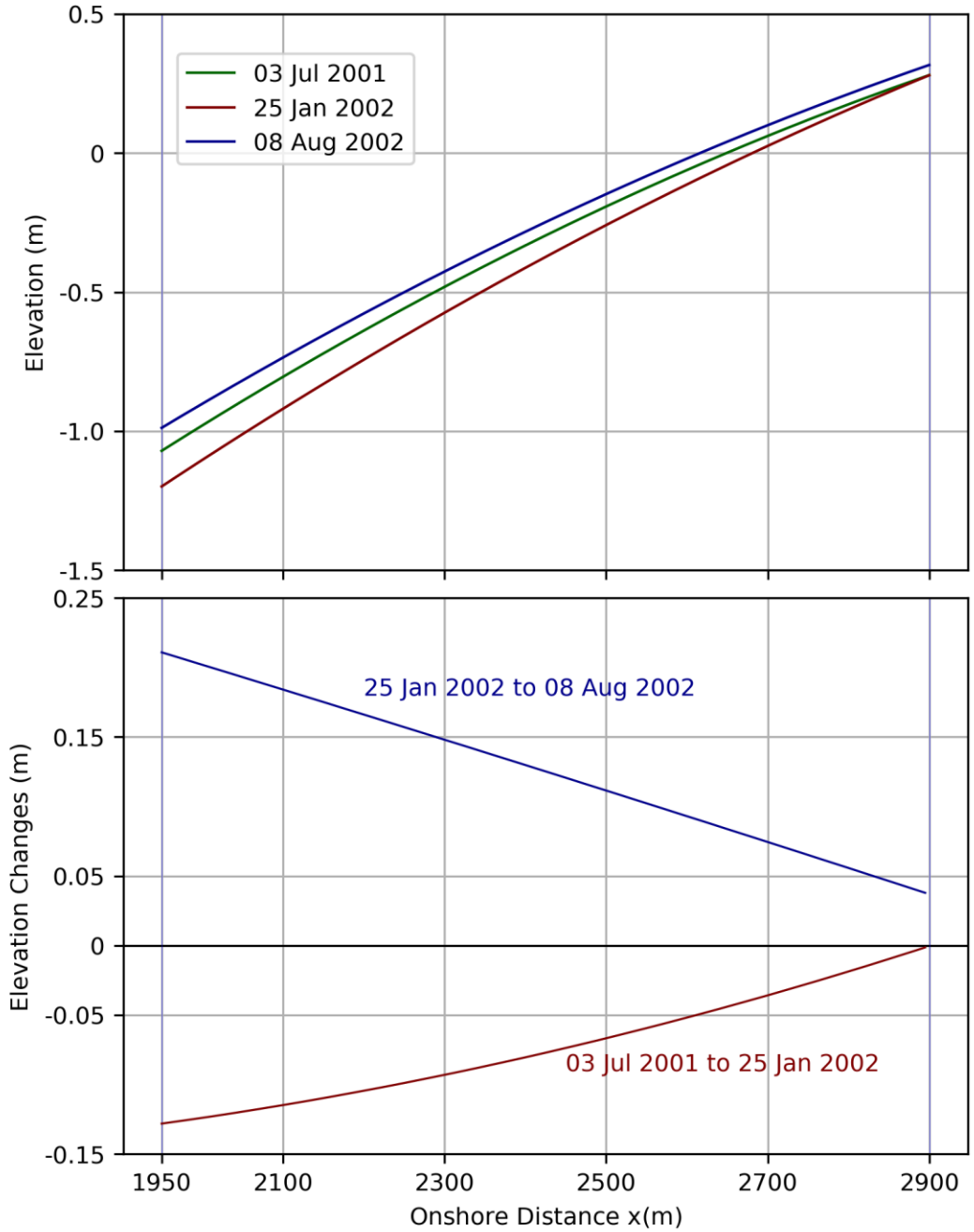


Figure 2.4: Fitted mudflat profiles at the start and end of the Erosion and Accretion intervals (top). Elevation changes after each interval (bottom)

For the erosion interval, seven profiles are available including the initial profile on 03 July 2001 and the final profile on 25 January 2002. The changes in mudflat elevation from the initial profile are shown in Fig. 2.5. The profiles, identified by their survey date and number of days since 03 July 2001, show the evolution during the interval of 206 days.

Table 2.3 and Fig. 2.6 present the temporal erosion area within the zone of the measured profile. Relatively small profile changes and even some accretion was observed until 150 days. Negative elevation changes became conspicuous after 177 days. The average erosion depths were also estimated in Table 2.3. Although an erosion depth of about 0.1 m was small, the eroded area was as large as 77 $m^2$ across the cross-shore distance of 950 m on 27 December 2001.

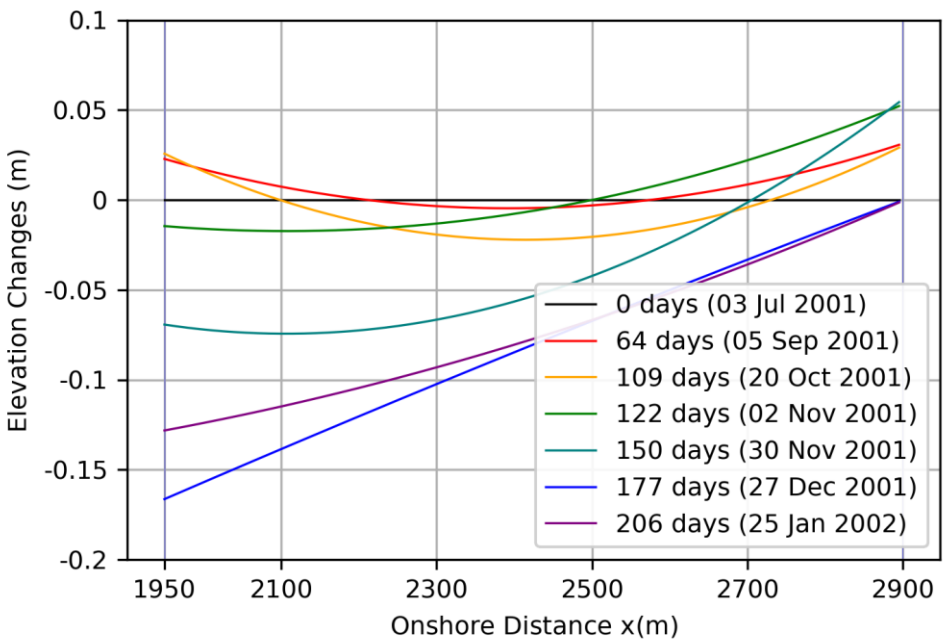


Figure 2.5: Elevation changes during Erosion interval

Table 2.3: Eroded Area and Average Erosion Depth for $x = 1{,}950 - 2{,}900$ m during Erosion Interval (negative for accretion)

| Date | Time (Days) | Eroded area $(\mathbf{m^2})$ | Erosion Depth $(\mathbf{m})$ |
|---|---|---|---|
| **03 Jul 2001** | 0 | 0 | 0 |
| **05 Sep 2001** | 64 | -5.9 | -0.006 |
| **20 Oct 2001** | 109 | 5.0 | 0.005 |
| **02 Nov 2001** | 122 | -2.6 | -0.003 |
| **30 Nov 2001** | 150 | 35.6 | 0.037 |
| **27 Dec 2001** | 177 | 77.2 | 0.081 |
| **25 Jan 2002** | 206 | 69.2 | 0.073 |

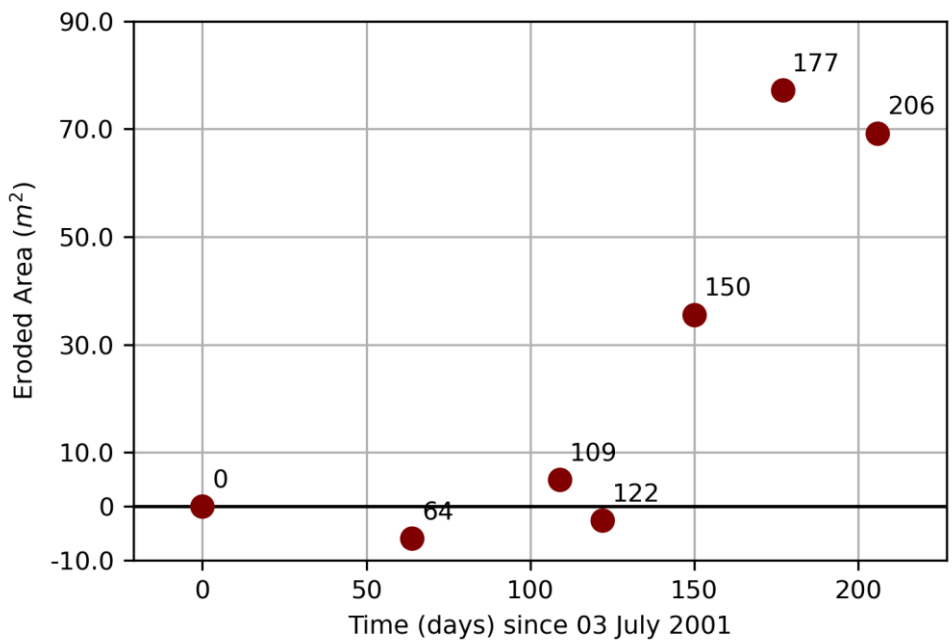


Figure 2.6: Temporal change of eroded area (negative eroded area for accretion)

For the accretion interval, six profiles are available including the initial profile on 25 January 2002 and the final profile on 08 August 2002. The changes in mudflat elevation from the initial profile are shown in Fig. 2.7. The profiles, similarly identified by their survey date and number of days since 25 January 2002, show the evolution during the interval of 195 days.

Table 2.4 and Fig. 2.8 present the temporal accretion area within the zone of the measured profile. The average mudflat elevation increased after 32 days and decreased marginally in March then accretion resumed. The accreted area was at 119 $m^2$ at the end of the accretion interval with the accretion height exceeding 0.2 m at the seaward boundary of the measured zone.

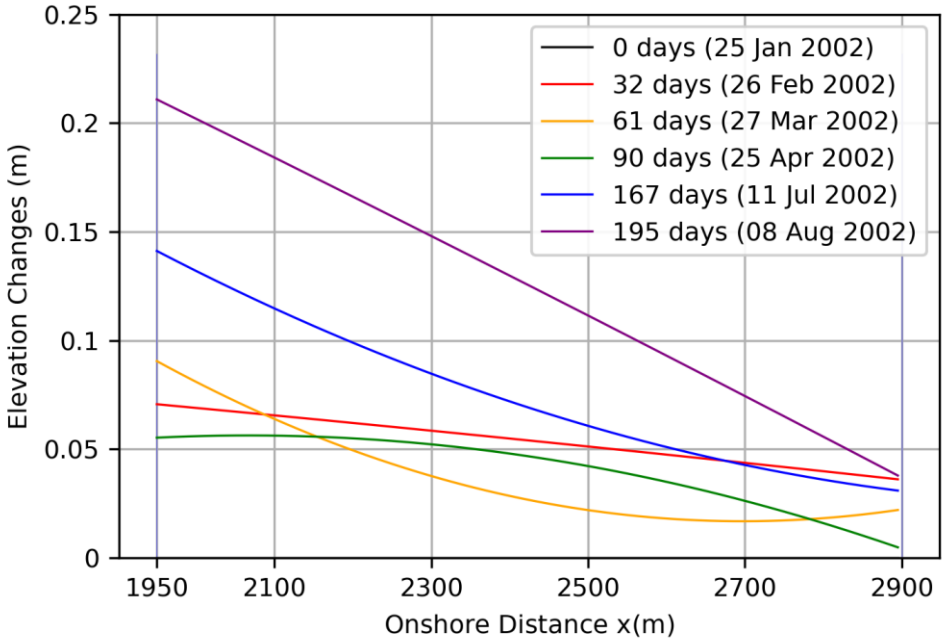


Figure 2.7: Elevation changes during Accretion interval

Table 2.4: Accreted Area and Average Accreted Depth for $x = 1{,}950 - 2{,}900$ m during Accretion Interval

| Date | Time (Days) | Accreted Area $(\mathbf{m^2})$ | Accreted Depth $(\mathbf{m})$ |
|---|---|---|---|
| **25 Jan 2002** | 0 | 0 | 0 |
| **26 Feb 2002** | 32 | 51.3 | 0.054 |
| **27 Mar 2002** | 61 | 34.9 | 0.037 |
| **25 Apr 2002** | 90 | 39.0 | 0.041 |
| **11 Jul 2002** | 167 | 71.1 | 0.075 |
| **08 Aug 2002** | 195 | 118.8 | 0.125 |

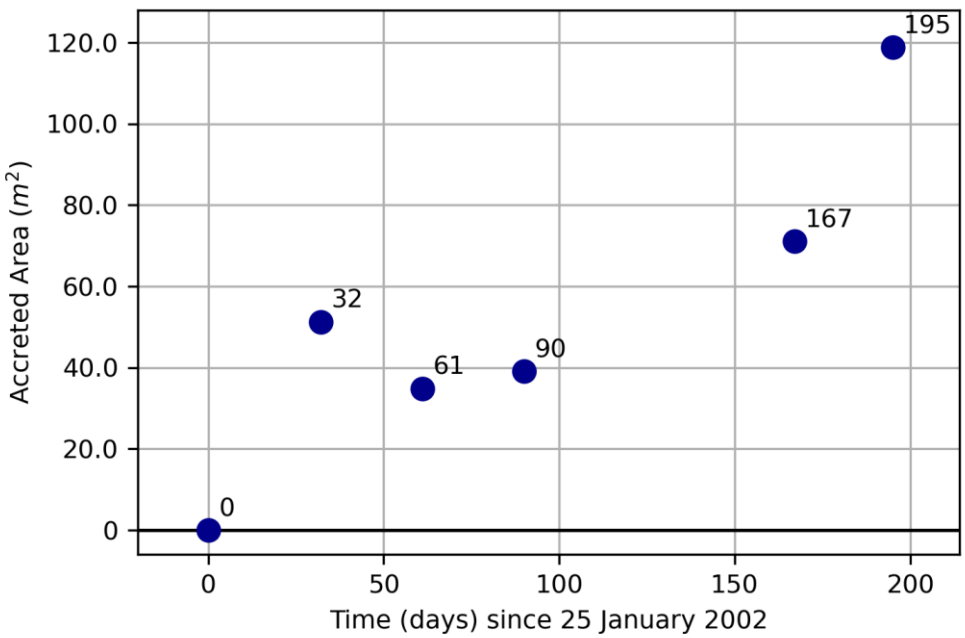


Figure 2.8: Temporal change of accreted area

# Chapter 3

# NUMERICAL MODEL

## 3.1 Extension of CSHORE to Mudflat

The physical processes of intertidal mudflat profile evolution under waves and currents were predicted using a numerical model. Fig. 3.1 presents the horizontal coordinate system adopted for this study.

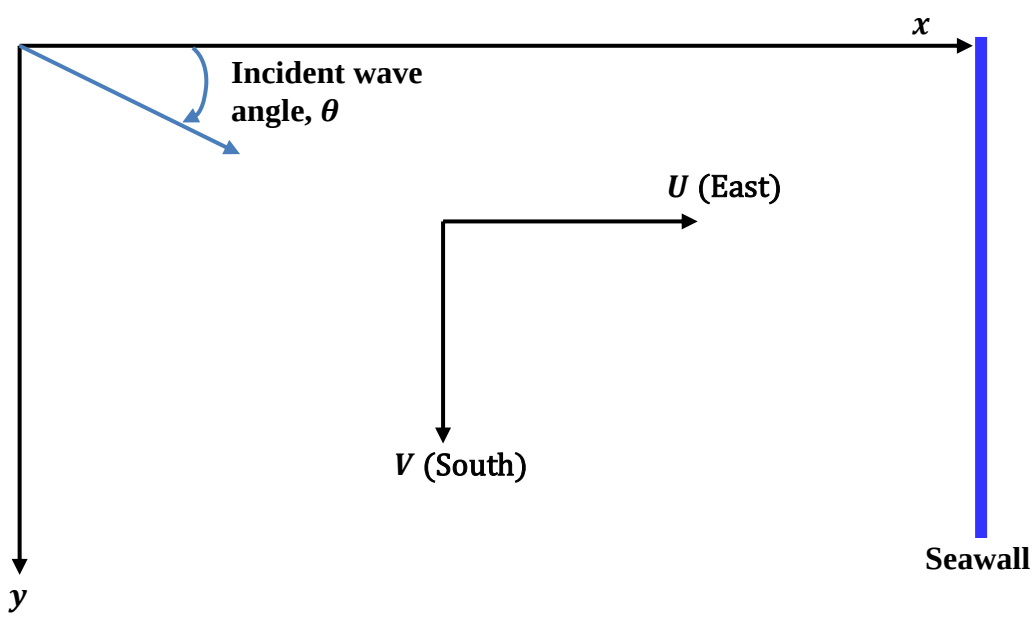


Figure 3.1: Adopted horizontal coordinate system $(x, y)$ and incident wave angle, $\theta$

The cross-shore and longshore coordinates $x, y$ are positive in the onshore and southern directions, respectively. For the cross-shore coordinate, the water level and incident waves are specified as input at the origin. The incident wave angle $\theta$ at the

origin is positive in the clockwise direction. For the longshore coordinate, the southerly orientation is based on the direction of observed mudflat current by Yamada et al. (2012). The depth-averaged velocities $U$ and $V$ are positive in the directions of $x$ and $y$, respectively.

The cross-shore numerical model CSHORE (Kobayashi 2016) based on the assumption of alongshore uniformity was extended for a mixture of sand and mud and is computationally efficient.

The depth-integrated continuity equation of water included the cross-shore tidal water flux by Do et al. (2012) and is expressed as

$$\bar{h}\bar{U} + \frac{g{\sigma_\eta}^2}{C}\cos\theta + q_r\cos\theta = q_0 + (x_{SWL} - x)\frac{\partial S}{\partial t} \tag{2}$$

where $\bar{h}$ = mean depth; $\bar{U}$ = mean cross-shore current; $g$ = gravitational acceleration; $\sigma_\eta$ = free surface standard deviation computed using a wave energy equation with significant wave height $H_{m0}$ = $4\sigma_\eta$; $C$ = phase velocity; $\theta$ = wave angle computed using Snell's law; $q_r$ = volume flux of a roller estimated using a roller energy equation; $q_0$ = rate of wave overtopping of the seawall (which is zero in this study); $x_{SWL}$ = cross-shore location of the still water shoreline; and $S$ = still water level which was assumed invariant in the cross-shore direction.

The second and third terms on the left-hand side of Eq. (2) are the onshore volume fluxes caused by wind waves and roller, respectively, while the last term on the right-hand side is the volume flux associated with water volume change between $x$ and $x_{SWL}$.

Without the second and third terms on the left-hand side which are both related to waves, Friedrichs and Aubrey (1996), and Pritchard and Hogg (2003) used Eq. (2)

to estimate the cross-shore tidal current which is maximum at the tidal front. In the absence of wave setup, the local mudflat slope is $\bar{h}/(x_{SWL} - x)$. For sandy beaches with large waves and small tidal ranges, Eq. (2) without the $S(t)$ term is used to estimate the return (undertow) current $\bar{U}$. For a macrotidal sand beach in Korea, Do et al. (2012) used Eq. (2) to include both cross-shore tidal and undertow current. In this study, Eq. (2) is used to predict $\bar{U}$.

For the case of zero wave overtopping of the seawall, the cross- and longshore momentum equations are written as

$$\frac{dS_{xx}}{dx} = -\rho g \bar{h} \frac{d\bar{\eta}}{dx} - \tau_{bx} + \tau_{sx} \tag{3}$$

$$\frac{dS_{xy}}{dy} = -\tau_{by} - \rho g \bar{h} S_y + \tau_{sy} \quad ; \quad S_y = \frac{\partial S}{\partial y} \tag{4}$$

where $S_{xx}$ = cross-shore radiation stress; $S_{xy}$ = shear component of the radiation stress; $\rho$ = water density; $\bar{\eta}$ = mean water level (wave setup); $\tau_{bx}$ = cross-shore bottom stress; $\tau_{sx}$ = cross-shore wind stress; $\tau_{by}$ = longshore bottom stress; and $\tau_{sy}$ = longshore wind stress.

The term including $S_y$ was included by Farhadzadeh et al. (2012) to predict longshore current generated by obliquely incident breaking waves in a wave basin with water recirculation. The order of magnitude for $S_y$ required to induce the observed southerly current on the mudflat was estimated by Yamada et al. (2012).

Kobayashi (2013) included the wind shear stress on the water surface that may be important outside the surf zone. The wind drag coefficient was estimated using the formula by Large and Pond (1981).

The mean water level $\bar{\eta}$ and mean longshore current $\bar{V}$ through $\tau_{by}$ are estimated using Eqs. (3) and (4) (Kobayashi 2016), respectively. At this site, the wave

setup is small for small incident waves and negligible at this tidal range. The mean longshore current $\bar{V}$ is generated by the incident waves through the $S_{xy}$ term in Eq. (4). The longshore bottom stress $\tau_{by}$ is modified by the longshore wind stress $\tau_{sy}$. The other effects such as alongshore tidal current and river discharge are represented by the alongshore water level gradient $S_y$. The effects of wind stresses and alongshore gradient $S_y$ are included after the calibration of CSHORE.

Mud erosion and deposition processes are normally expressed using mud suspension and settlement formulas with several empirical parameters (USACE 2003). Such formulas are not adopted for lack of extensive field data for the parameter calibration. The porosity of the mixture is denoted as $n_p$ and the solid volume per unit mixture volume is $(1 - n_p)$. The fraction of sand and mud in this solid volume is denoted as $f_s$ and $f_m$ where $f_m = 1 - f_s$. The values for $n_p$, $f_s$, and $f_m$ were assumed constant for this first CSHORE application to mudflat.

The cross-shore $(x)$ and longshore $(y)$ volumetric sediment transport rates $q_x$ and $q_y$ per unit width are expressed as

$$q_x = f_s(q_{bx} + q_{sx}) + f_m q_{mx} \tag{5}$$

$$q_y = f_s(q_{by} + q_{sy}) + f_m q_{my} \tag{6}$$

where $q_{bx}$ and $q_{by}$ = bed load transport rate in the $x$- and $y$-directions, respectively; $q_{sx}$ and $q_{sy}$ = suspended sand transport rate in the $x$- and $y$-directions, respectively; and $q_{mx}$ and $q_{my}$ = suspended mud transport rate in the $x$- and $y$-directions, respectively.

Mud is assumed to be transported as suspended load only while the sand transport rates $q_{bx}$, $q_{by}$, $q_{sx}$, and $q_{sy}$ are estimated using the formulas used in

CSHORE (Kobayashi 2016) for sand only case ($f_s$ = 1 and $f_m$ = 0). Eqs. (5) and (6) reduce to $q_x = q_{mx}$ and $q_y = q_{my}$ for mud only case ($f_s$ = 0 and $f_m$ = 1).

The mud transport rates $q_{mx}$ and $q_{my}$ are estimated using the following equations.

$$q_{mx} = a_x \bar{U} V_m \quad ; \quad q_{my} = \bar{V} V_m \tag{7}$$

where $V_m$ = suspended mud volume per unit horizontal bottom area; and $a_x$ = empirical suspended load parameter used for $q_{sx}$ which is 0.2 m on a gentle slope. It is noted that $a_x$ is dimensionless. The mud volume $V_m$ is expressed as

$$V_m = \frac{e_B D_r + e_f D_f}{\rho g w_e}\left(1 + {S_b}^2\right)^{0.5} \quad ; \quad w_e = \left(\frac{\rho_m}{\rho} - 1\right)\frac{w_m}{P_m} \tag{8}$$

where $S_b$ = cross-shore bottom slope; $D_r$ = roller energy dissipation rate; $D_f$ = wave energy dissipation rate due to bottom friction; $e_B$ and $e_f$ = suspension efficiencies for $D_r$ and $D_f$, respectively; $w_e$ = effective mud fall velocity; $\rho_m$ = mud density; $w_m$ = mud fall velocity; and $P_m$ = probability of mud suspension.

The dissipation rates $D_r$ and $D_f$ are computed when the wave energy and roller energy equations are solved numerically. The standard values of $e_B$ = 0.005 and $e_f$ = 0.01 are used in the computations.

Since the mud settling process is complicated (McAnally et al. 2021), three uncertain parameters ($\rho_m$, $w_m$, and $P_m$) are combined into a single parameter, effective mud fall velocity $w_e$. The effective mud fall velocity may be calibrated at each field site. Similarly, the mud volume fraction $f_m$ is assumed to be constant during mudflat profile evolution.

The temporal change in mudflat elevation $z_b$ is computed using the conservation of sediment volume equation

$$\left(1 - n_p\right)\frac{\partial z_b}{\partial t} + \frac{\partial q_x}{\partial x} + \frac{\partial q_y}{\partial y} = 0 \tag{9}$$

where $t$ = morphological time. CSHORE computes the temporal change of $z_b$ along the cross-shore ling using Eq. (9).

Yamada et al. (2012) concluded that the mudflat profile evolution along the cross-shore line $y$ = 0 in Fig. 2.2 must have been influenced by the alongshore sediment transport on the mudflat. The CSHORE extension by Kobayashi and Jung (2012) to allow for simultaneous computation of multiple cross-shore lines and include the effects of alongshore gradient $q_y$ in Eq. (9) was utilized.

The alongshore gradient $q_y$ is approximated by Zhu and Kobayashi (2021) for computation of bluff erosion along a single cross-shore line. The approximation for the single line in Fig. 2.2 yields

$$\frac{\partial q_y}{\partial y} = \frac{q_y}{y_e} \quad at\ y = 0 \tag{10}$$

where $y_e$ = equivalent alongshore length. The alongshore sediment transport rate $q_y$ is positive in the positive $y$-direction (south) in Fig. 3.1. For a positive $q_y$, the positive (negative) $y_e$ contributes to the temporal decrease (increase) of $z_b$ along the cross-shore ling $y$ = 0 in Fig. 2.2. The degree of computed erosion and accretion can be adjusted by calibrating the value of $y_e$. In this study, this calibration is necessary because alongshore loss or gain was not measured at the field site.

## 3.2 Computation Procedure

The results of the extended CSHORE were compared with the fitted profiles shown in Figs. 2.5 and 2.7. In order to identify the causes of the observed erosion and accretion on the mudflat, the comparisons were separated into the erosion (E) and accretion (A) intervals. The computation duration was 206 and 195 days for the E and A intervals, respectively.

For the computations during the E and A intervals, the initial profiles used were the fitted profiles on 03 July 2001 and 25 January 2002, respectively. The computational domain was between the seaward boundary at $x$ = 0 at a depth of $z = -6.3$ or $-6.4$ m and the seawall at $x$ = 3,000 m. The boundary conditions used in the model were no cross-shore gradient of $q_x$ at $x$ = 0 to solve Eq. (9), no wave overtopping in solving Eq. (2), and zero water and sediment fluxes in solving Eqs. (2) and (9) at $x$ = 3,000 m.

The time series of the water level $S(t)$ above the datum measured in the vicinity of the seaward boundary was simplified for the subsequent sensitivity analyses

$$\mathrm{S}(t) = S_a + A_t \sin\left(\frac{2\pi t}{T_t}\right) - A_y \cos\left(\frac{2\pi t}{T_y}\right) \tag{11}$$

where $S_a$ = average water level ($S_a$ = 0.14 m); $A_t$ = semidiurnal tide amplitude; $T_t$ = semidiurnal tide period ($T_t$ = 12.4 h); $A_y$ = amplitude of yearly water level oscillation; and $T_y$ = yearly oscillation period ($T_y$ = 1 y).

The water level associated with $T_y$ = 1 y in Eq. (11) decreased during the E interval and increased during the A interval. The water and sediment discharge from the river spread more on the mud flat during higher water levels (Yamada et al. 2011),

but the sediment exchange process between the mudflat and the river mouth was uncertain (Yamada et al. 2012).

The origin of time $t$ in Eq. (11) was 25 January 2002, the start of the A interval and when the yearly water level was the lowest. For the E interval, time $t$ was shifted so that $t$ = 0 is on 03 July 2001, the start of the E interval. The measured tide amplitude values were $A_t$ = 1.44 m and $A_y$ = 0.2 m.

The significant wave height and period in the vicinity of the seaward boundary were in the range of 0.1 – 0.3 m and 2 – 4 s, respectively. This study used the average values of 0.2 m and 3 s as the incident significant wave height $H_{m0}$ and spectral peak wave period $T_p$. The incident wave direction $\theta$ used in this study was $\theta$ = 30° which was taken from the measured wind direction. The range of values for subsequent tests were 0.1 – 0.3 m, 2 – 4 s, and 15° - 60° for the $H_{m0}$, $T_p$, and $\theta$, respectively.

The sediment properties used in this study are as follows. The sediment porosity was $n_p$ = 0.5. The sand parameters were $\rho_s$ = 2,800 kg/m$^3$, $d_{50}$ = 0.17 mm, $w_s$ = 2 cm/s, and $f_s$ = 0.3 while the mud parameters were $f_m$ = 0.7, and $w_e$ = 0.02 cm/s.

The volume fractions $f_s$ and $f_m$ were estimated using the measured masses of water, sand, and mud per unit volume of the mixed sediment. The effective mud fall velocity $w_e$ was calibrated to predict the magnitude of mudflat profile changes shown in Figs. 2.5 and 2.7. A decrease in $w_e$ increases the suspended mud volume $V_m$ in Eq. (8) and consequently, the mud transport rates $q_{mx}$ and $q_{my}$ in Eq. (7). The calibration resulted in an effective mud fall velocity $w_e$ = 0.02 cm/s. Given reasonable values of $(\rho_m/\rho)$ = 1.2 and $P_m$ = 1.0, this corresponded to a mud fall velocity $w_m$ = 0.1 cm/s. McAnally et al. (2021) measured mud fall velocities in the

range of 0.06 – 0.12 $\mathrm{cm/s}$ which showed that the calibrated value for $w_e$ may be physically reasonable.

The calibrated equivalent alongshore length $y_e$ in Eq. (10) was $y_e$ = 100 m for the E interval and $y_e$ = –100 m for the A interval. The positive $y_e$ leads to an alongshore sediment loss while a negative $y_e$ leads to an alongshore sediment gain. The distance may be related to the longshore distance between the cross-shore line at $y$ = 0 and the navigational channel through the mudflat at the mouth of the Shirakawa River in Fig. 2.2.

The sensitivity of the computed profile change to values of $y_e$ and $w_e$ are presented later.

Table 3.1 presents the basic input values for CSHORE computation during both E and A intervals. Sensitivity analysis for each parameter was done and explained in succeeding chapters to demonstrate its degree of importance to mudflat profile evolution.

Table 3.1: Basic input values for Erosion (E) and Accretion (A) Intervals

| **Input Parameter** | **Value** |
|---|---|
| Equivalent alongshore length, $y_e$, for erosion | 100 m |
| Equivalent alongshore length $y_e$, for accretion | -100 m |
| Effective mud fall velocity, $w_e$ | 0.2 mm/s |
| Mud volume fraction, $f_m$ | 0.7 |
| Amplitude, $A_y$, of yearly water level variation | 0.2 m |
| Semidiurnal tide amplitude, $A_t$ | 1.44 m |
| Incident significant wave height, $H_{m0}$ | 0.2 m |
| Spectral peak period, $T_p$ | 3 s |
| Incident wave angle, $\theta$ | 30° |

CSHORE performs a landward-marching computation based on Eqs. (2) – (4) with the wave and roller energy equations. The adopted nodal spacing was 5 m over the cross-shore distance of 3,000 m. The computation was limited to the wet zone below the still water level since the swash zone of the small waves was not resolved by the nodal spacing. The landward-marching computation was terminated at a mean water depth $\bar{h}$ of about 1 cm.

After the hydrodynamic variables were computed, the sediment transport rates were computed using Eqs. (5) – (8). Then the temporal change in mudflat elevation $z_b$ was computed using Eqs. (9) and (10) with an appropriate time step size that satisfied numerical stability.

The computational procedure was repeated until the end of the E and A intervals. The computational time was less than 1 minute for each of the cases presented below.

# Chapter 4

# COMPARISON WITH DATA

## 4.1 Erosion interval

Fig. 4.1 presents the hourly water level time series during the E interval, 03 July 2001 to 25 January 2002. The time series was created using Eq. (11) and the basic input values in Table 3.1. The effect of the yearly water level oscillation is evident in the figure with water levels high earlier in the interval than they are towards the end.

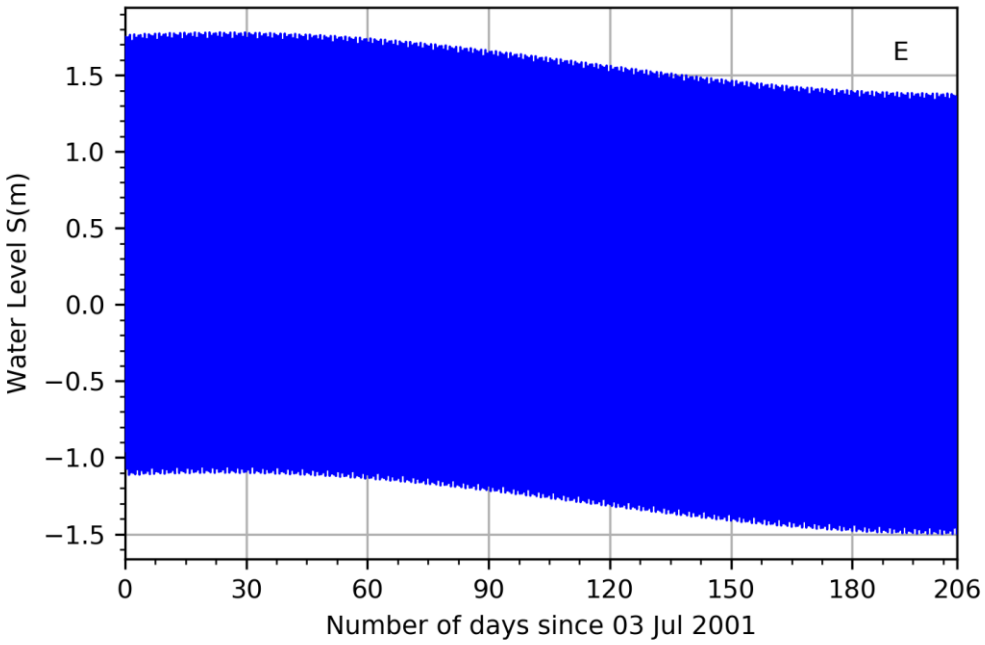


Figure 4.1: Time series of water level assumed for Erosion (E) interval of 206 days

### 4.1.1 Base case of equivalent alongshore distance $y_e$ = 100 m

The equivalent alongshore length for the basic case is $y_e$ = 100 m. The positive value of $y_e$ results in alongshore sediment loss for $q_y > 0$ in Eq. (10).

The hourly hydrodynamic and sediment transport variables are presented in Figs. 4.2 to 4.4 to show the role of semidiurnal tides and waves within a semidiurnal tide period.

Fig. 4.2 shows cross-shore variation of the mean water depth $\bar{h}$, the significant wave height $H_{m0}$, the mean cross-shore current $\bar{U}$, and the standard deviation $\sigma_U$, which is associated with the oscillatory cross-shore wave velocity, during the time $t$ = 1 – 13 h from $t$ = 0 of the E interval.

The temporal change in $\bar{h}$ was dominated by the semidiurnal tide while the cross-shore variation of $\bar{h}$ was influenced by both the mudflat profile and the seawall.

The cross-shore variation in $H_{m0}$ was caused by refraction, shoaling, and wave energy dissipation due to bottom friction and wave breaking. The sudden decrease in $H_{m0}$ became obvious in the surf zone on the mudflat. Wave breaking does not occur when the toe depth at the seawall is significantly larger than the incident wave height. During such instances, it must be noted that CSHORE does not include wave reflection from the seawall. This limitation may not pose a risk to the accuracy of the results since breaking waves and currents are what drive sediment transport in small water depths on a mudflat.

The mean cross-shore current $\bar{U}$ was dominated by flood ($\bar{U}$ > 0) and ebb ($\bar{U}$ < 0) currents. These were small during high tide and when non-breaking waves were at the seawall. Tidal current measurements were made by Yamada et al. (2011)

during 2006 - 2009 in the vicinity of the cross-shore profile in Fig. 2.2. Although the measurements were limited to a water depth exceeding 0.3 m, the measured velocities were in the order of 0.1 $\mathrm{m/s}$.

The standard deviation or oscillatory cross-shore wave velocity $\sigma_U$ increased landward and was maximum in the breaker zone. Its magnitude decreased landward in the surf zone.

Fig. 4.3 shows cross-shore variation of the sin $\theta$ with $\theta$ = wave angle, the mean longshore current $\bar{V}$, and the standard deviation $\sigma_V$, associated with the oscillatory longshore wave velocity, during the same time interval.

The wave angle $\theta$ decreased landward as the wave refracts from $\theta$ = 30° at the seaward boundary. The degree of refraction was noticeably lower during high tide.

The mean longshore current $\bar{V}$ was caused by breaking waves since $S_y$ and $\tau_{sy}$ are zero in Eq. (4) for this base case. The effects of $S_y$ and $\tau_{sy}$ were examined in later analyses. The order of magnitude for the computed $\bar{V}$ was much less than the order of magnitude for the computed $\bar{U}$ which included the cross-shore tidal current and the wave-induced current.

The standard deviation or oscillatory longshore wave velocity $\sigma_V$ was of a lower order of magnitude from the oscillatory cross-shore wave velocity because the wave angle decreases landward.

Fig. 4.4 shows the computed sediment transport rates $q_x$ and $q_y$ from Eqs. (5) and (6). Both volumetric rates were in the order of $10^{-5}$ $\mathrm{m^2/s}$. The bed load rates $q_{bx}$ and $q_{by}$ were in the order of $10^{-8}$ $\mathrm{m^2/s}$ which is negligible in Eqs. (5) and (6). The suspended sand transport rates with $w_s$ = 2 $\mathrm{cm/s}$ were much smaller than the suspended mud transport rates with $w_e$ = 0.02 $\mathrm{cm/s}$. The computed mud volume $V_m$

per unit bottom area was large in the surf zone. The cross-shore sediment transport rate $q_x$ was positive (onshore) during flood tide and negative (offshore) during ebb tide while the longshore sediment transport rate $q_y$ was in the same direction as the mean longshore current $\bar{V}$. The computed sediment transport rates were of the same order of magnitude as the mud transport rates measured by Yamada et al. (2011) who measured the velocities and mud concentrations on the mudflat. Yamada et al. (2011) could not distinguish the wave-induced currents in the order of $0.01\ \mathrm{m/s}$ and tidal currents in the order of $0.1\ \mathrm{m/s}$.

The mudflat elevation change was computed with Eq. (9). The change in computed sediment transport rates was less than $10^{-3}$ from $t$ = 1 – 13 h.

The sediment transport rates were integrated with respect to time $t$ from $t$ = 0 to obtain the cumulative sediment volumes $v_x$ and $v_y$ per unit width as a function of $t$. Fig. 4.5 shows the cumulative sediment volumes during time $t$ when the mudflat profiles were measured, similar to Fig. 2.5. The semidiurnal variations in Fig. 4.4 are not apparent in Fig. 4.5 after the exposure to multiple tide cycles. The cross-shore volume $v_x$ was influenced by offshore suspended sediment transport from the undertow current induced by the breaking waves in the surf zone while the longshore volume $v_y$ was caused by the longshore current induced by wave breaking.

The sinusoidal semidiurnal tide is not effective in producing net sediment transport (Pritchard and Hogg 2003). The computed cross-shore volume illustrated the point of Pritchard and Hogg well since the volume of sediment directed offshore in the surf zone accumulated just seaward of the breaker zone but never got transported past the seaward boundary.

The wave-induced currents on a mudflat may be small for small waves, such was the case for the longshore sediment transport rates. However, the small net transport accumulated as computed by the longshore sediment volume $v_y$ with a maximum volume of almost 14 $\mathrm{m}^2$ along the profile.

Fig. 4.6 presents evolution of the fitted and computed profiles together with the initial profile on 03 July 2001. The computed profiles showed a consistent erosion of the mudflat throughout the E interval along the entire measured profile. This was contrasted with the periods when the fitted profiles had some accretion close to the seawall.

Fig. 4.7 shows the deviation of the computed profiles from the initial profile. The computed profiles were able to consistently reproduce the middle part of the profile fairly well. This was evidenced by the elevation difference in that part of the profile at less than 0.04 m. Difficulty in capturing the evolution at the seaward end ($x$ = 1,950 m) was evident during the earlier parts of the E interval. Erosion was overpredicted in the vicinity of the landward end ($x$ = 2,900 m).

Fig. 4.8 presents the amount of erosion for both the fitted and computed results along the entire measured profile during the E interval. The computed profiles showed a monotonic increase in erosion and is consistent with the profiles in Fig. 4.6. This was because of the assumption of constant wave height, period, and direction. There was significant variability in the fitted profile's evolution which at specific times resulted in some accretion ($t$ = 64 and 122 days) and resulted in a big discrepancy in erosion areas between the fitted and computed profiles especially early in the E interval. The error in the latter days of the E interval was less and can be attributed to the inability to capture the mudflat evolution at the landward end ($x$ = 2,900 m).

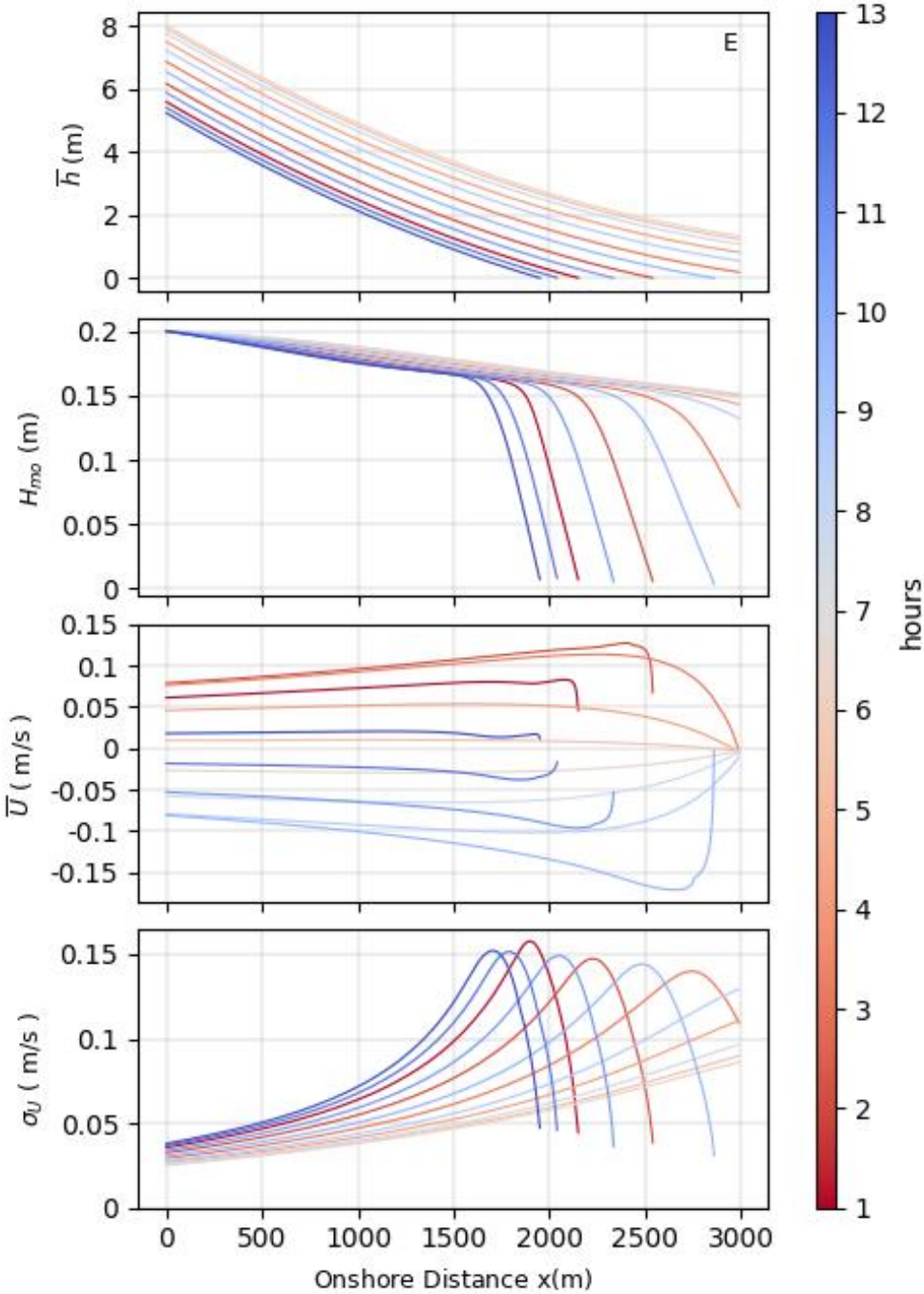


Figure 4.2: Hourly cross-shore variation of mean water depth ($\bar{h}$), significant wave height ($H_{m0}$), mean ($\bar{U}$) and standard deviation ($\sigma_U$) of cross-shore velocity ($U$) at beginning of E interval

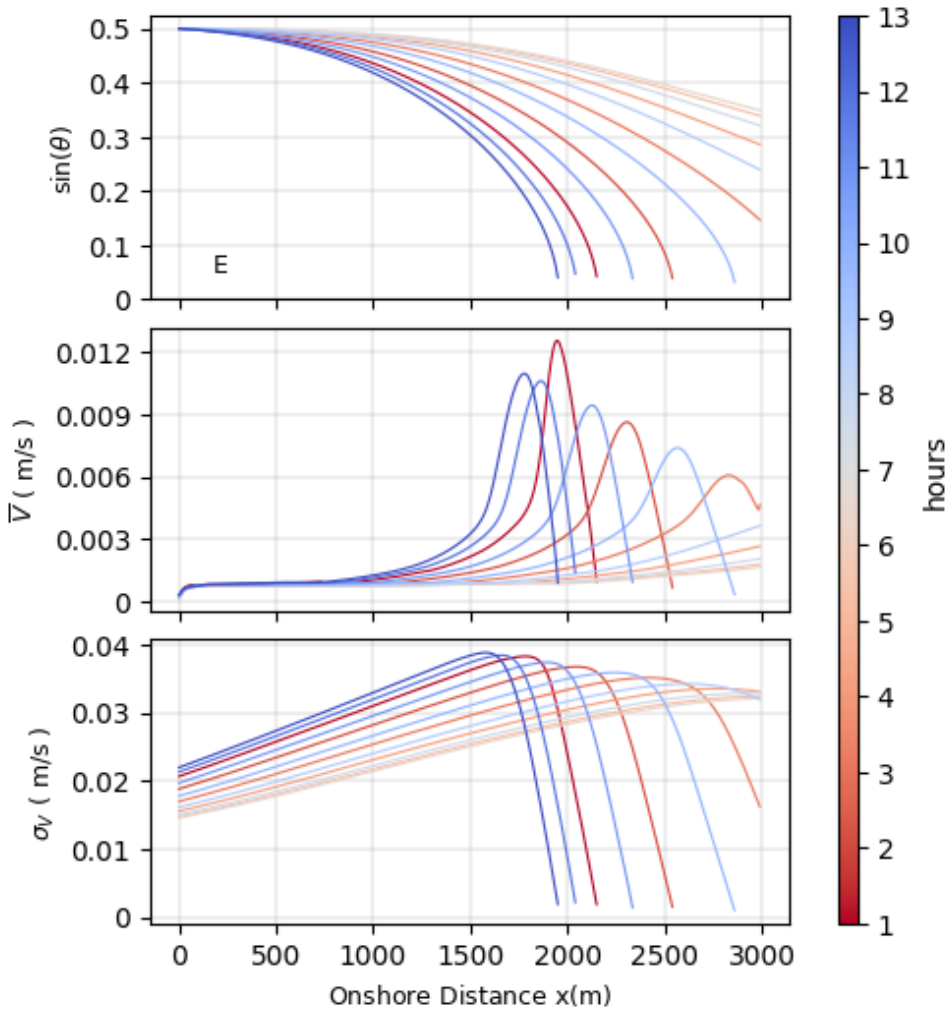


Figure 4.3: Hourly cross-shore variation of sin $\theta$ ($\theta$ = wave angle), mean ($\bar{V}$) and standard deviation ($\sigma_V$) of longshore velocity ($V$) at beginning of E interval

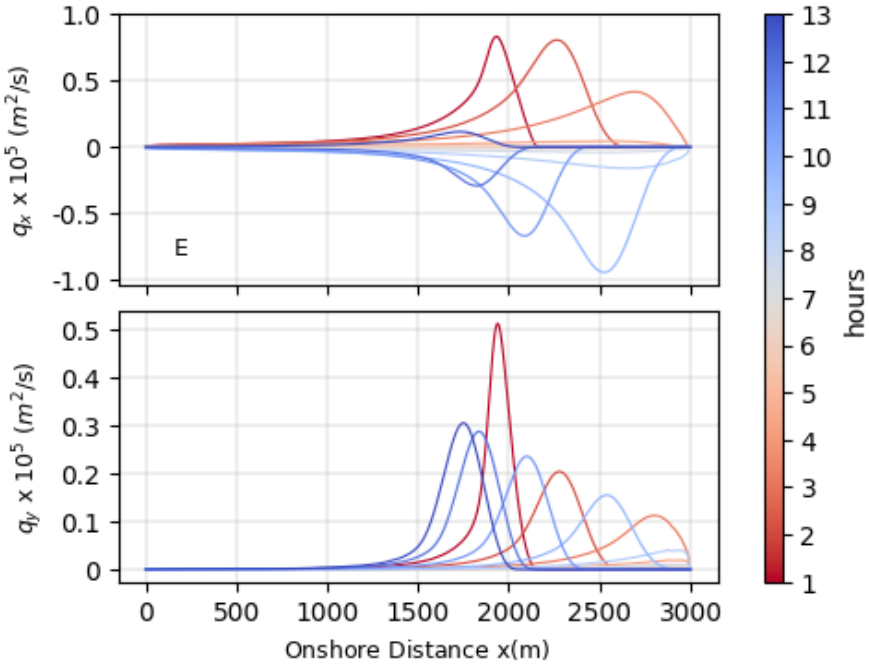


Figure 4.4: Hourly cross-shore variation of cross-shore sediment transport rate ($q_x$) and longshore sediment transport rate ($q_y$) at the beginning of E interval

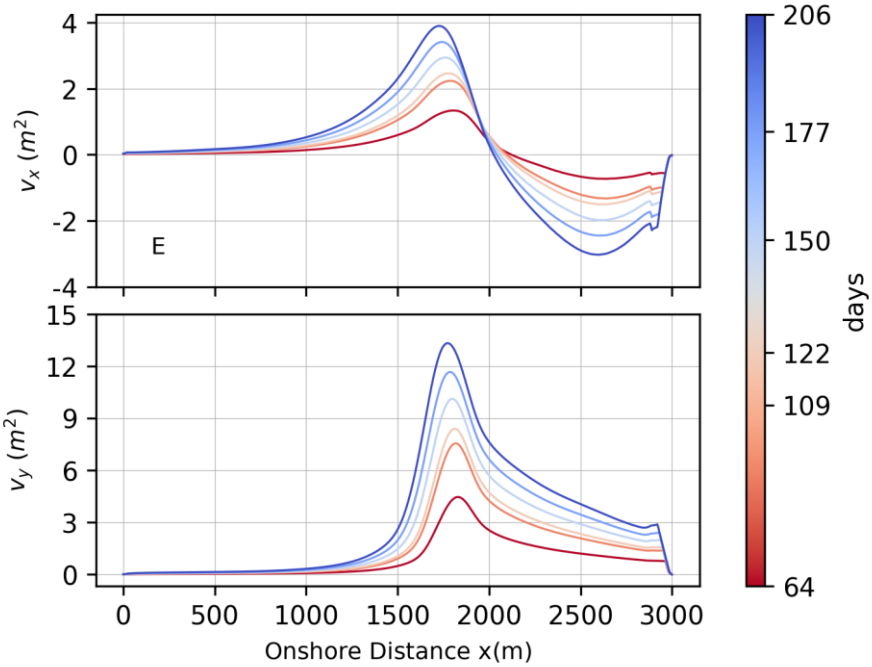


Figure 4.5: Cross-shore variation of cumulative sediment transport volumes $v_x$ and $v_y$ calculated by integrating $q_x$ and $q_y$ from time $t$ = 0 to $t$ = 64, 109, 122, 150, 177, and 206 days during E interval

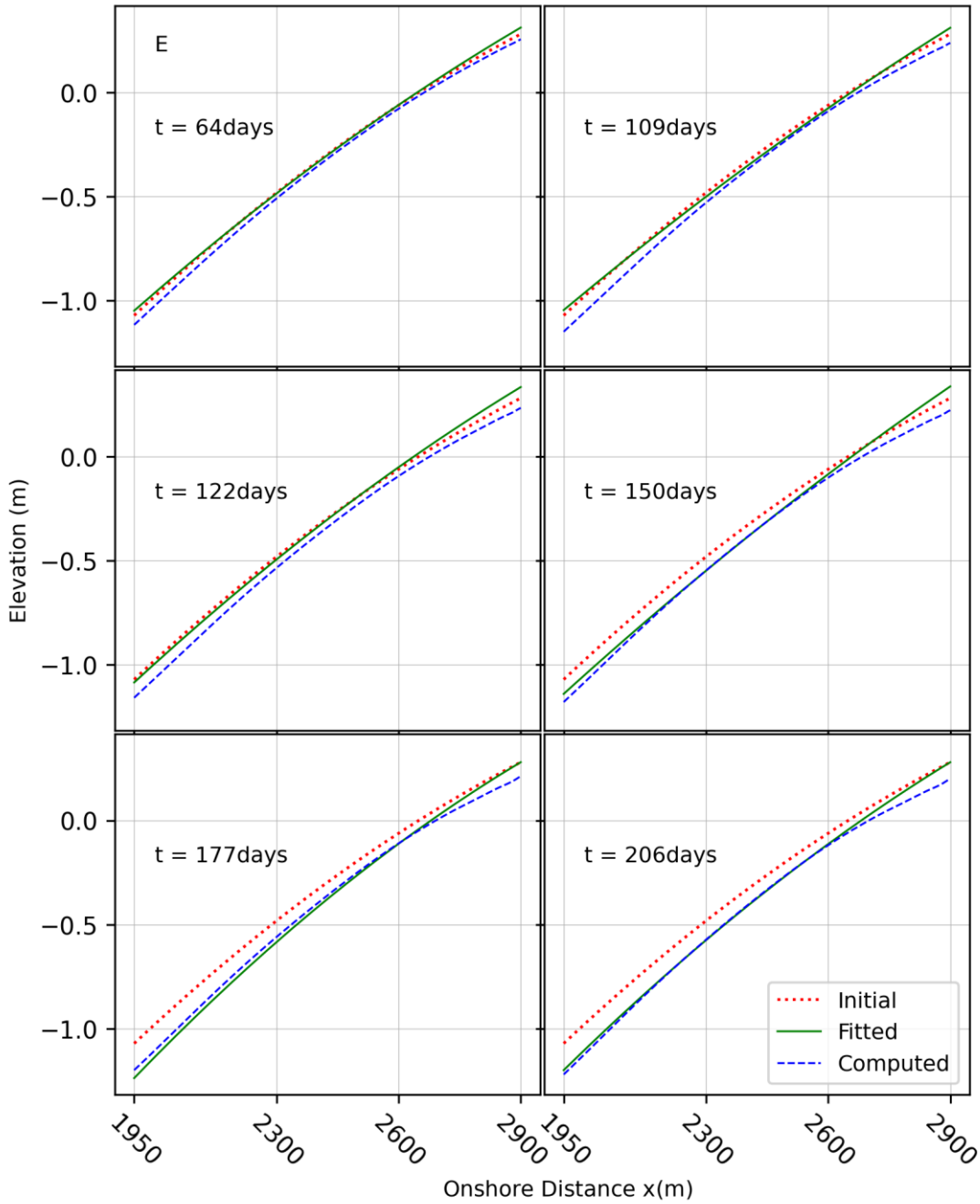


Figure 4.6: Comparison of fitted and computed mudflat profiles relative to initial profile at $t$ = 64, 109, 122, 150, 177 and 206 days during E interval

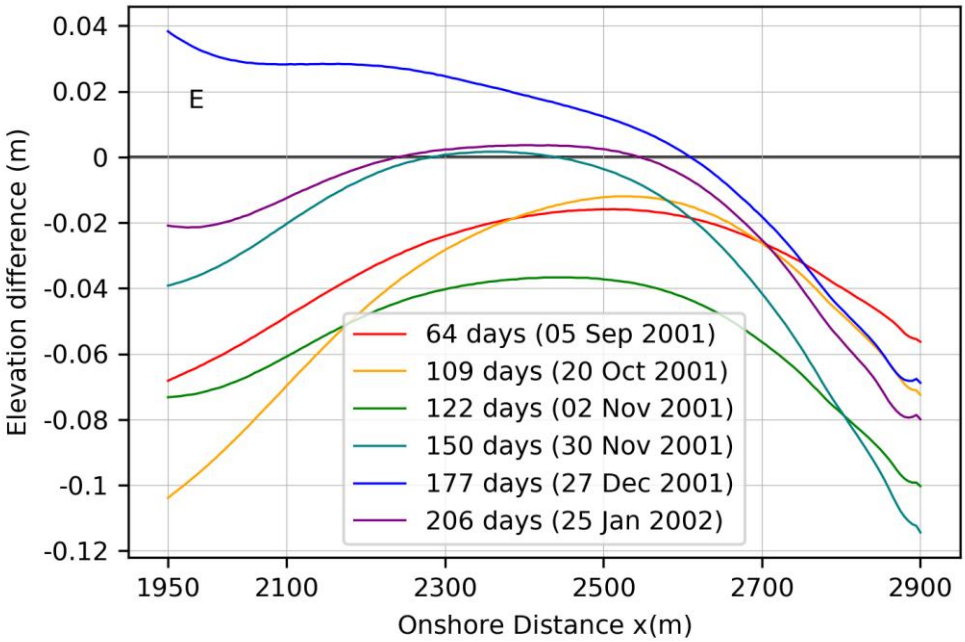


Figure 4.7: Deviation of computed mudflat profile from fitted profile at time $t$ = 64, 109, 122, 150, 177 and 206 days during E interval

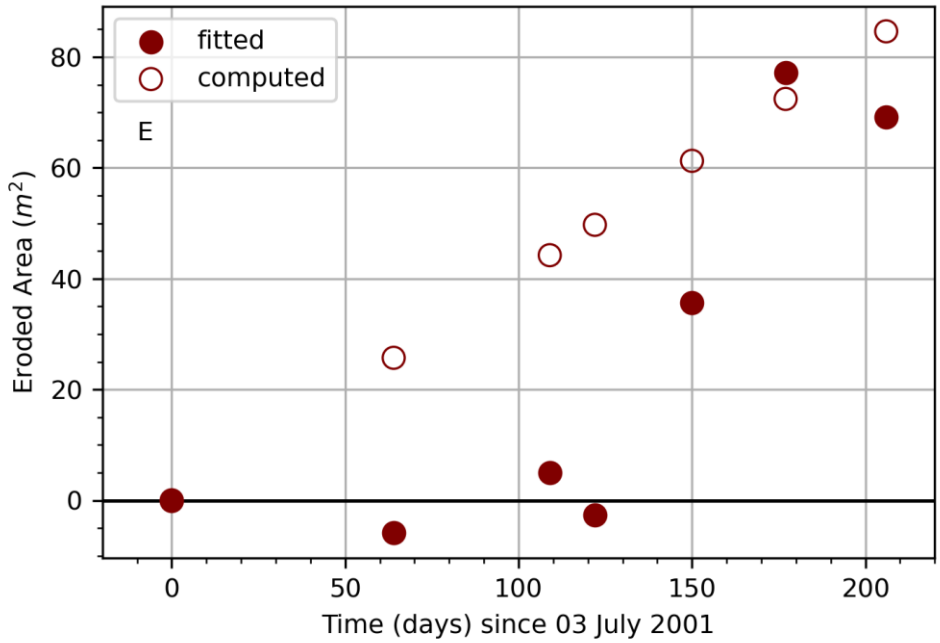


Figure 4.8: Comparison of fitted and computed eroded areas during E interval

### 4.1.2 Alongshore uniform case of IQYDY = 0

An alongshore uniform case was done to compare with the basic case and quantify deviation when there is no sediment loss in the alongshore direction. This case neglected the third term in Eq. (9) therefore mudflat elevation change was only affected by cross-shore sediment transport.

Fig. 4.9 presents the cumulative sediment volumes $v_x$ and $v_y$ per unit width as a function of $t$ for the alongshore uniform case during E interval. In comparison with the basic case, the cross-shore volume was slightly lower offshore of the breaker zone while the longshore volume was marginally higher in the same location.

The lack of longshore sediment loss resulted in net accretion along the profile. Both Figs. 4.10 and 4.11 display significant accretion along most of the profile and a slight erosion at the landward end. This suggested that the sediment was merely transported from the surf zone to offshore of the breaker zone.

The comparison of eroded areas in Fig. 4.12 illustrates net accretion for this alongshore uniform case. The eroded areas varied significantly except at two points ($t$ = 64 and 122 days). However, at $t$ = 122 days, the profile evolution did not adequately capture the evolution of the fitted profile. This case demonstrated that the mudflat profile evolution at this site during E interval is a 2D process.

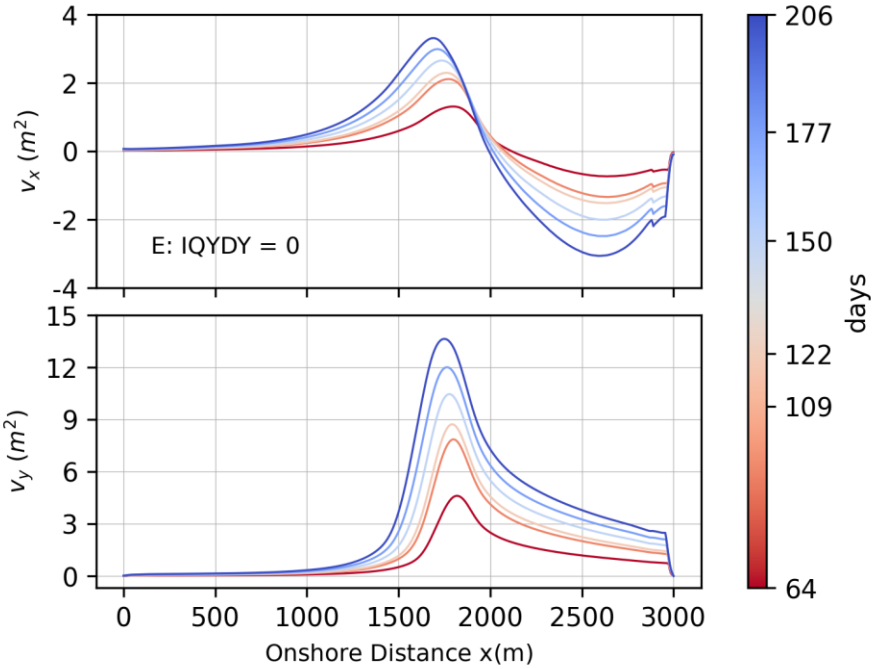


Figure 4.9: Cross-shore variation of cumulative sediment transport volumes $v_x$ and $v_y$ during E interval for alongshore uniform case of IQYDY = 0

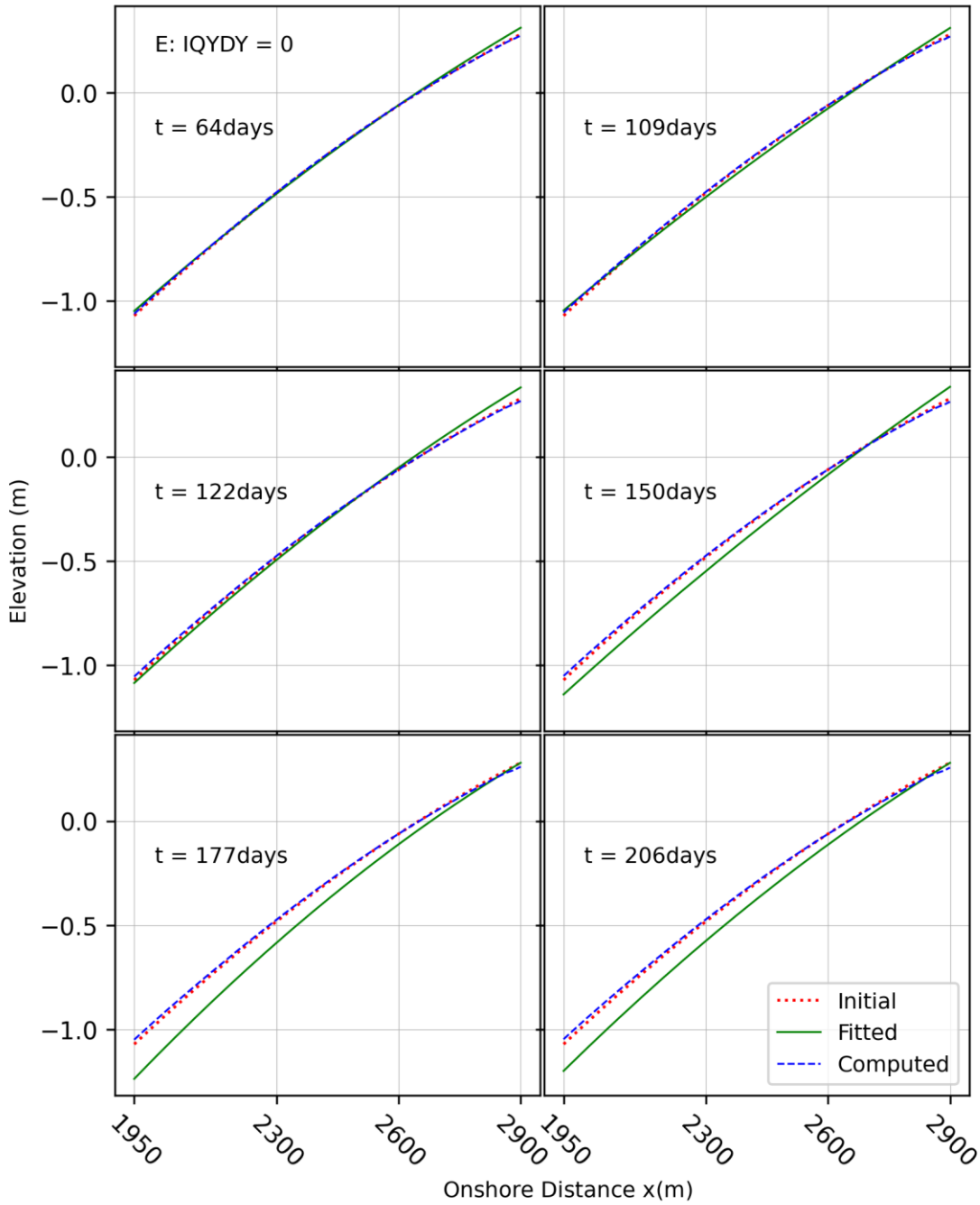


Figure 4.10: Comparison of fitted and computed mudflat profiles relative to initial profile during E interval for alongshore uniform case of IQYDY = 0

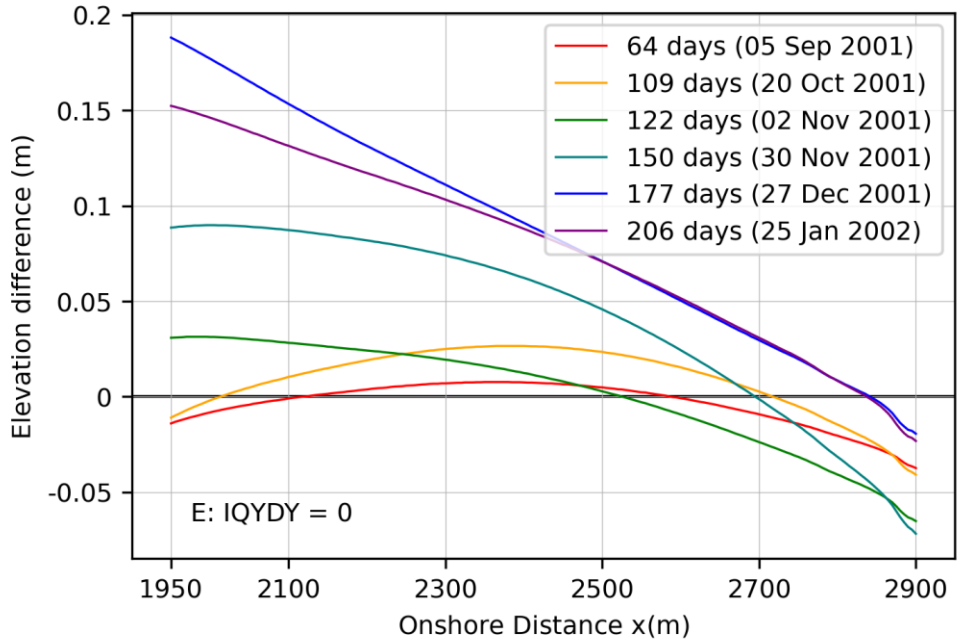


Figure 4.11: Deviation of computed mudflat profile from fitted profile at given time during E interval for alongshore uniform case of IQYDY = 0

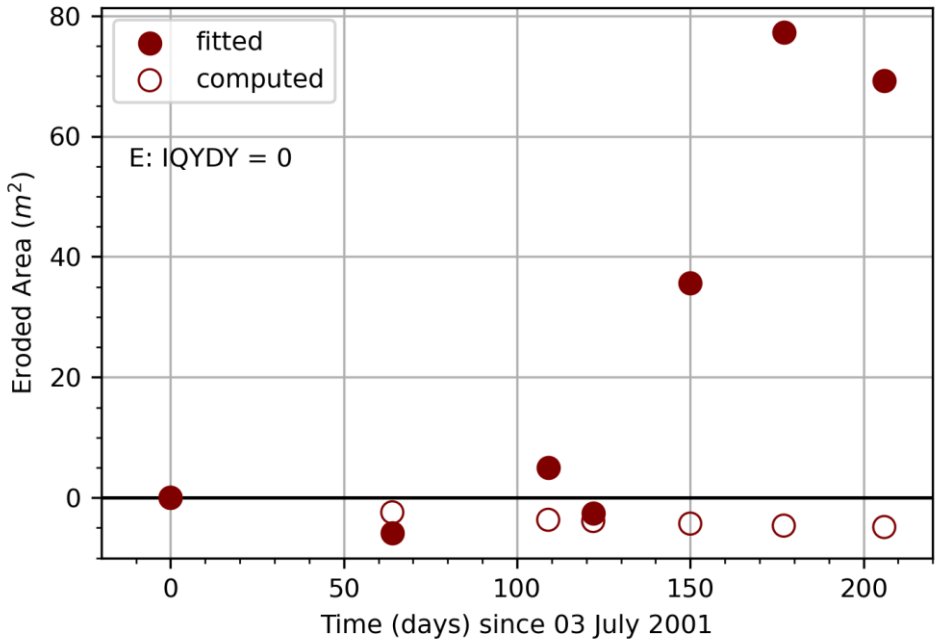


Figure 4.12: Comparison of fitted and computed eroded areas (negative implies net accretion) during E interval for alongshore uniform case of IQYDY = 0

### 4.1.3 Profile change sensitivity to increased $y_e$ = 200 m

A different equivalent alongshore length case was done to compare with the basic case and check for its sensitivity. This case affected the longshore sediment transport in Eq. (10).

Fig. 4.13 presents the cumulative sediment volumes $v_x$ and $v_y$ per unit width as a function of $t$ for an equivalent alongshore length $y_e$ = 200 m case during E interval. In comparison with the basic case, the longshore volume was slightly higher offshore of the breaker zone while the cross-shore case was almost the same.

Fig. 4.14 displays a reduced rate of erosion of the mudflat profile especially towards the latter end of the E interval compared with the basic case. This reduced rate exhibited better agreement with the fitted profiles until $t$ = 150 days. After this time, the seaward end of the profile was unable to keep pace with that of the fitted profile.

Fig. 4.15 shows the deviation of the computed profiles from the fitted profile. The computed profiles were able to consistently reproduce most of the profiles until $t$ = 150 days fairly well. This was evidenced by the elevation difference not exceeding 0.05 m. The final two data points in the E interval showed significant elevation difference at the seaward end.

Fig. 4.16 presents the amount of erosion for both the fitted and computed results of the equivalent alongshore length $y_e$ = 200 m along the entire measured profile during the E interval. The computed profiles showed a monotonic increase in erosion although noticeably less than that of the basic case. However, the error between the eroded area of the fitted and computed profiles are less than that of the basic case until $t$ = 150 days. This case demonstrated that CSHORE cannot satisfactorily predict temporal change in eroded area with a constant value of $y_e$.

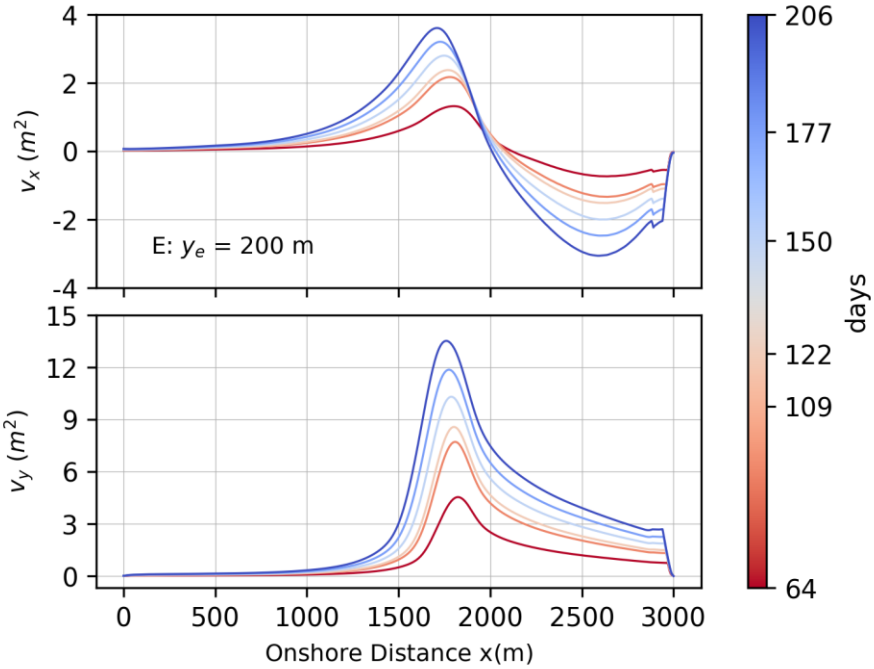


Figure 4.13: Cross-shore variation of cumulative sediment transport volumes $v_x$ and $v_y$ during E interval for increased $y_e$ = 200 m

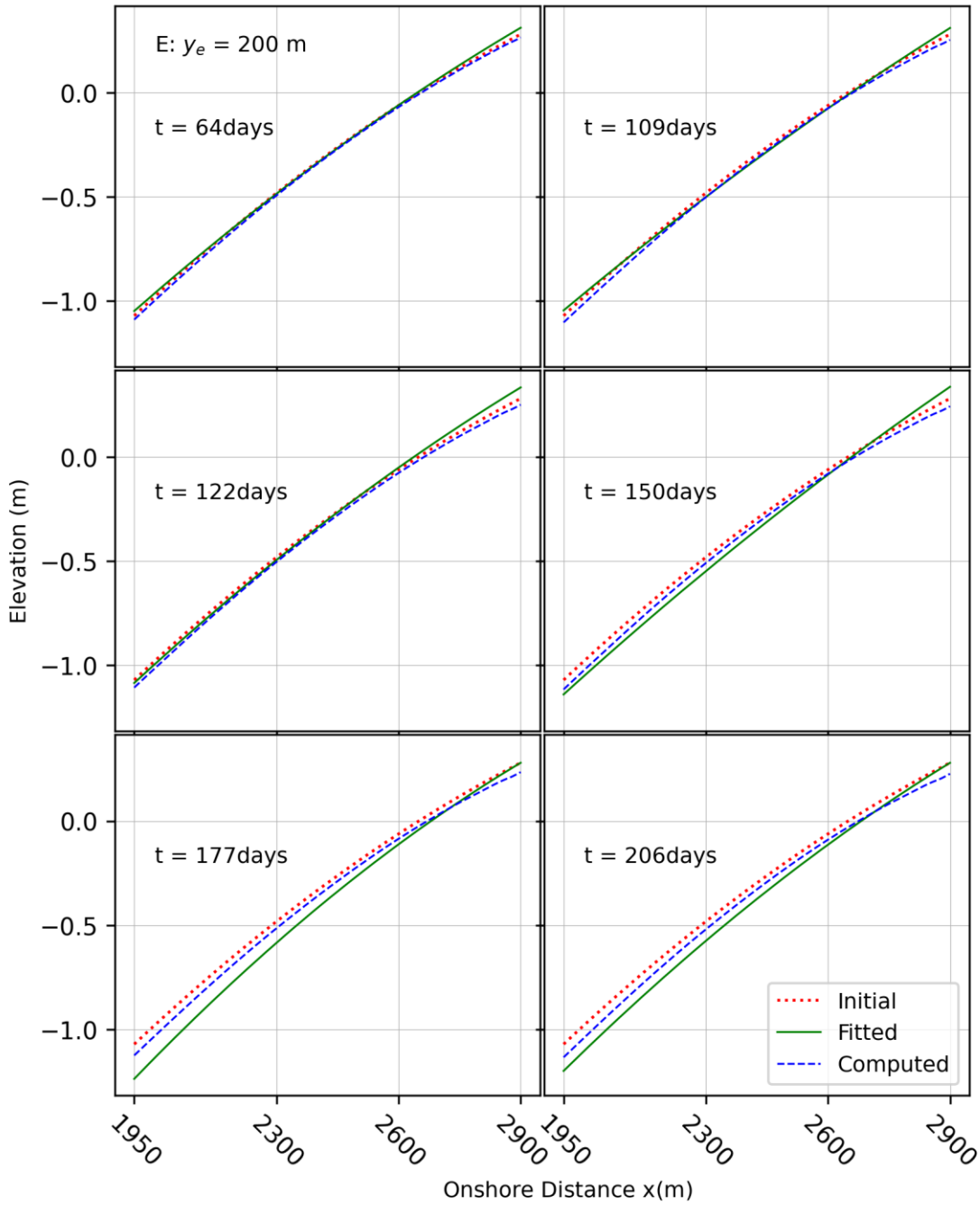


Figure 4.14: Comparison of fitted and computed mudflat profiles relative to initial profile during E interval for increased $y_e$ = 200 m

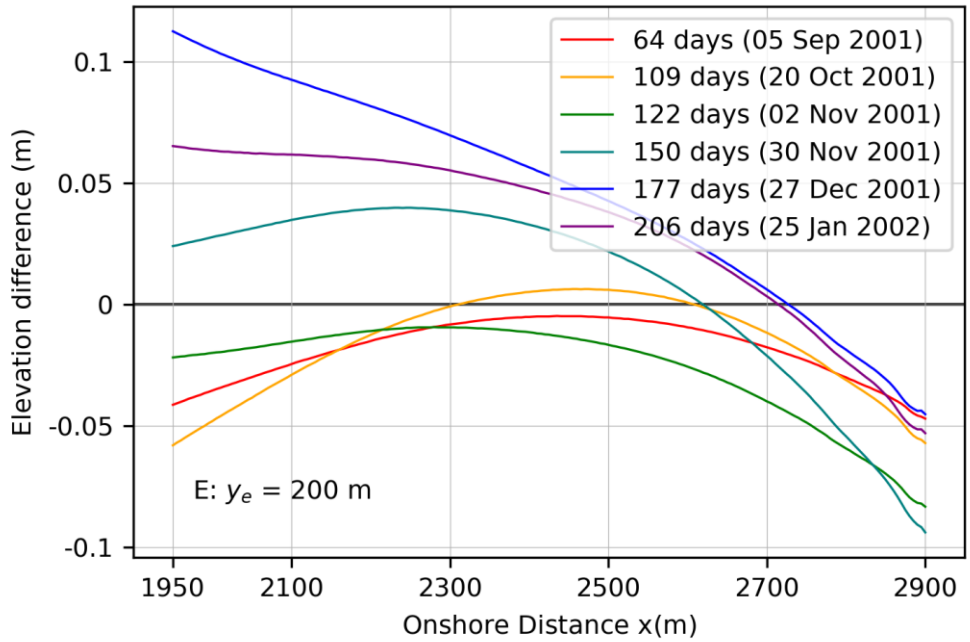


Figure 4.15: Deviation of computed mudflat profile from fitted profile at given time during E interval for increased $y_e$ = 200 m

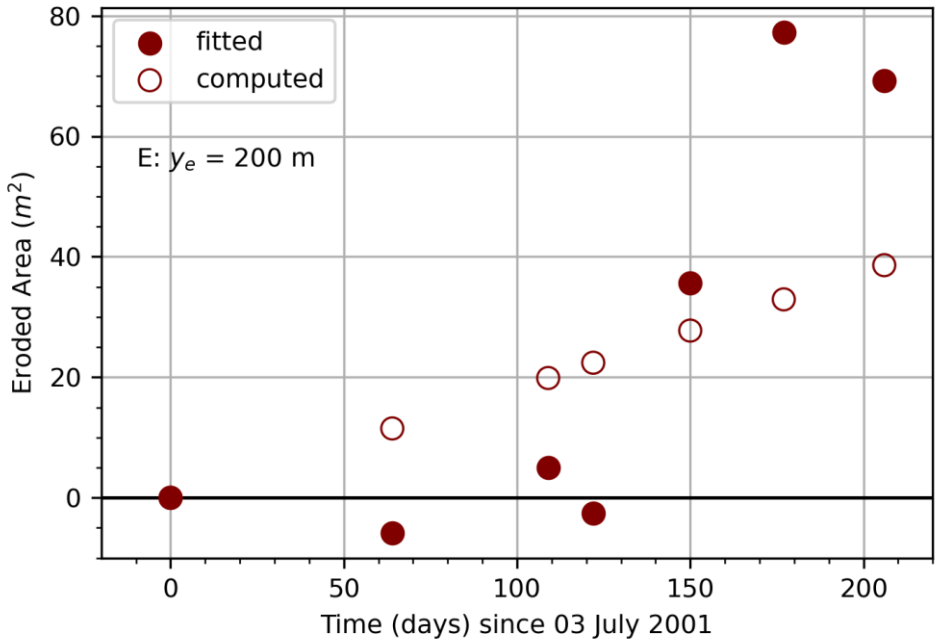


Figure 4.16: Comparison of fitted and computed eroded areas (negative implies net accretion) during E interval for increased $y_e$ = 200 m

## 4.2 Accretion interval

Fig. 4.17 presents the hourly water level time series during the A interval, 25 January 2002 to 08 August 2002. The time series was also created using Eq. (11) and the basic input values in Table 3.1. The effect of the yearly water level oscillation is evident in the figure with water levels low earlier in the interval than they are towards the end.

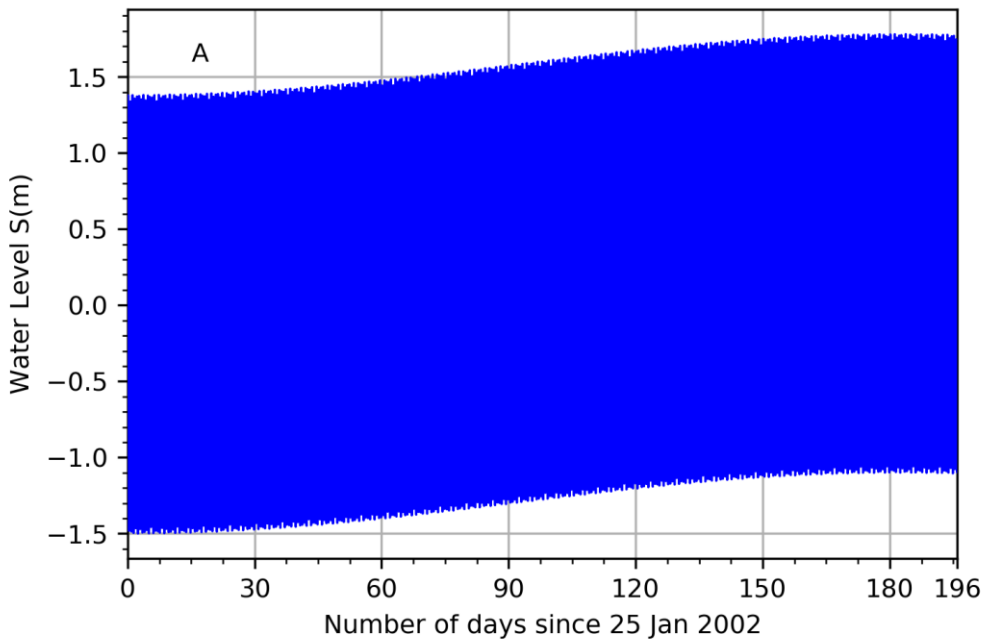


Figure 4.17: Time series of water level assumed for Accretion (A) interval of 195 days

### 4.2.1 Base case of equivalent alongshore distance (-$y_e$) = 100 m

The equivalent alongshore length for the basic case is (-$y_e$) = 100 m. The negative value of $y_e$ results in alongshore sediment gain for $q_y > 0$ in Eq. (10).

The hourly hydrodynamic and sediment transport variables are presented in Figs. 4.18 to 4.20 to show the role of semidiurnal tides and waves within a semidiurnal tide period.

Fig. 4.18 shows cross-shore variation of the mean water depth $\bar{h}$, the significant wave height $H_{m0}$, the mean cross-shore current $\bar{U}$, and the standard deviation $\sigma_U$, which is associated with the oscillatory cross-shore wave velocity, during the time $t$ = 1 – 13 h from $t$ = 0 of the A interval.

The temporal change in $\bar{h}$ was dominated by the semidiurnal tide while the cross-shore variation of $\bar{h}$ was influenced by both the mudflat profile and the seawall.

The cross-shore variation in $H_{m0}$ was cause by refraction, shoaling, and wave energy dissipation due to bottom friction and wave breaking. The sudden decrease in $H_{m0}$ became obvious in the surf zone on the mudflat. Wave breaking does not occur when the toe depth at the seawall is larger than the incident wave height.

The mean cross-shore current $\bar{U}$ was dominated by flood ($\bar{U}$ > 0) and ebb ($\bar{U}$ < 0) currents. These were small during high tide and when non-breaking waves were at the seawall.

The standard deviation or oscillatory cross-shore wave velocity $\sigma_U$ increased landward and is maximum in the breaker zone. Its magnitude decreased landward in the surf zone.

Fig. 4.19 shows cross-shore variation of the sin $\theta$ with $\theta$ = wave angle, the mean longshore current $\bar{V}$, and the standard deviation $\sigma_V$, associated with the oscillatory longshore wave velocity, during the same time interval.

The wave angle $\theta$ decreased landward as the wave refracts from $\theta$ = 30° at the seaward boundary. The degree of refraction was noticeably lower during high tide.

The mean longshore current $\bar{V}$ was caused by breaking waves since $S_y$ and $\tau_{sy}$ are zero in Eq. (4) for this base case. The order of magnitude for the computed $\bar{V}$ was much less than the order of magnitude for the computed $\bar{U}$ which included the cross-shore tidal current and the wave-induced current.

The standard deviation or oscillatory longshore wave velocity $\sigma_V$ was of a lower order of magnitude from the oscillatory cross-shore wave velocity because the wave angle decreases landward.

Fig. 4.20 shows the computed sediment transport rates $q_x$ and $q_y$ from Eqs. (5) and (6). Both volumetric rates were in the order of $10^{-5}$ $\mathrm{m}^2/\mathrm{s}$. The bed load rates $q_{bx}$ and $q_{by}$ were negligible in Eqs. (5) and (6). The cross-shore sediment transport rate $q_x$ was positive (onshore) during flood tide and negative (offshore) during ebb tide while the longshore sediment transport rate $q_y$ was in the same direction as the mean longshore current $\bar{V}$.

The mudflat elevation change was computed with Eq. (9). The change in computed sediment transport rates was less than $10^{-3}$ from $t$ = 1 – 13 h.

Fig. 4.21 shows the cumulative sediment volumes during time $t$ when the mudflat profiles were measured. The semidiurnal variations in Fig. 4.20 are not apparent in Fig. 4.21 after the exposure to multiple tide cycles. The cross-shore volume $v_x$ was influenced by offshore suspended sediment transport from the undertow current induced by the breaking waves in the surf zone while the longshore volume $v_y$ was caused by the longshore current induced by wave breaking.

The wave-induced currents on a mudflat may be small for small waves, such was the case for the longshore sediment transport rates. However, the small net transport accumulated as computed by the longshore sediment volume $v_y$ with a maximum volume of over 15 $\mathrm{m}^2$ along the profile.

Fig. 4.22 presents evolution of the fitted and computed profiles together with the initial profile on 25 January 2002. The computed profiles showed a consistent accretion of the mudflat throughout the A interval along the entire measured profile. Throughout interval A, the agreement between the fitted and computed profiles was very good until time $t$ = 195 days wherein there is some underprediction in the middle.

Fig. 4.23 shows the deviation of the computed profiles from the initial profile. The computed profiles were able to consistently reproduce the fitted profile fairly well. This was evidenced by the elevation difference along most of the profiles at less than 0.04 m.

Fig. 4.24 presents the amount of accretion for both the fitted and computed results along the entire measured profile during the A interval. The computed profiles showed a monotonic increase in accretion and was consistent with the profiles in Fig. 4.22. This was because of the assumption of constant wave height, period, and direction. There was variability in the fitted profile's evolution which at specific times ($t$ = 61 days) resulted in a lower accretion area. The computed profiles were able to capture the accretion with reasonable accuracy between time $t$ = 61 to 167 days.

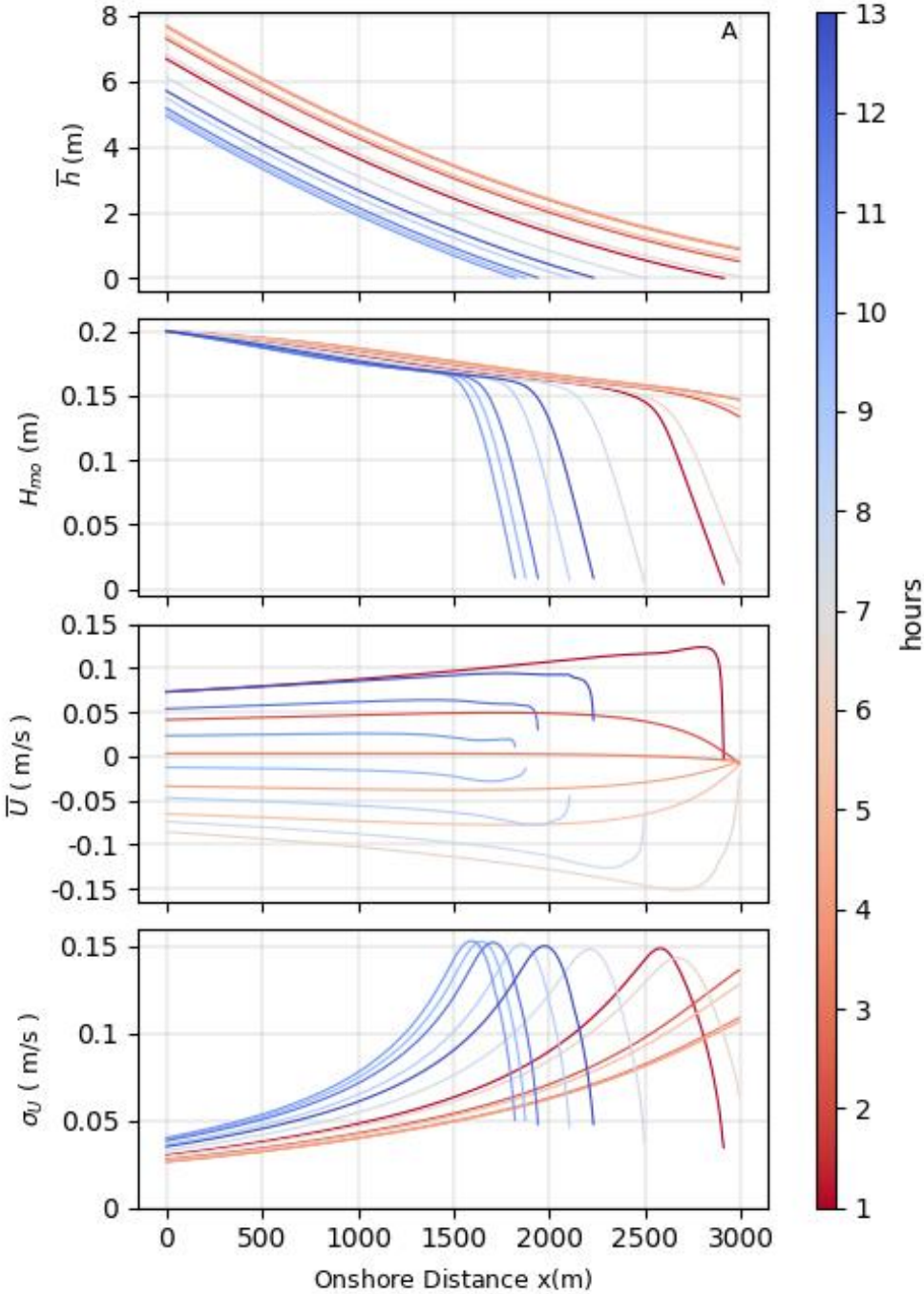


Figure 4.18: Hourly cross-shore variation of mean water depth ($\bar{h}$), significant wave height ($H_{m0}$), mean ($\bar{U}$) and standard deviation ($\sigma_U$) of cross-shore velocity ($U$) at beginning of A interval

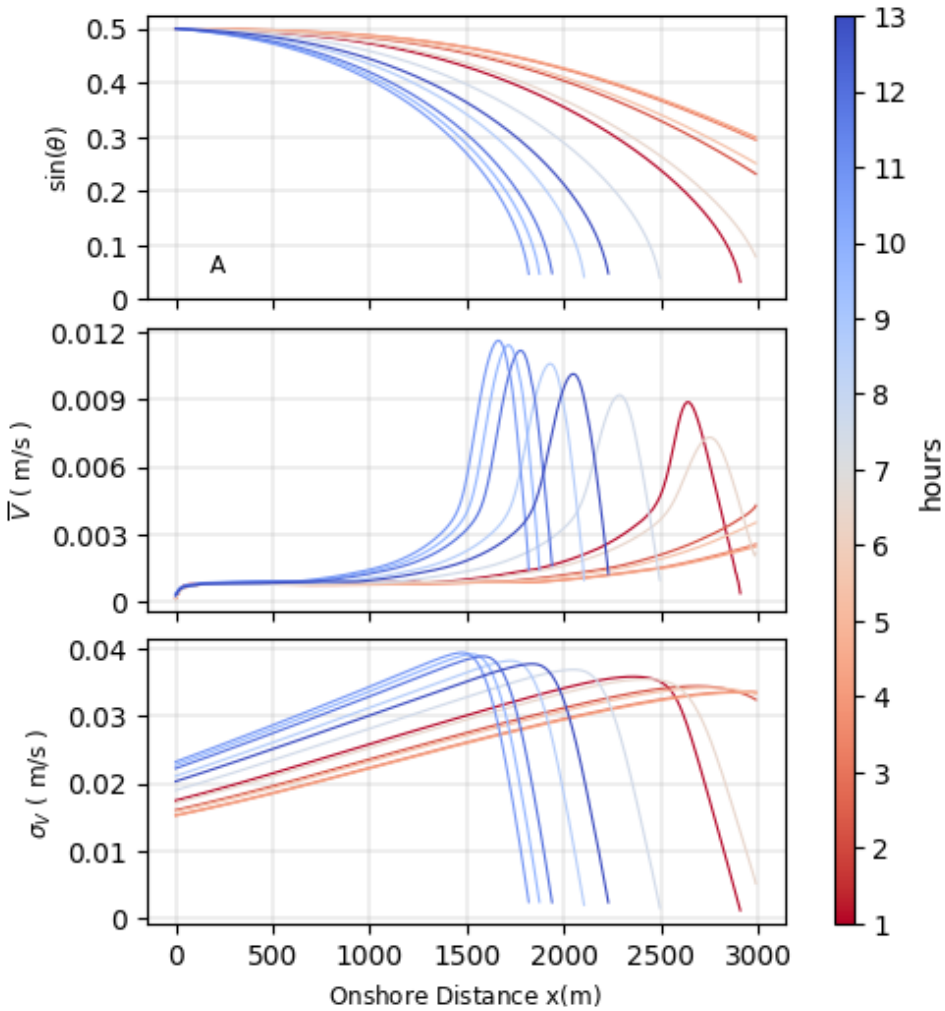


Figure 4.19: Hourly cross-shore variation of $\sin\theta$ ($\theta$ = wave angle), mean ($\bar{V}$) and standard deviation ($\sigma_V$) of longshore velocity ($V$) at beginning of A interval

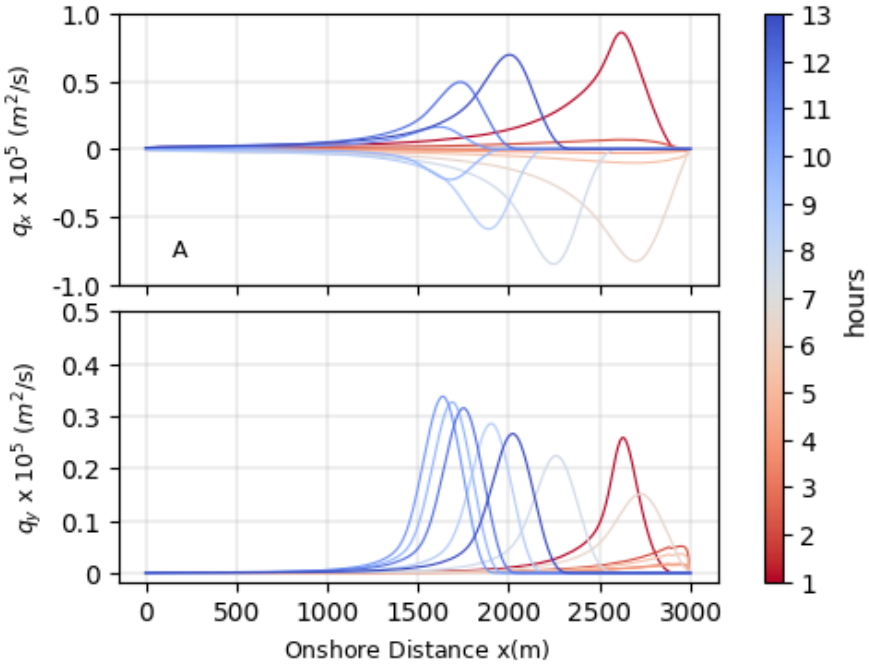


Figure 4.20: Hourly cross-shore variation of cross-shore sediment transport rate ($q_x$) and longshore sediment transport rate ($q_y$) at the beginning of A interval

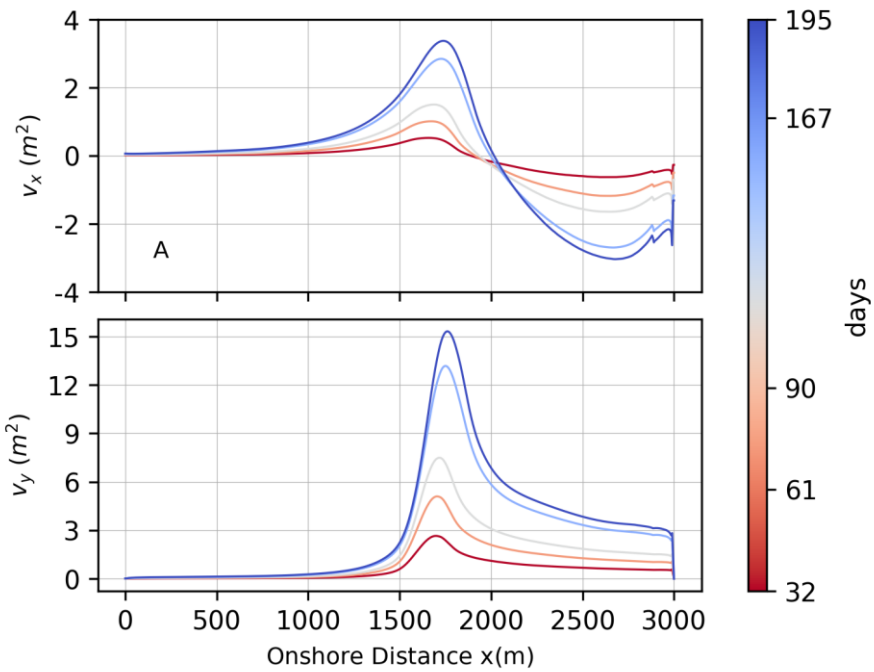


Figure 4.21: Cross-shore variation of cumulative sediment transport volumes $v_x$ and $v_y$ calculated by integrating $q_x$ and $q_y$ from time $t$ = 0 to $t$ = 32, 61, 90, 167, and 195 days during A interval

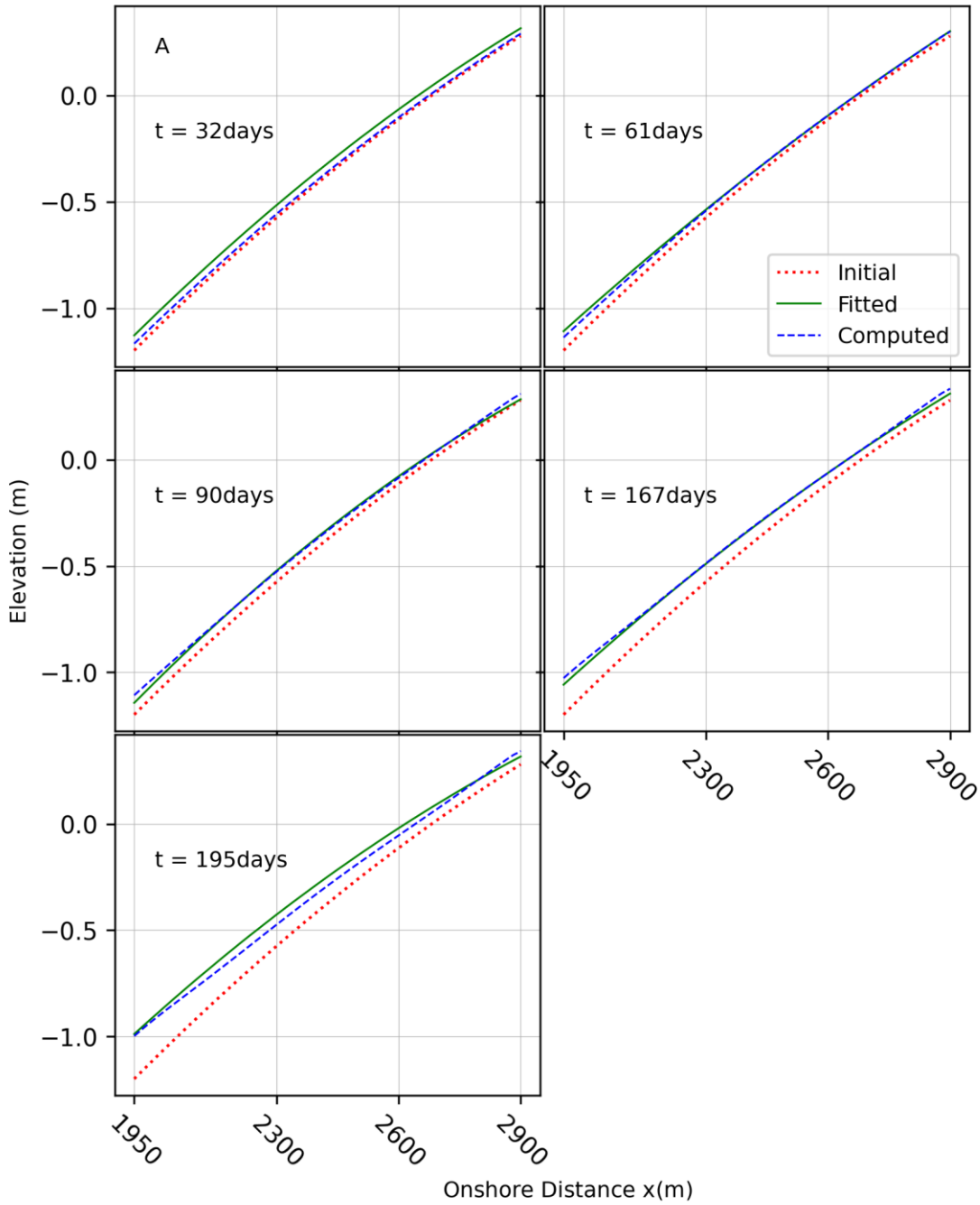


Figure 4.22: Comparison of fitted and computed mudflat profiles relative to initial profile at $t$ = 32, 61, 90, 167 and 195 days during A interval

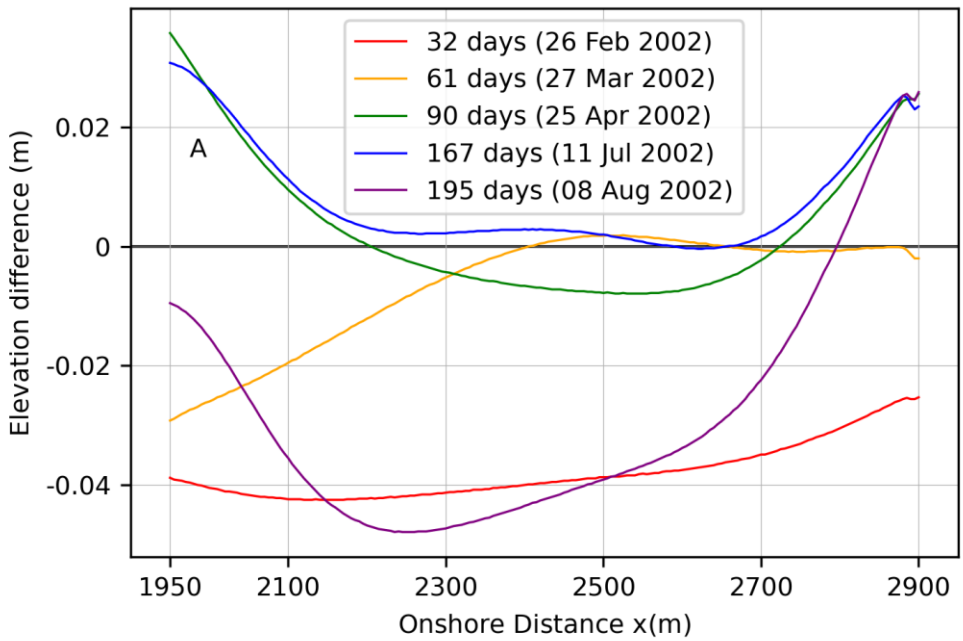


Figure 4.23: Deviation of computed mudflat profile from fitted profile at time $t$ = 32, 61, 90, 167 and 195 days during A interval

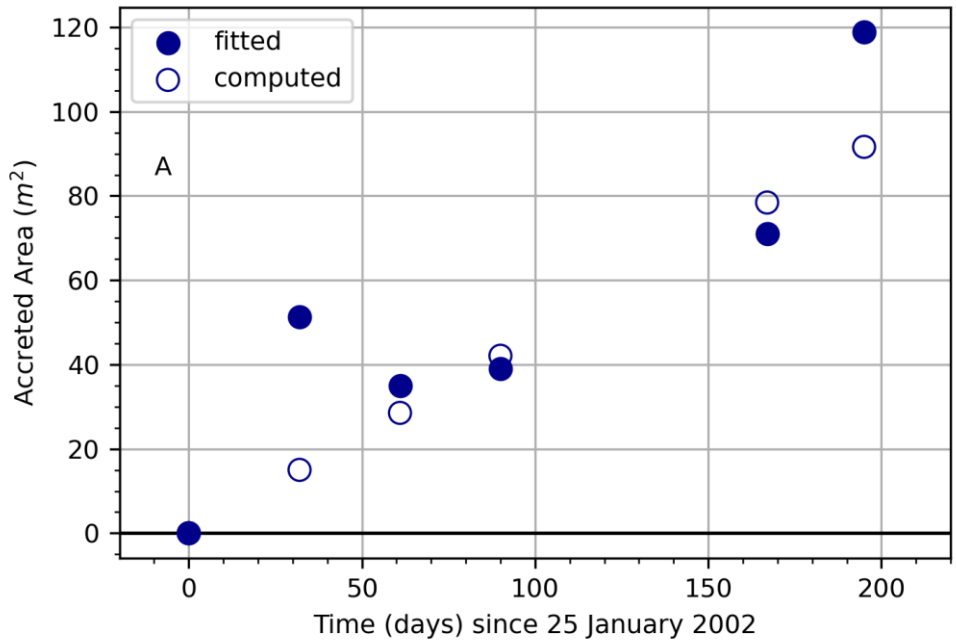


Figure 4.24: Comparison of fitted and computed eroded areas during A interval

### 4.2.2 Alongshore uniform case of IQYDY = 0

An alongshore uniform case was done to compare with the basic case and quantify deviation when there is no sediment loss in the alongshore direction. This case neglected the third term in Eq. (9) therefore mudflat elevation change was only affected by cross-shore sediment transport.

Fig. 4.25 presents the cumulative sediment volumes $v_x$ and $v_y$ per unit width as a function of $t$ for the alongshore uniform case during A interval. In comparison with the basic case, the longshore volume was significantly lower offshore of the breaker zone while the cross-shore volume was similar.

The lack of longshore sediment loss resulted in weak accretion along the profile. Both Figs. 4.26 and 4.27 display minimal accretion along most of the profile and a slight erosion at the landward end. This suggests that the profile was at some equilibrium state given the offshore wave conditions.

The amount of accreted area by the alongshore uniform case in Fig. 4.28 shows negligible accretion from a purely cross-shore sediment transport model. This case demonstrated that the mudflat profile evolution at this site during A interval is a 2D process.

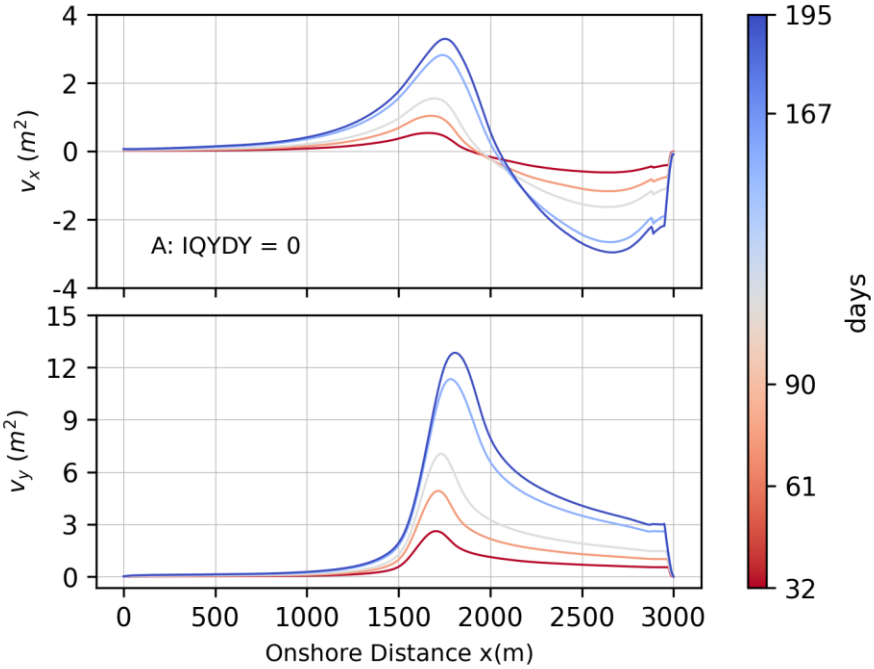


Figure 4.25: Cross-shore variation of cumulative sediment transport volumes $v_x$ and $v_y$ during A interval for alongshore uniform case of IQYDY = 0

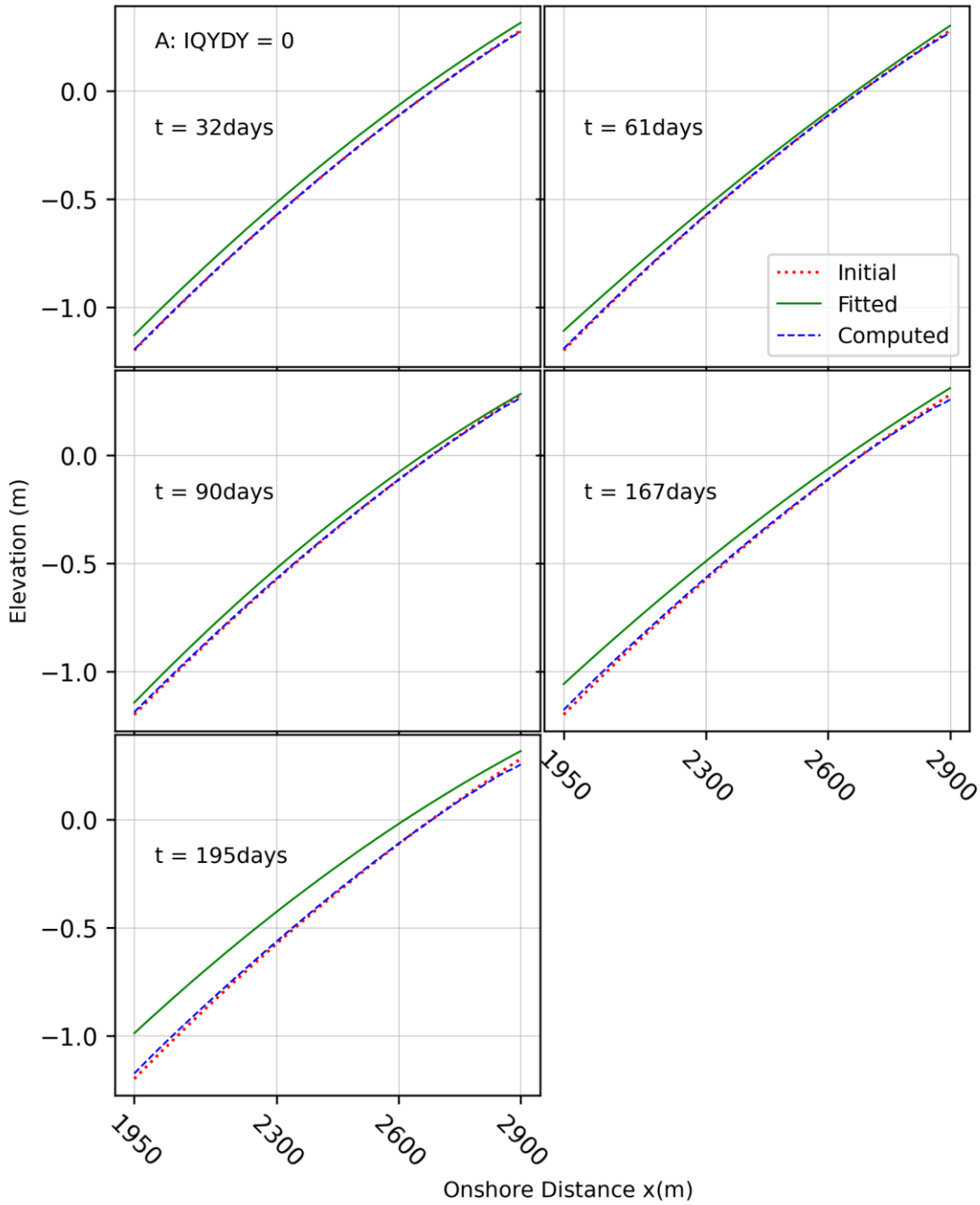


Figure 4.26: Comparison of fitted and computed mudflat profiles relative to initial profile during A interval for alongshore uniform case of IQYDY = 0

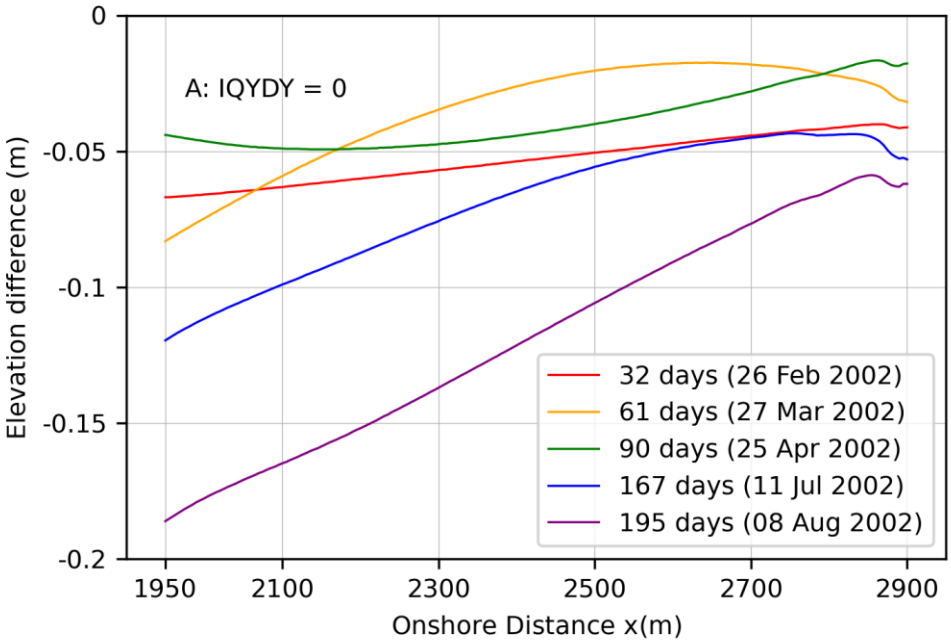


Figure 4.27: Deviation of computed mudflat profile from fitted profile at given time during A interval for alongshore uniform case of IQYDY = 0

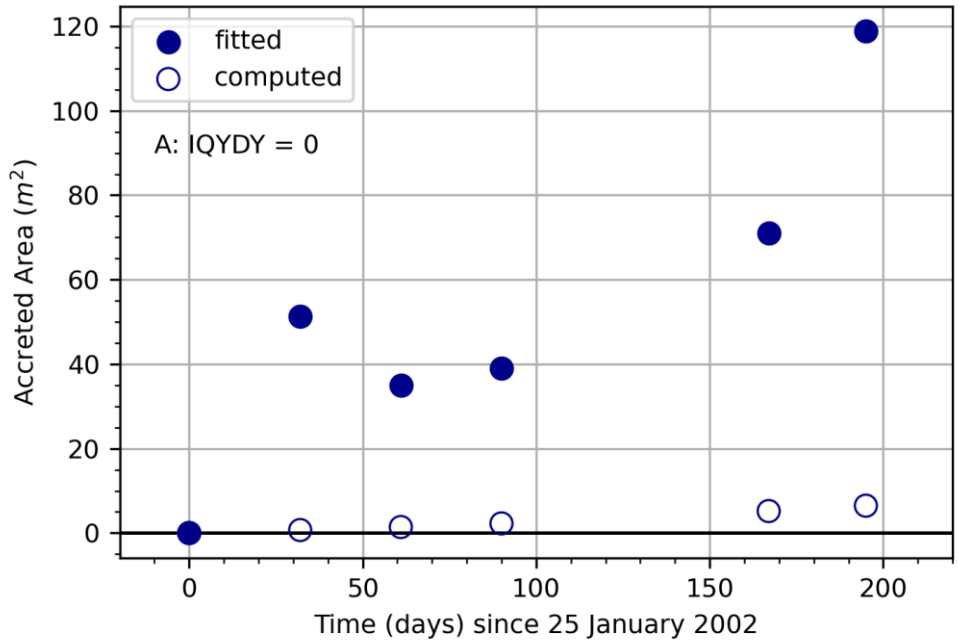


Figure 4.28: Comparison of fitted and computed accreted areas (negative implies net erosion) during A interval for alongshore uniform case of IQYDY = 0

### 4.2.3 Profile change sensitivity to increased (-$y_e$) = 200 m

A different equivalent alongshore length case was done to compare with the basic case and check for its sensitivity. This case affected the longshore sediment transport in Eq. (10).

Fig. 4.29 presents the cumulative sediment volumes $v_x$ and $v_y$ per unit width as a function of $t$ for equivalent alongshore length (-$y_e$) = 200 m case during A interval. In comparison with the basic case, the longshore volume was slightly lower offshore of the breaker zone while the cross-shore case was almost the same.

Fig. 4.30 displays a reduced rate of accretion of the mudflat profile especially towards the latter end of the A interval compared with the basic case. This reduced rate was still of reasonable agreement with the fitted profiles until $t$ = 167 days. After this time, the seaward end of the profile was unable to keep pace with the accretion of the fitted profile.

Fig. 4.31 shows the deviation of the computed profiles from the fitted profile. The computed profiles were able to consistently reproduce most of the profiles fairly well until $t$ = 167 days. This was evidenced by the elevation difference at about 0.05 m. The final data point in the A interval showed significant elevation difference at the seaward end.

Fig. 4.32 presents the amount of accretion for both the fitted and computed results of the equivalent alongshore length (-$y_e$) = 200 m along the entire measured profile during the A interval. The computed profiles showed a monotonic increase in accretion although noticeably less than that of the basic case. However, the error between time $t$ = 61 and 167 days did not improve while for time $t$ = 32 and 195 days worsened. This case demonstrated that CSHORE cannot satisfactorily predict temporal change in accreted area with a constant value of $y_e$.

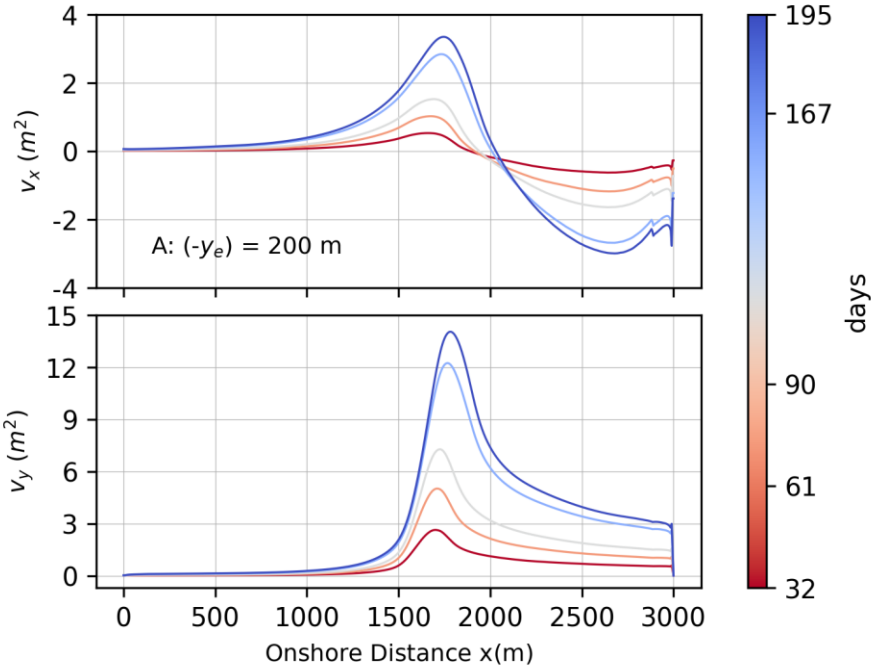


Figure 4.29: Cross-shore variation of cumulative sediment transport volumes $v_x$ and $v_y$ during A interval for increased (-$y_e$) = 200 m

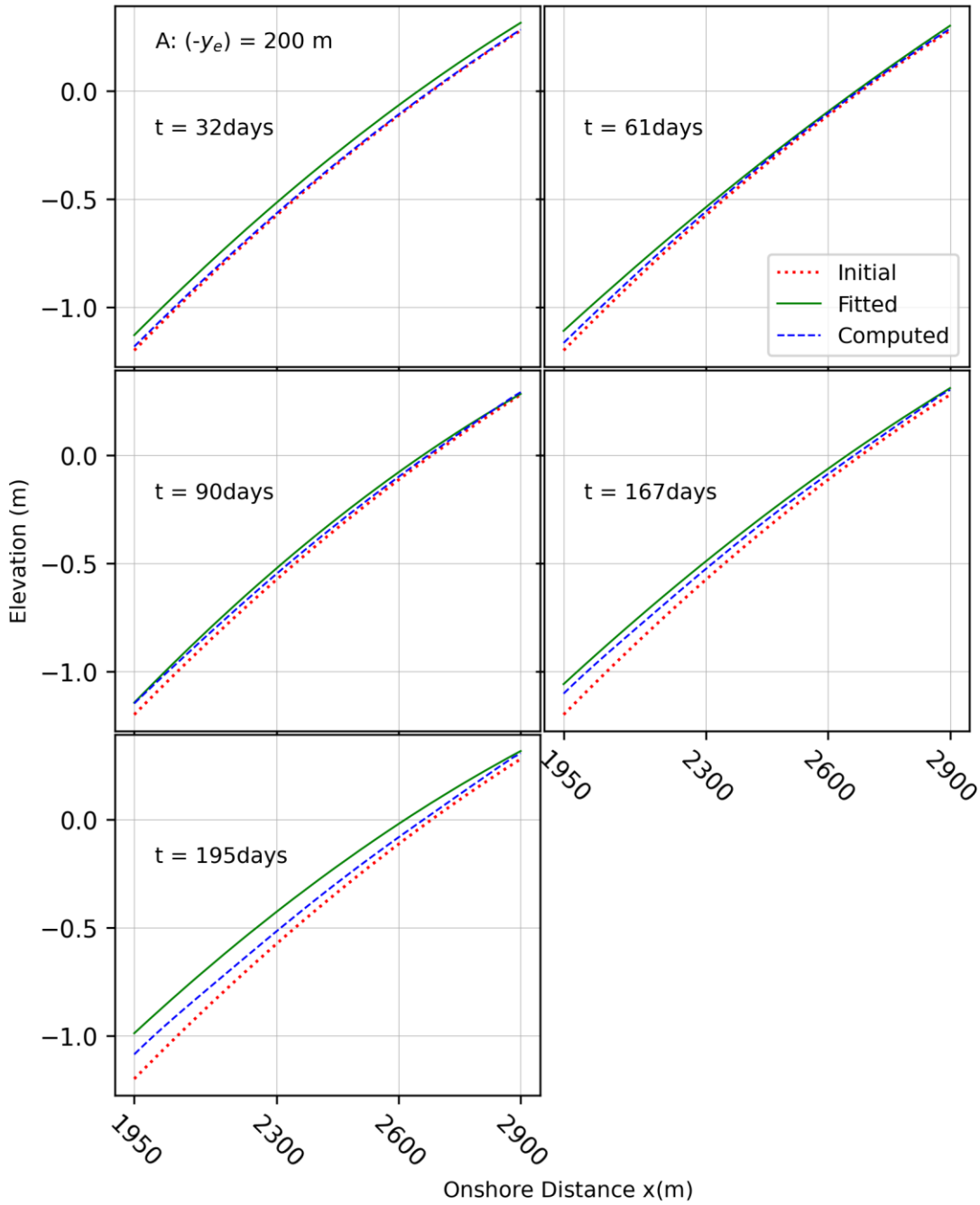


Figure 4.30: Comparison of fitted and computed mudflat profiles relative to initial profile during A interval for increased (-$y_e$) = 200 m

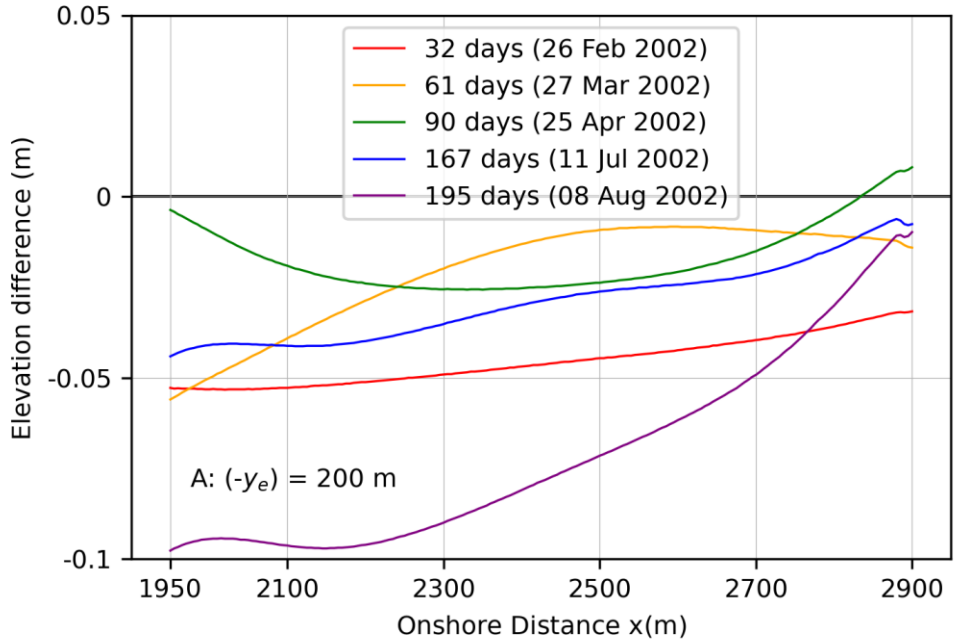


Figure 4.31: Deviation of computed mudflat profile from fitted profile at given time during A interval for increased (-$y_e$) = 200 m

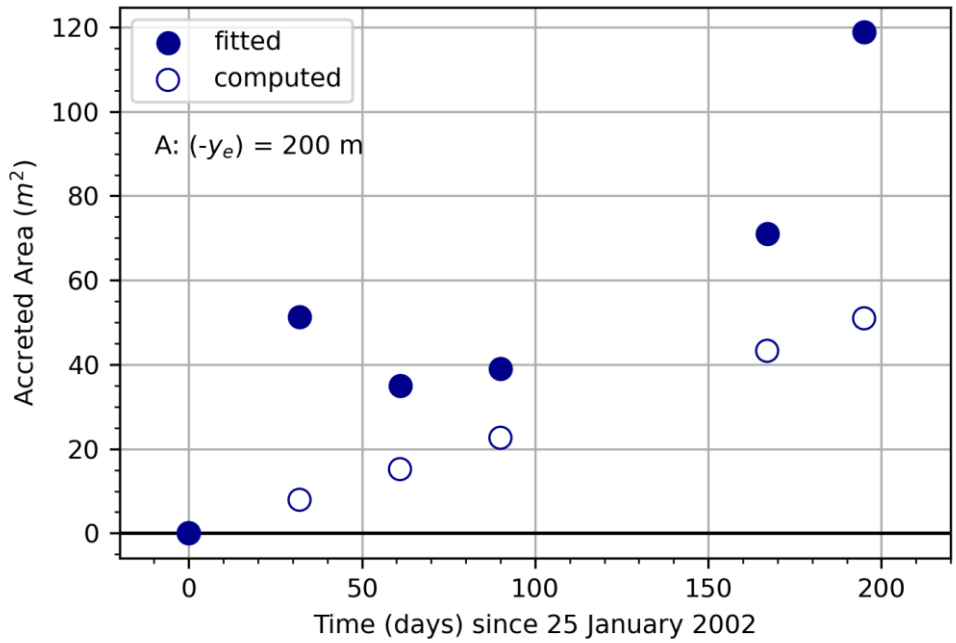


Figure 4.32: Comparison of fitted and computed accreted areas during A interval for increased (-$y_e$) = 200 m

# Chapter 5

# SENSITIVITY OF COMPUTED RESULTS

CSHORE includes a number of parameters to characterize the sediments, tides, waves, and currents. The basic input parameters in Table 3.1 may have reproduced the mudflat profile changes during the E and A intervals however, it is also important to understand which parameters affect the profile evolution and to what degree.

This chapter focuses on quantifying the sensitivity of each parameter to the computed results. The following sections will discuss different input parameters and quantify their effect on profile evolution. The parameters tested were mud characteristics, tidal amplitudes, and incident wave parameters.

## 5.1 Mud Characteristics and Volume Fraction

The effective mud fall velocity $w_e$ was increased from 0.2 $\mathrm{mm/s}$ to 0.4 $\mathrm{mm/s}$. Fig. 5.1 compares the fitted and computed areas for both effective mud fall velocities during the E and A intervals. The comparison was done to indicate the degree of sensitivity relative to the fitted values.

The increase of $w_e$ by a factor of 2 decreased the suspended mud volume $V_m$ and the mud transport rates $q_{mx}$ and $q_{my}$ in Eq. (7) by a factor of 2. The sediment transport rates $q_x$ and $q_y$ in Eqs. (5) and (6) were determined mostly by $q_{mx}$ and $q_{my}$. The decrease in sediment transport rates in Eq. (10) reduced the increment of $z_b$ and the eroded or accreted area by a factor of about 2. The eroded or accreted area for $w_e$ = 0.4 $\mathrm{mm/s}$ in Fig. 5.1 is similar to that of $y_e$ (positive or negative) = 200 m in Figs. 4.16 and 4.32.

Fig. 5.2 shows the deviation of the computed profiles from the fitted profile for both the E and A intervals. Fig. 5.2 (top) shows profiles from time $t$ = 150 to 206 days with a positive elevation difference at the seaward end which is evidence of lower erosion rates towards the end of the E interval when compared with Fig. 4.7. For the A interval, the more negative elevation difference in Fig. 5.2 (bottom) towards the end of the interval presents the evidence of lower accretion rates.

Next, the mudflat profile evolution was compared with the evolution of a sandier flat, that is to say $f_m$ = 0.3 and $f_s$ = 0.7. Fig. 5.3 compares the fitted and computed areas for both mud volume fractions during the E and A intervals, respectively. The sand transport rates $q_{bx}$, $q_{by}$, $q_{sx}$, and $q_{sy}$ were small in comparison with the mud transport rates $q_{mx}$ and $q_{my}$. The sediment transport rates $q_x$ and $q_y$ were reduced by a factor of about 7/3, resulting in reduced erosion and accretion areas. Sand placement on an eroding mudflat may be effective in reducing mudflat erosion.

Fig. 5.4 shows the deviation of the computed profiles from the fitted profile for the E and A intervals, respectively. Fig. 5.4 (top) shows a positive elevation difference at the seaward end during the second half of the E interval. The trend is almost similar to that of the case for $w_e$ = 0.4 $\mathrm{mm/s}$. For the A interval, the more negative elevation difference in Fig. 5.4 (bottom) compared with Fig. 4.23 towards the end of the interval similarly presents evidence of lower rates of accretion.

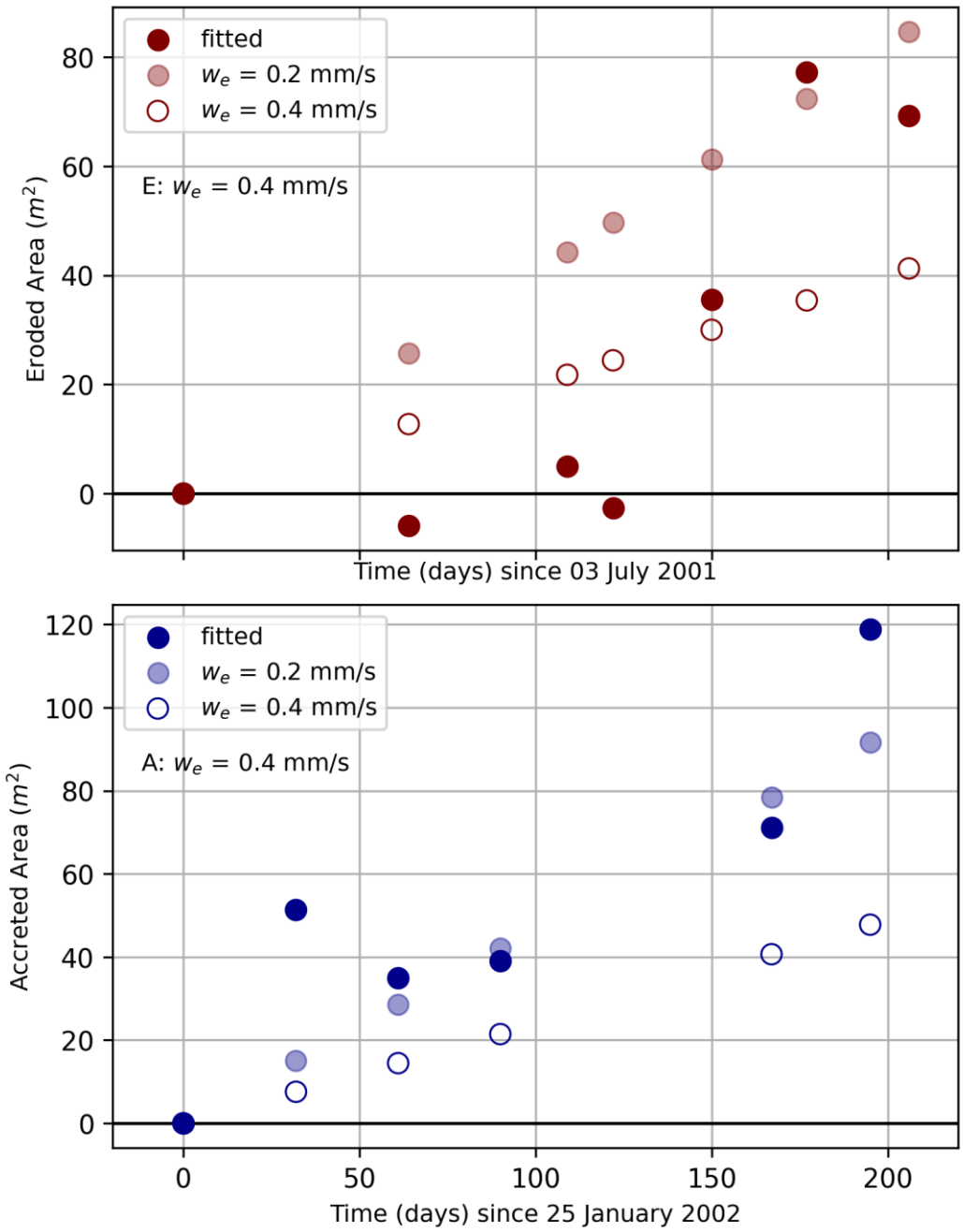


Figure 5.1: Comparison of fitted and computed eroded areas (negative implies net accretion) during E interval (top) and accreted areas during A interval (bottom) for mud fall velocity $w_e$ = 0.2 and 0.4 mm/s

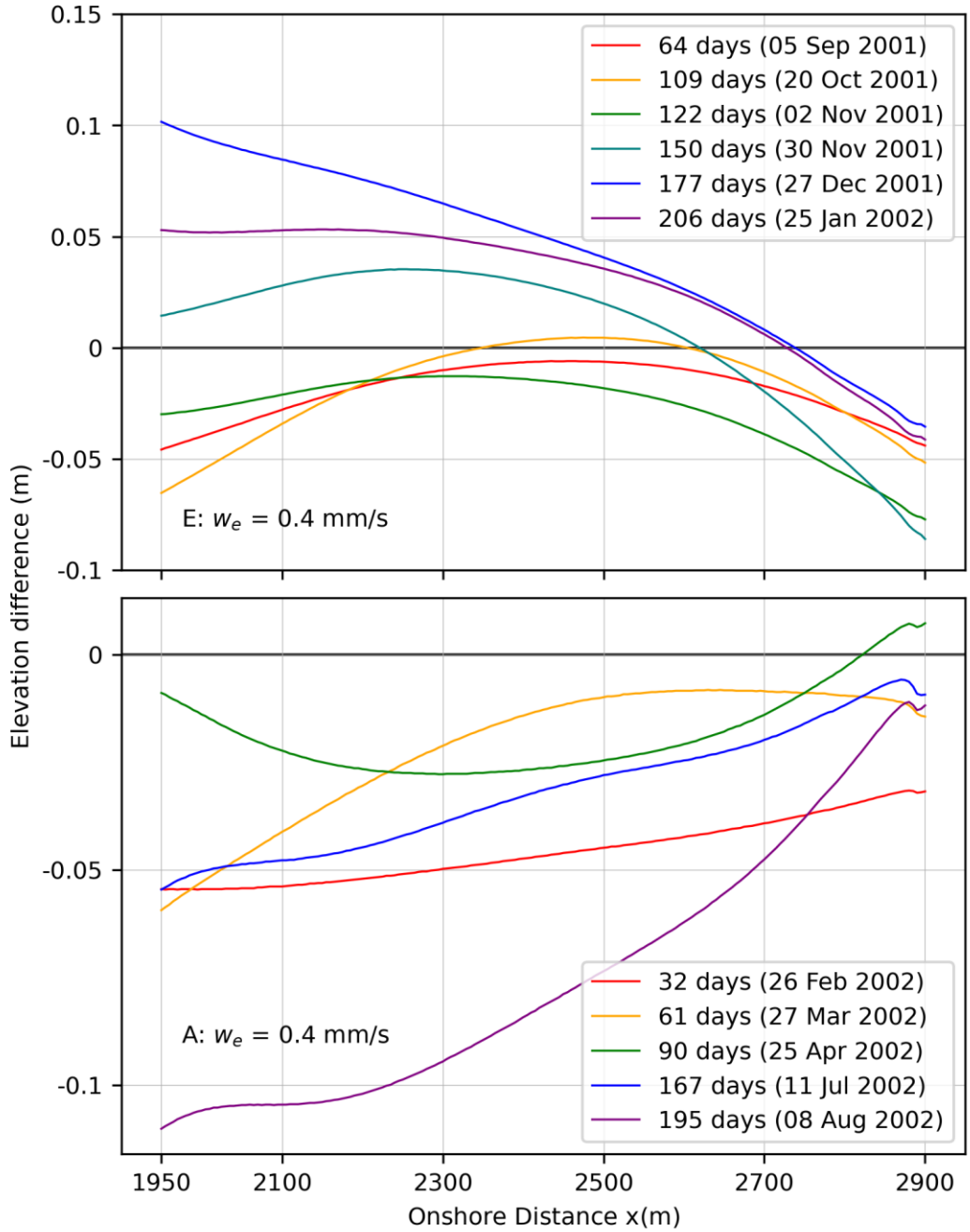


Figure 5.2: Deviation of computed mudflat profile from fitted profile at time $t$ = 64, 109, 122, 150, 177 and 206 days during E interval (top) and time $t$ = 32, 61, 90, 167 and 195 days during A interval (bottom) for $w_e$ = 0.4 mm/s

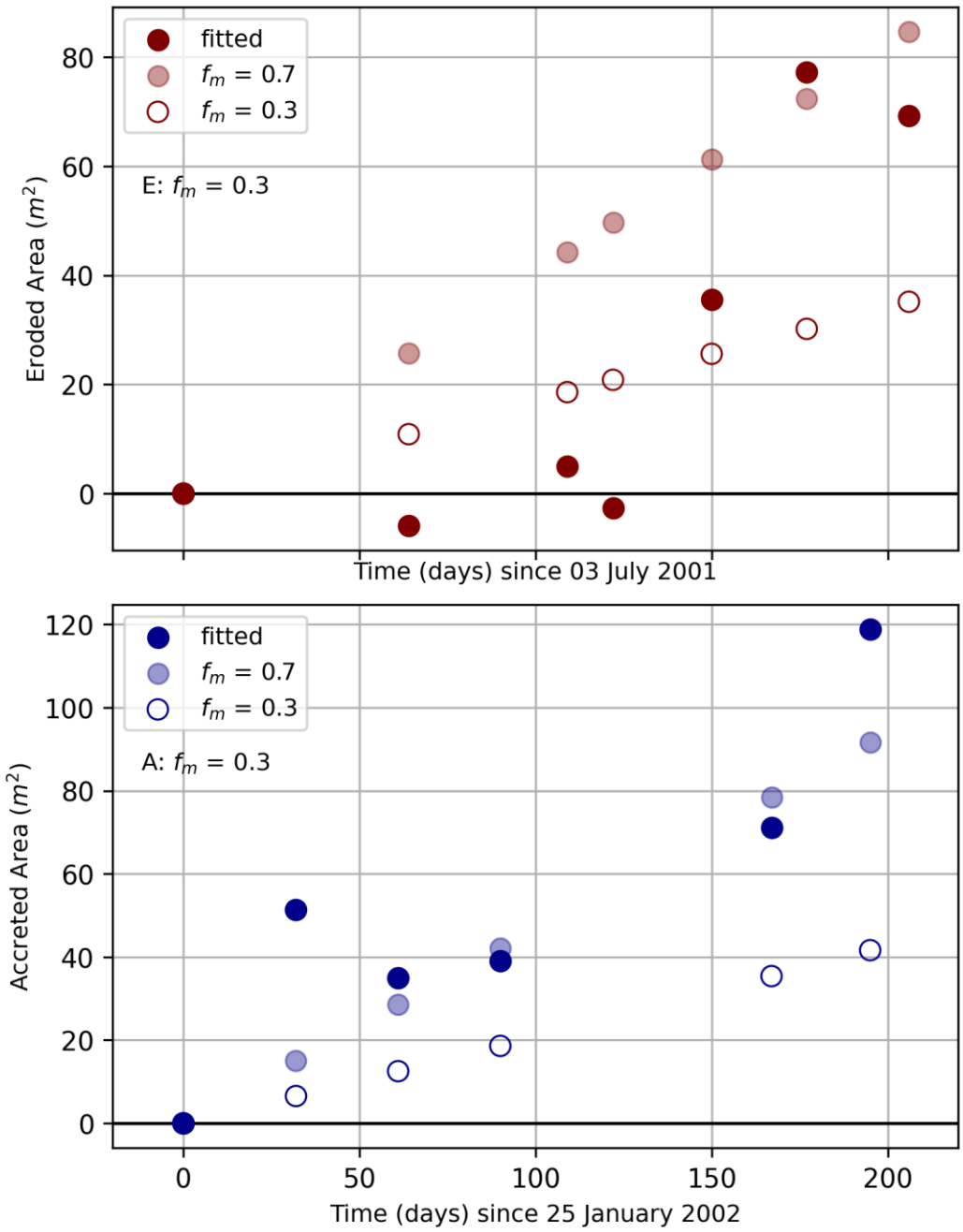


Figure 5.3: Comparison of fitted and computed eroded areas (negative implies net accretion) during E interval (top) and accreted areas during A interval (bottom) for mud volume fraction $f_m$ = 0.3 and 0.7

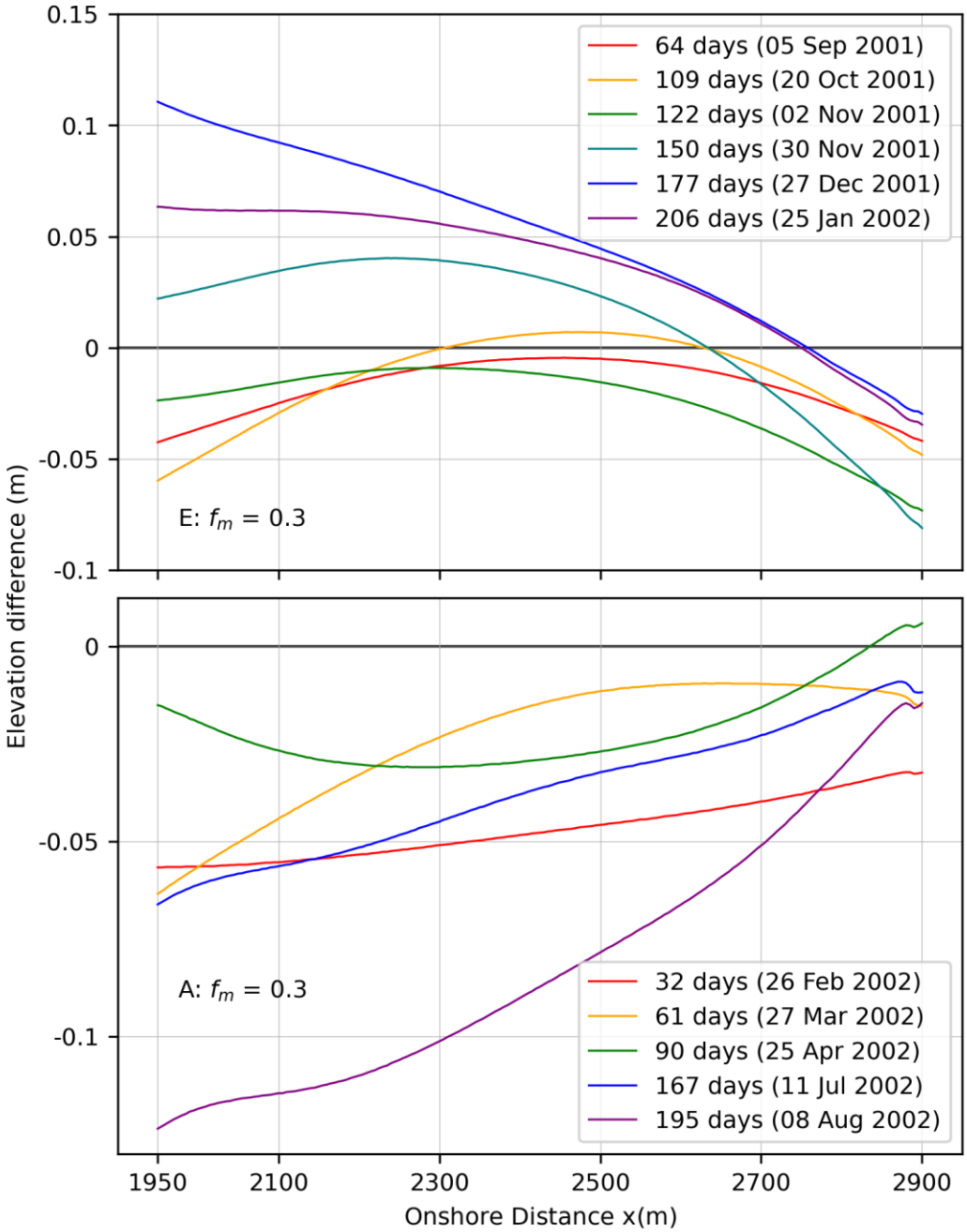


Figure 5.4: Deviation of computed mudflat profile from fitted profile at time $t$ = 64, 109, 122, 150, 177 and 206 days during E interval (top) and time $t$ = 32, 61, 90, 167 and 195 days during A interval (bottom) for $f_m$ = 0.3

## 5.2 Tide Amplitudes $A_y$ and $A_t$

The water level in Eq. (11) was different depending on the interval simulated. The E interval had lower water levels when the mudflat eroded while the A interval had higher water levels during mudflat accretion. Computations were done for the case of no yearly water level oscillation, $A_y$ = 0. The time series input for water levels during the E and A intervals are shown in Fig. 5.5.

Fig. 5.6 compares the eroded and accreted areas of cases with and without a yearly water level oscillation. The direct effect of $A_y$ on the mudflat profile appears to be negligible in the case of the E interval or minimal in the case of the A interval.

Fig. 5.7 presents the deviation of the computed mudflat profile from the fitted profile. In comparison, the resulting profiles did not differ much from the basic case in Figs. 4.7 and 4.23. This was the reason the equivalent alongshore length $y_e$ has been selected to be either positive (E) or negative (A).

Another case was done to inspect the effect of the semidiurnal tide amplitude $A_t$ in Eq. (11). A reduced semidiurnal tide amplitude of $A_t$ = 0.72 m was used instead of the value for the basic case $A_t$ = 1.44 m. The time series input for water levels during the E and A intervals are shown in Fig. 5.8.

The reduction of the semidiurnal tide amplitude $A_t$ by a factor of 2 resulted in an increase in eroded area by about 1.5 and in accreted area by about 2. Fig. 5.9 presents the temporal evolution of eroded and accreted areas.

The E interval evolution in Fig. 5.10 (top) shows a lower elevation difference (more erosion) at the middle portion of the fitted profile compared with Fig. 4.7. With a lower water level from the reduced semidiurnal tide amplitude, wave breaking occurred more frequently on the mudflat unlike in the basic case. The same can be said in Fig. 5.10 (bottom) that shows an increase in the amount of sediment accreted in

the same middle portion of the profile. The frequency of breaking and the associated longshore mud transport were what was driving the profile change. The change in semidiurnal tide amplitude affects the water depth and wave breaking.

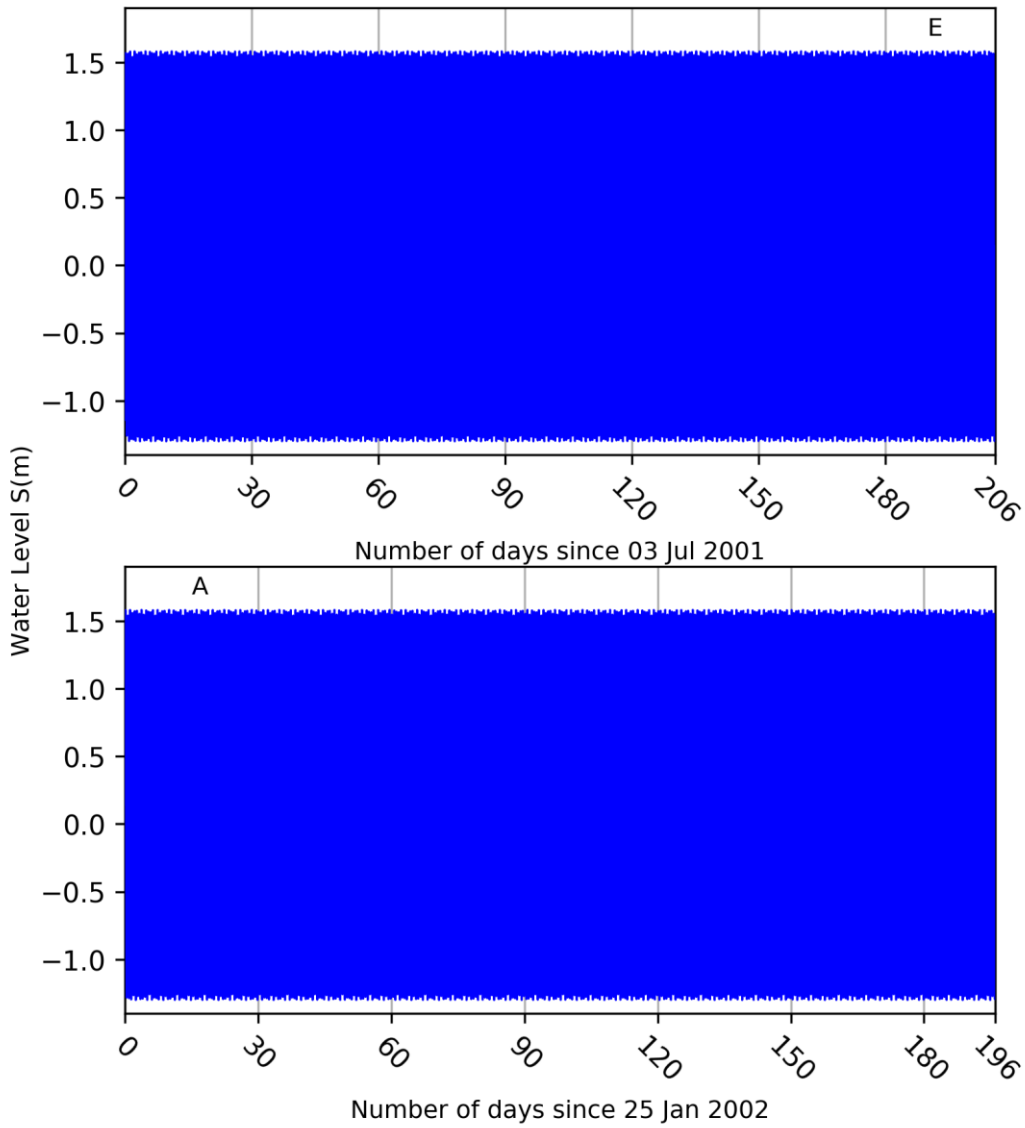


Figure 5.5: Time series of water level assumed for both E (top) and A (bottom) intervals with yearly water level variation, $A_y$, = 0

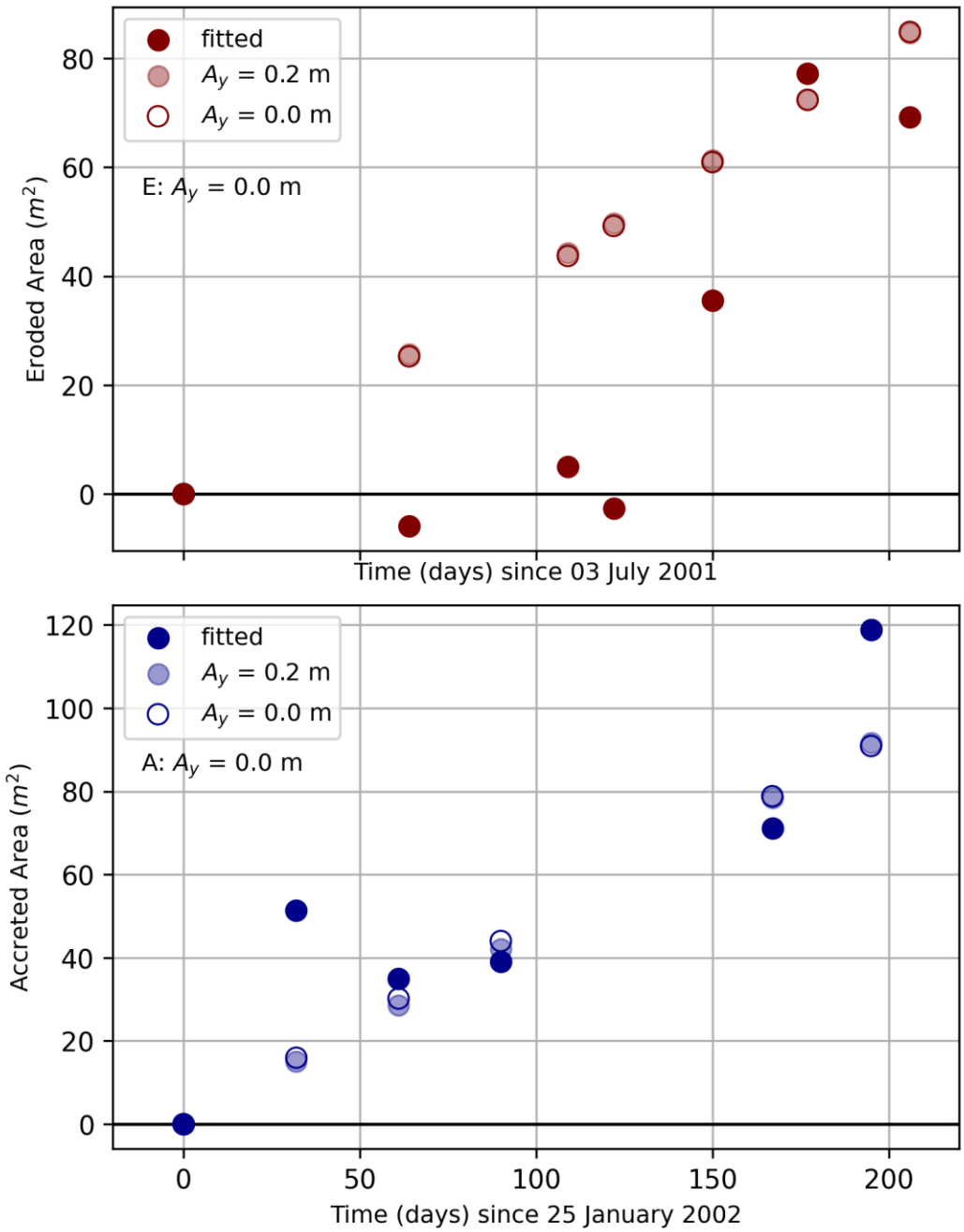


Figure 5.6: Comparison of fitted and computed eroded areas (negative implies net accretion) during E interval (top) and accreted areas during A interval (bottom) for yearly amplitudes $A_y$ = 0.0 and 0.2 m

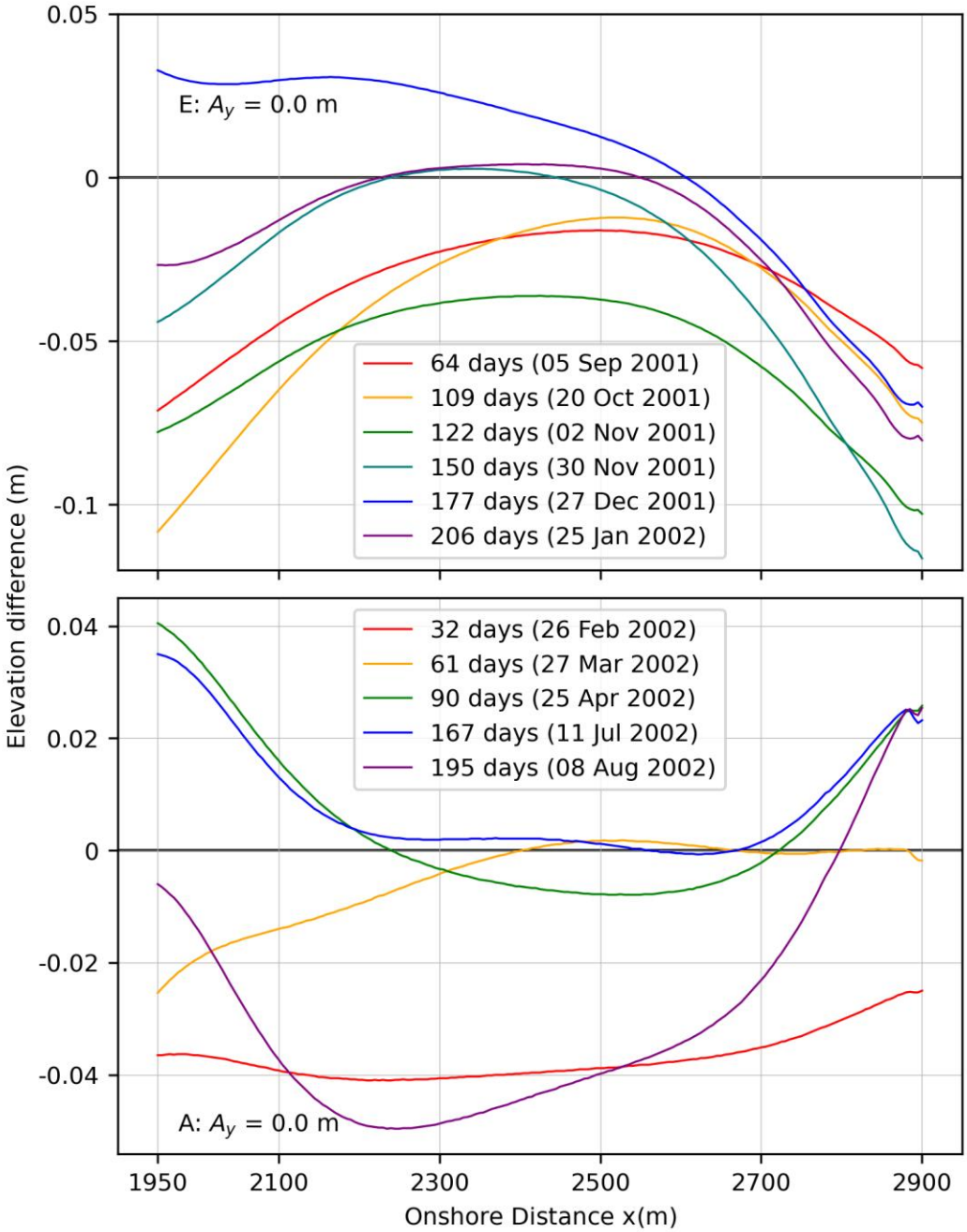


Figure 5.7: Deviation of computed mudflat profile from fitted profile at time $t$ = 64, 109, 122, 150, 177 and 206 days during E interval (top) and time $t$ = 32, 61, 90, 167 and 195 days during A interval (bottom) for $A_y$ = 0.0 m

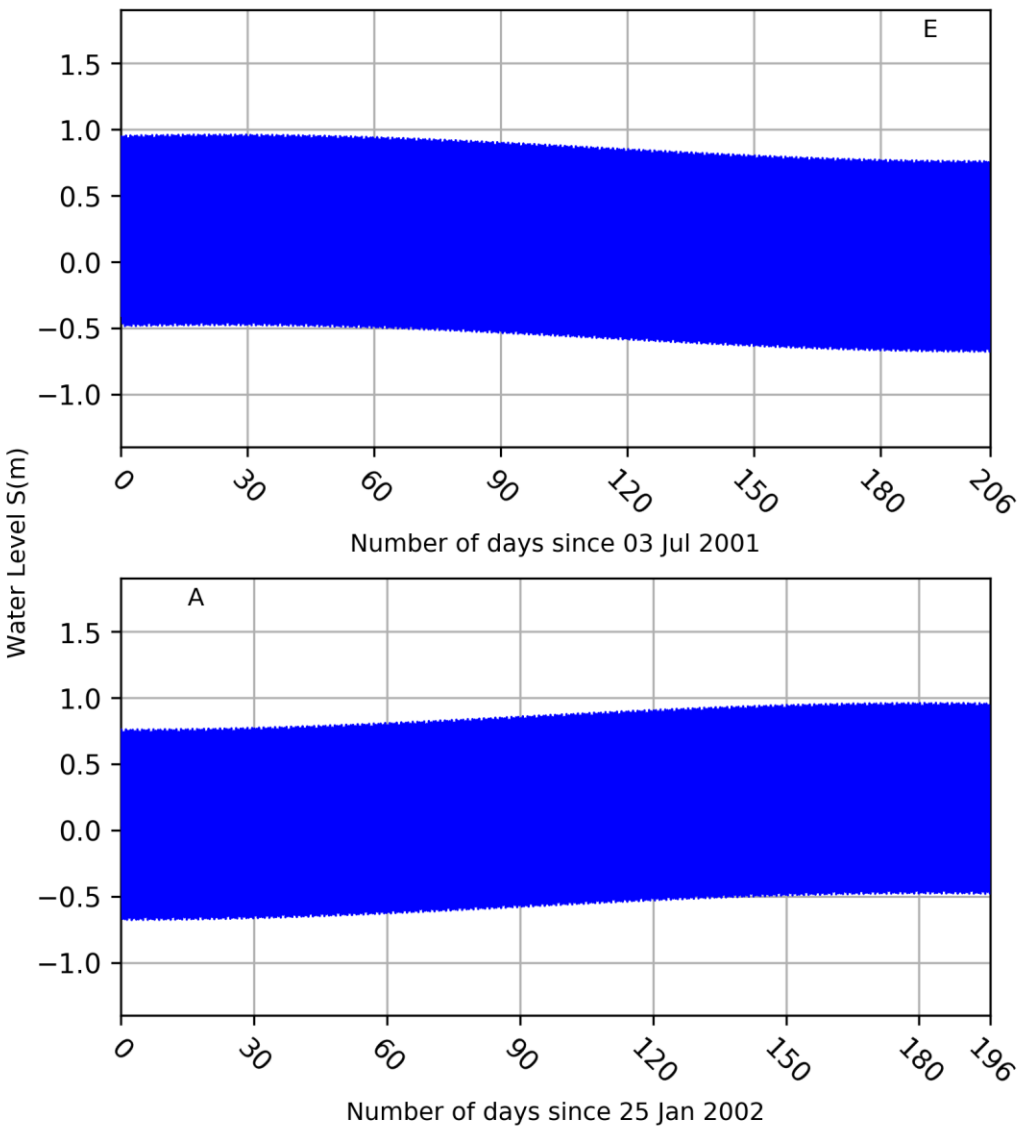


Figure 5.8: Time series of water level assumed for both E (top) and A (bottom) intervals with semidiurnal amplitude $A_t$ = 0.72 m

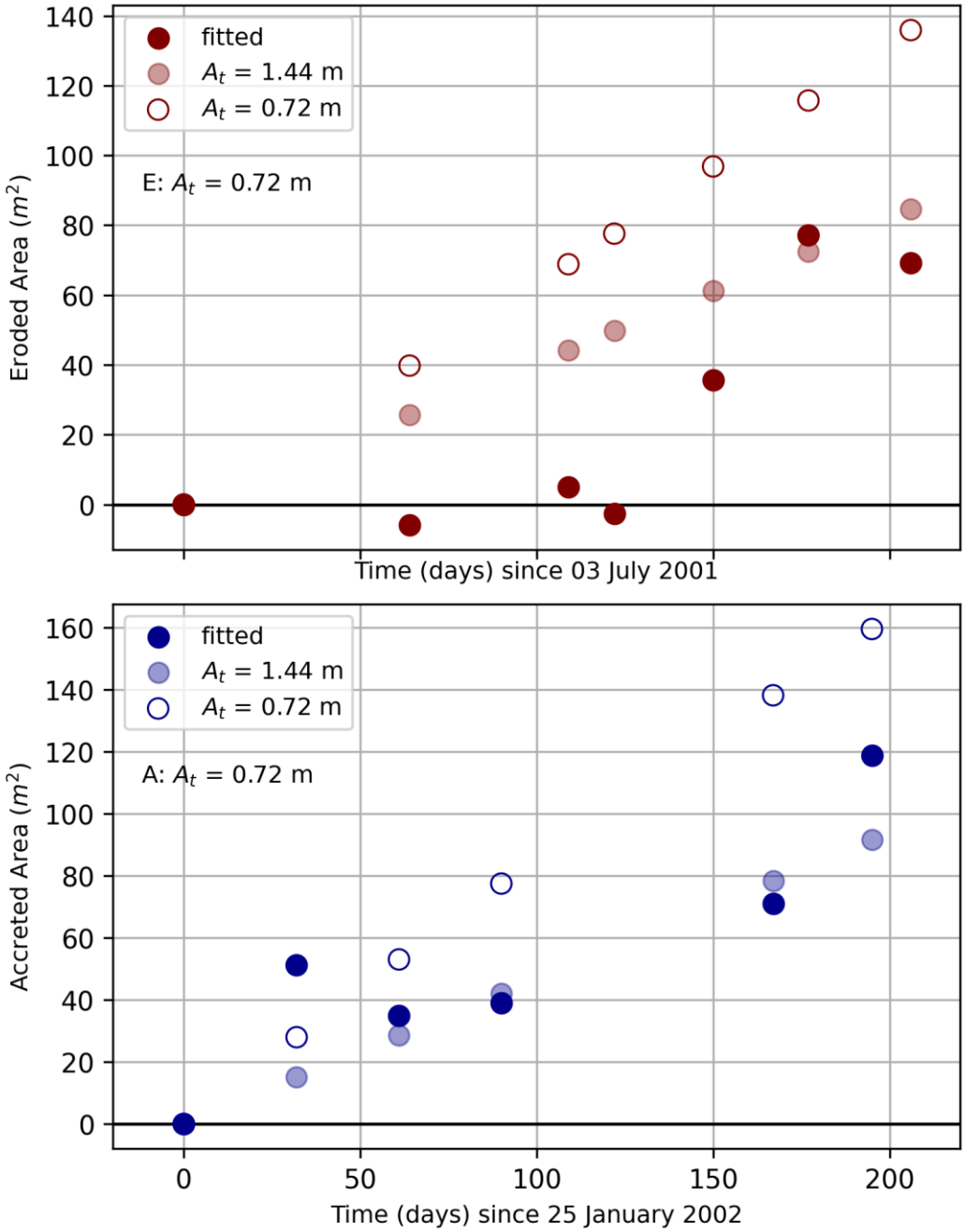


Figure 5.9: Comparison of fitted and computed eroded areas (negative implies net accretion) during E interval (top) and accreted areas during A interval (bottom) for semidiurnal amplitudes $A_t$ = 0.72 and 1.44 m

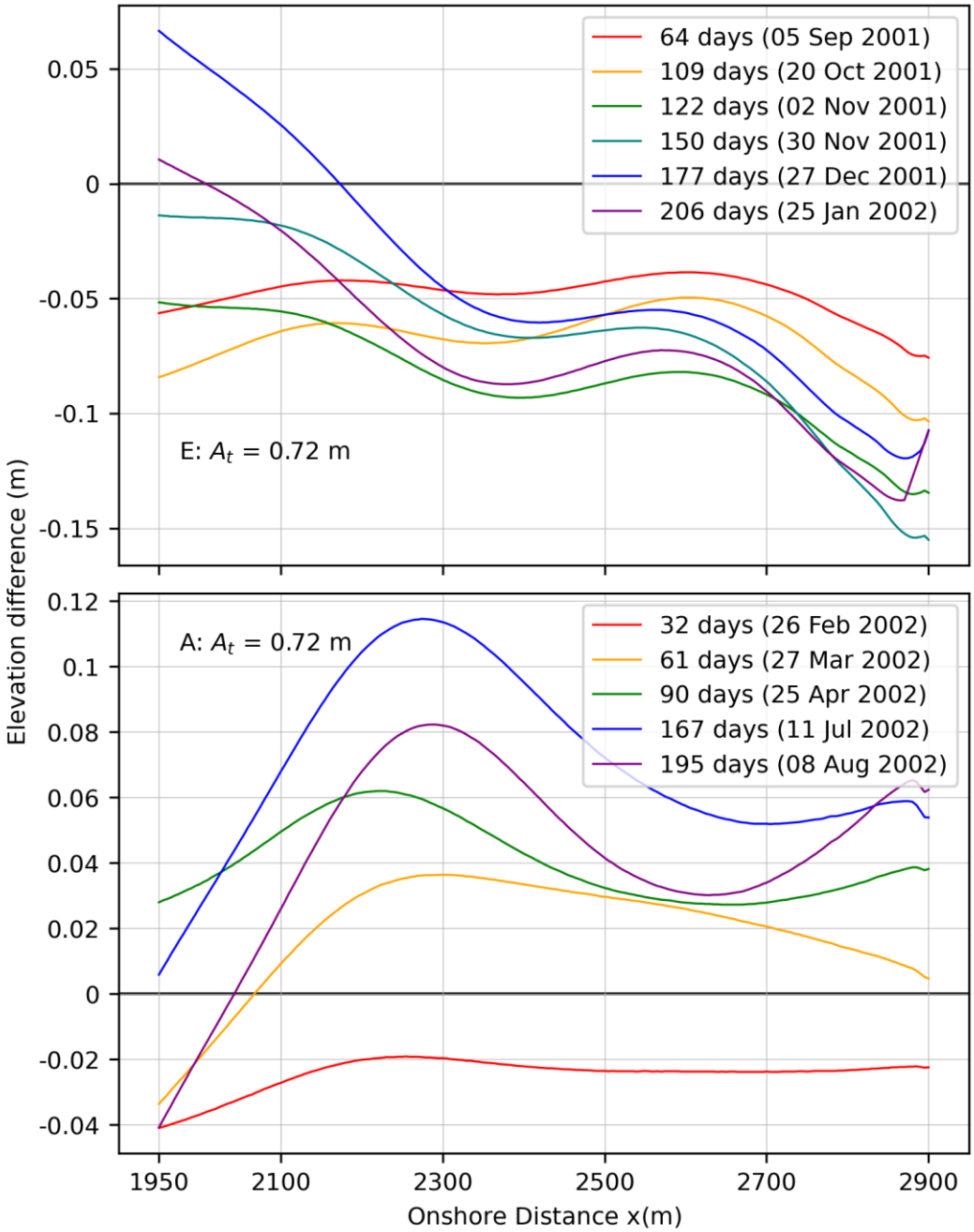


Figure 5.10: Deviation of computed mudflat profile from fitted profile at time $t$ = 64, 109, 122, 150, 177 and 206 days during E interval (top) and time $t$ = 32, 61, 90, 167 and 195 days during A interval (bottom) for $A_t$ = 0.72 m

## 5.3 Wave Height, Period, and Direction

The incident wave parameters used in the basic case were the average of the measured values at the field site. In reality, wave conditions change during either E or A interval.

First tested was the incident wave height. From the basic case, two more simulations were done to examine a larger ($H_{m0}$ = 0.3 m) and a smaller wave height. ($H_{m0}$ = 0.1 m). Fig. 5.11 presents the eroded and accreted areas of varying incident wave heights. During both intervals, the smaller wave height eroded or accreted negligible amounts while the larger wave height eroded and accreted more.

Figs. 5.12 and 5.13 present the same findings. The profile evolution at the top plot for either figure showed a positive and negative elevation difference for $H_{m0}$ = 0.1 m during E and A intervals, respectively. This illustrated the smaller rate of sediment transport from the lower incident wave height. The opposite can be observed in the lower plot for either figure. An excessively negative and positive elevation difference during the E and A intervals, respectively, displayed larger rates of sediment movement. The effect the incident wave height $H_{m0}$ has on profile evolution was evident in the wave-induced longshore mud transport brought about by wave breaking.

Next, the incident wave period was tested. From the basic case, two more simulations were done to examine a shorter ($T_p$ = 2 s) and a longer wave period. ($T_p$ = 4 s). Fig. 5.14 presents the eroded and accreted areas, respectively, of varying incident wave periods. During both intervals, the shorter wave period eroded or accreted smaller amounts while the longer wave period eroded and accreted more.

The wave period affects the cross-shore wave transformation and wave breaking on the mudflat. The effect of varying wave periods on the degree of erosion or accretion is conspicuous in Figs. 5.15 and 5.16.

Finally, the incident wave direction was examined. From the basic case, three more simulations were done: $\theta$ = 15°, 45°, and 60°. Fig. 5.17 presents the eroded and accreted areas of varying incident wave directions. During both intervals, a 45° incident wave direction had an almost similar effect as the base case while 15° and 60° had smaller eroded or accreted areas.

The incident wave angle does have some effect on the mudflat profile evolution but to a lesser extent than the effect of the incident wave period. The temporal elevation difference for 15°, 45° and 60° are presented in Figs. 5.18 and 5.19 for the E and A intervals. It is noted that incident wave angle was not measured at the field site and was only estimated from wind data. Given the smaller effects incident wave angle has on the profile evolution, the uncertainty of the input wave angle turns out to be less serious than initially hypothesized.

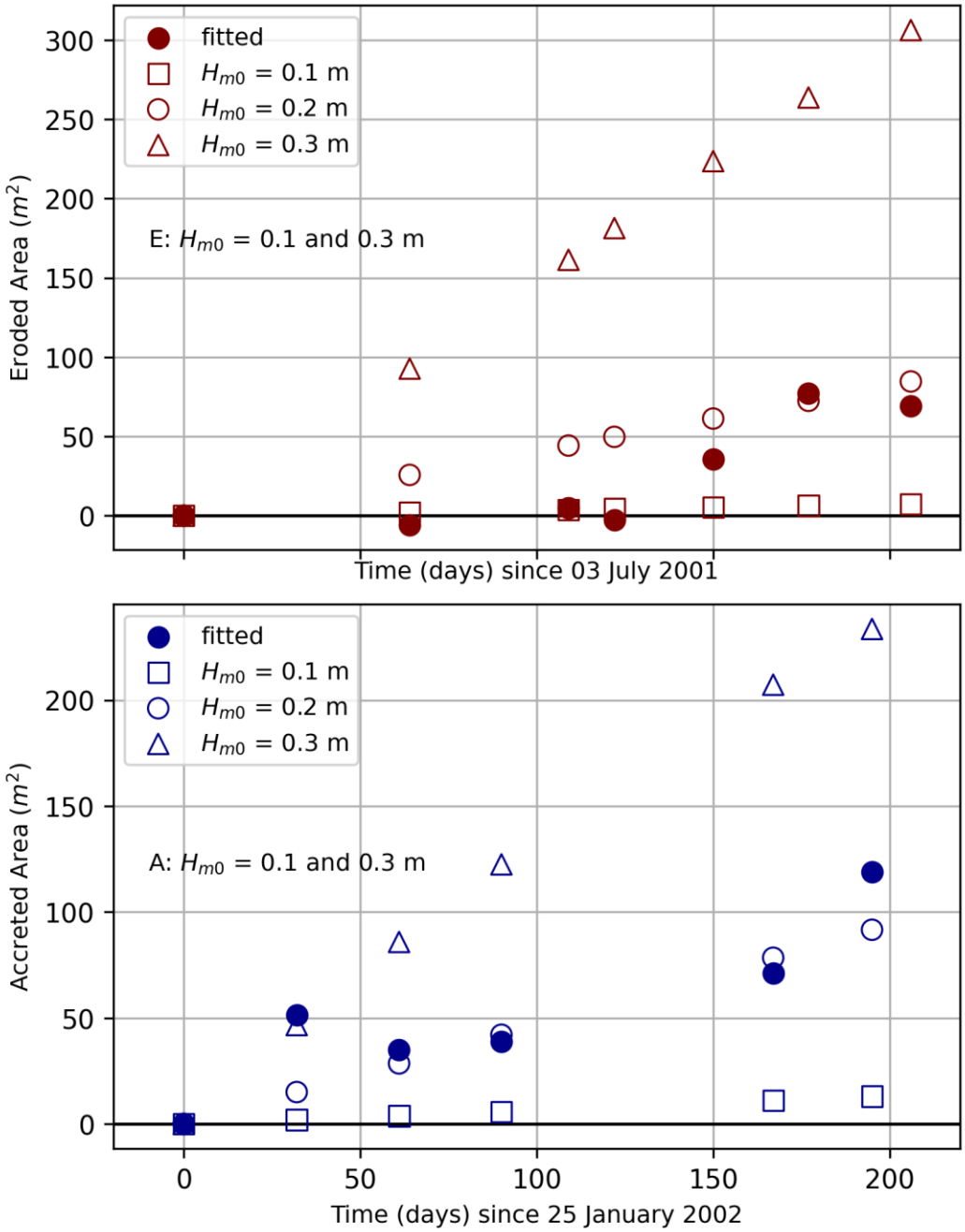


Figure 5.11: Comparison of fitted and computed eroded areas (negative implies net accretion) during E interval (top) and accreted areas during A interval (bottom) for wave height $H_{m0}$ = 0.1, 0.2 and 0.3 m

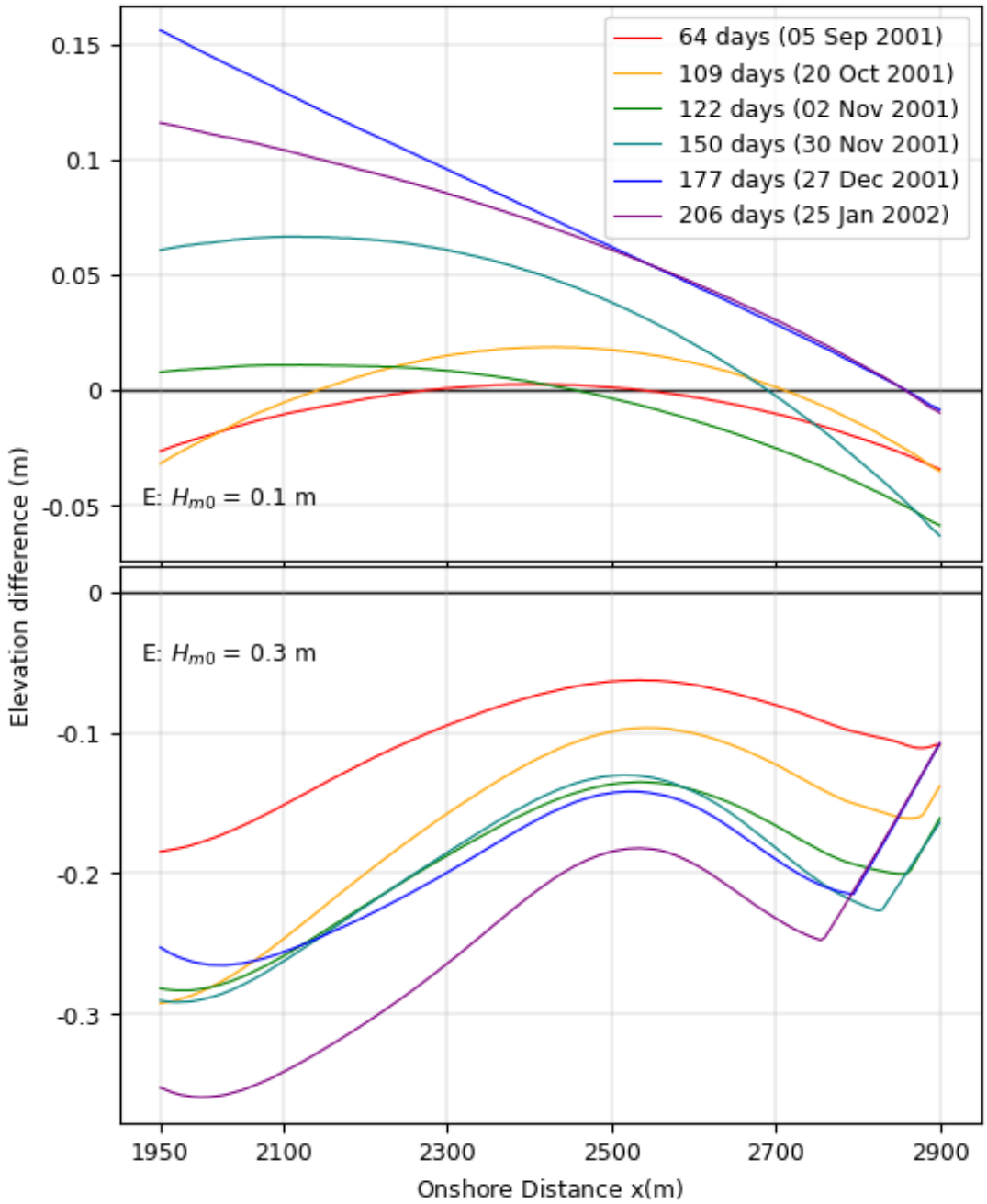


Figure 5.12: Deviation of computed mudflat profile from fitted profile at time $t$ = 64, 109, 122, 150, 177 and 206 days during E interval for $H_{m0}$ = 0.1 and 0.3 m

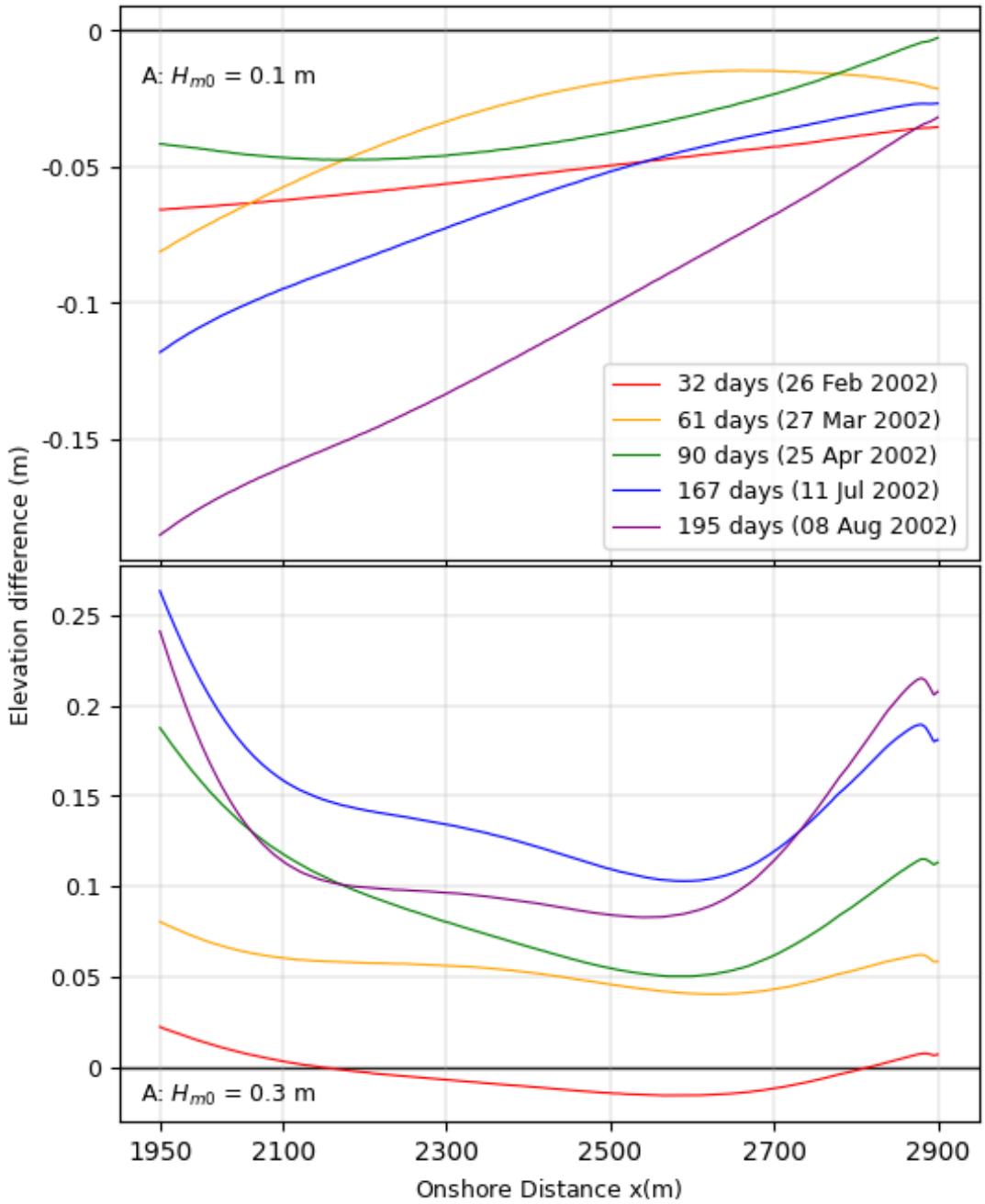


Figure 5.13: Deviation of computed mudflat profile from fitted profile at time $t$ = 32, 61, 90, 167 and 195 days during A interval for $H_{m0}$ = 0.1 and 0.3 m

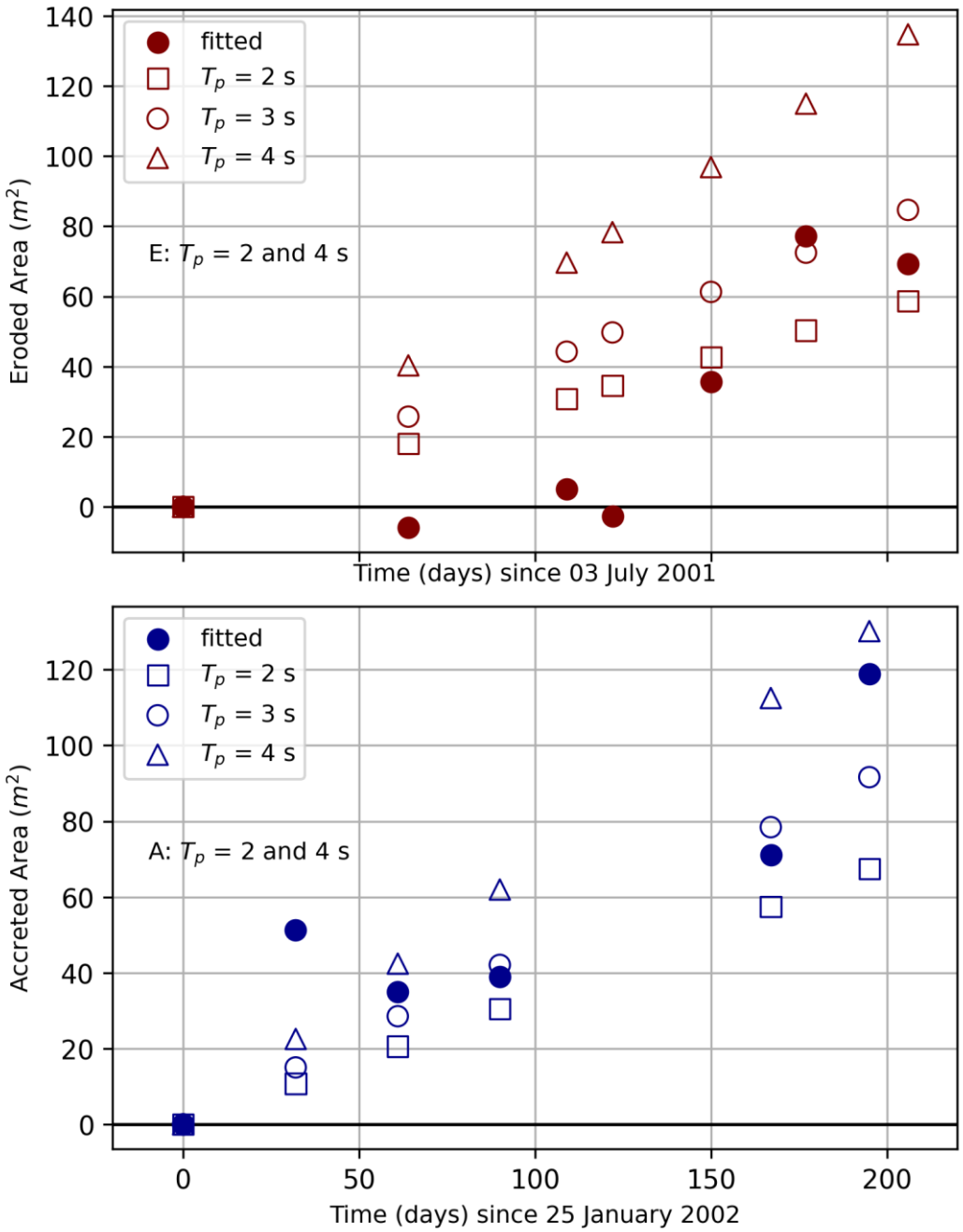


Figure 5.14: Comparison of fitted and computed eroded areas (negative implies net accretion) during E interval (top) and accreted areas during A interval (bottom) for wave period $T_p$ = 2, 3 and 4 s

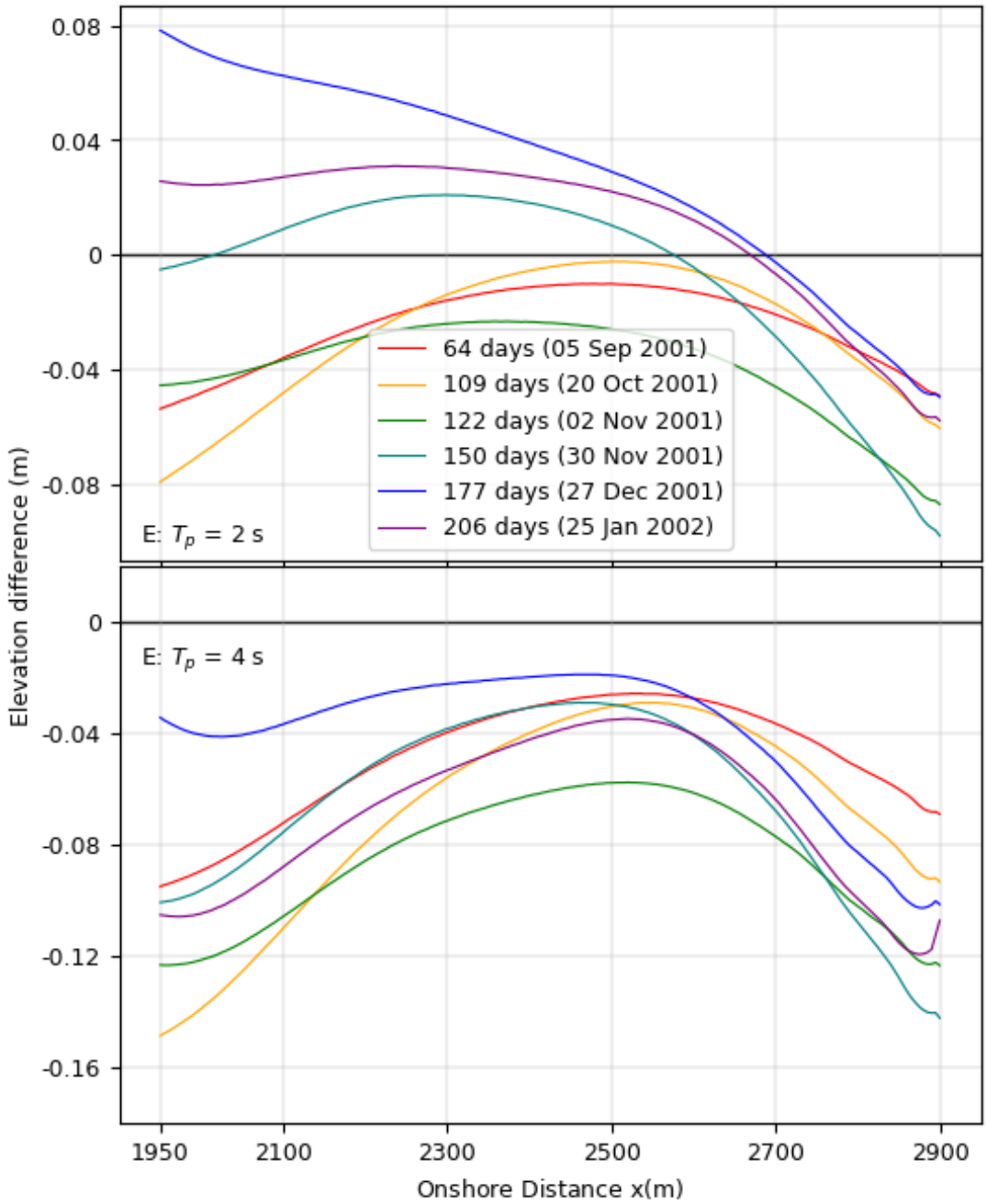


Figure 5.15: Deviation of computed mudflat profile from fitted profile at time $t$ = 64, 109, 122, 150, 177 and 206 days during E interval for $T_p$ = 2, and 4 s

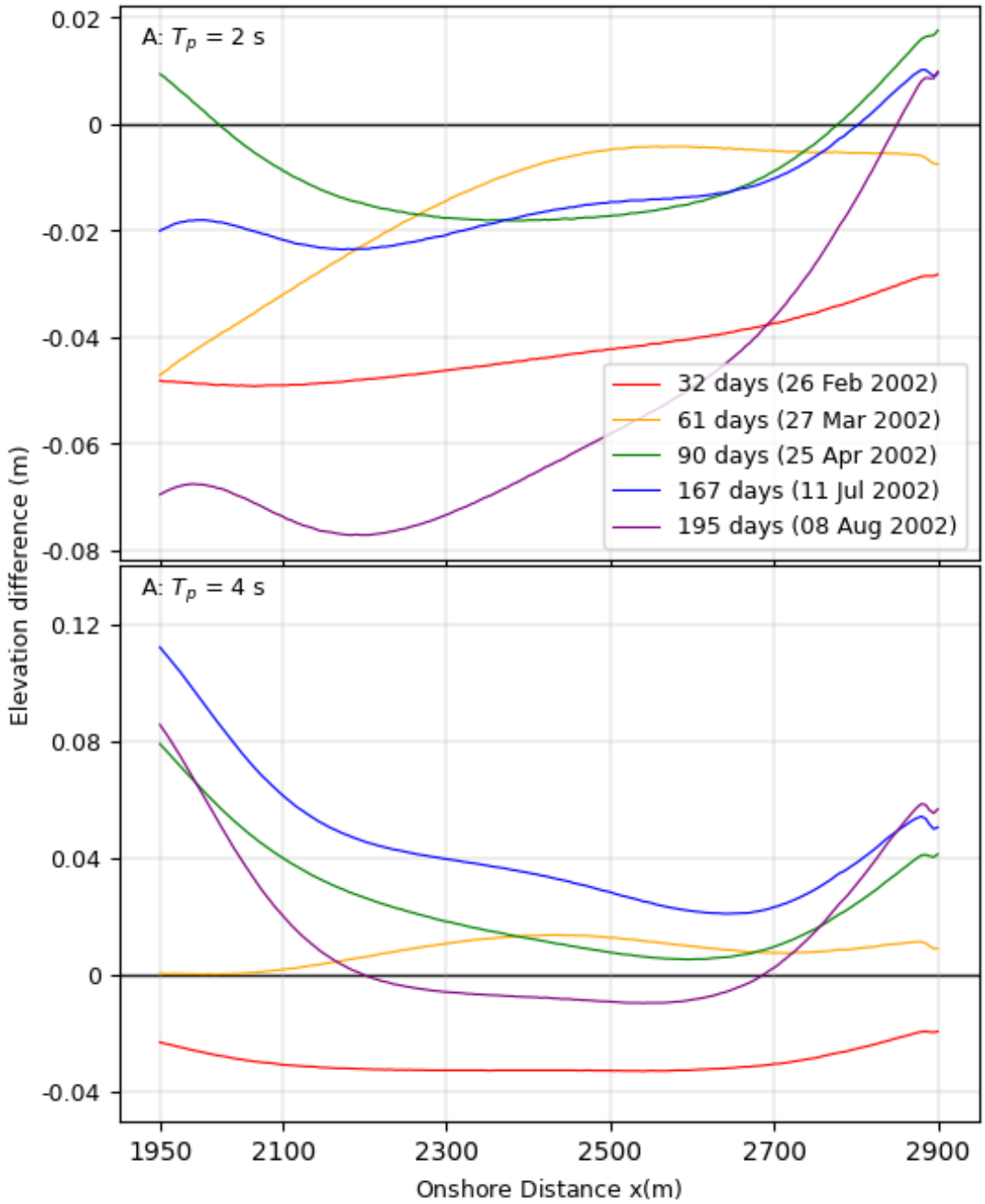


Figure 5.16: Deviation of computed mudflat profile from fitted profile at time $t$ = 32, 61, 90, 167 and 195 days during A interval for $T_p$ = 2, and 4 s

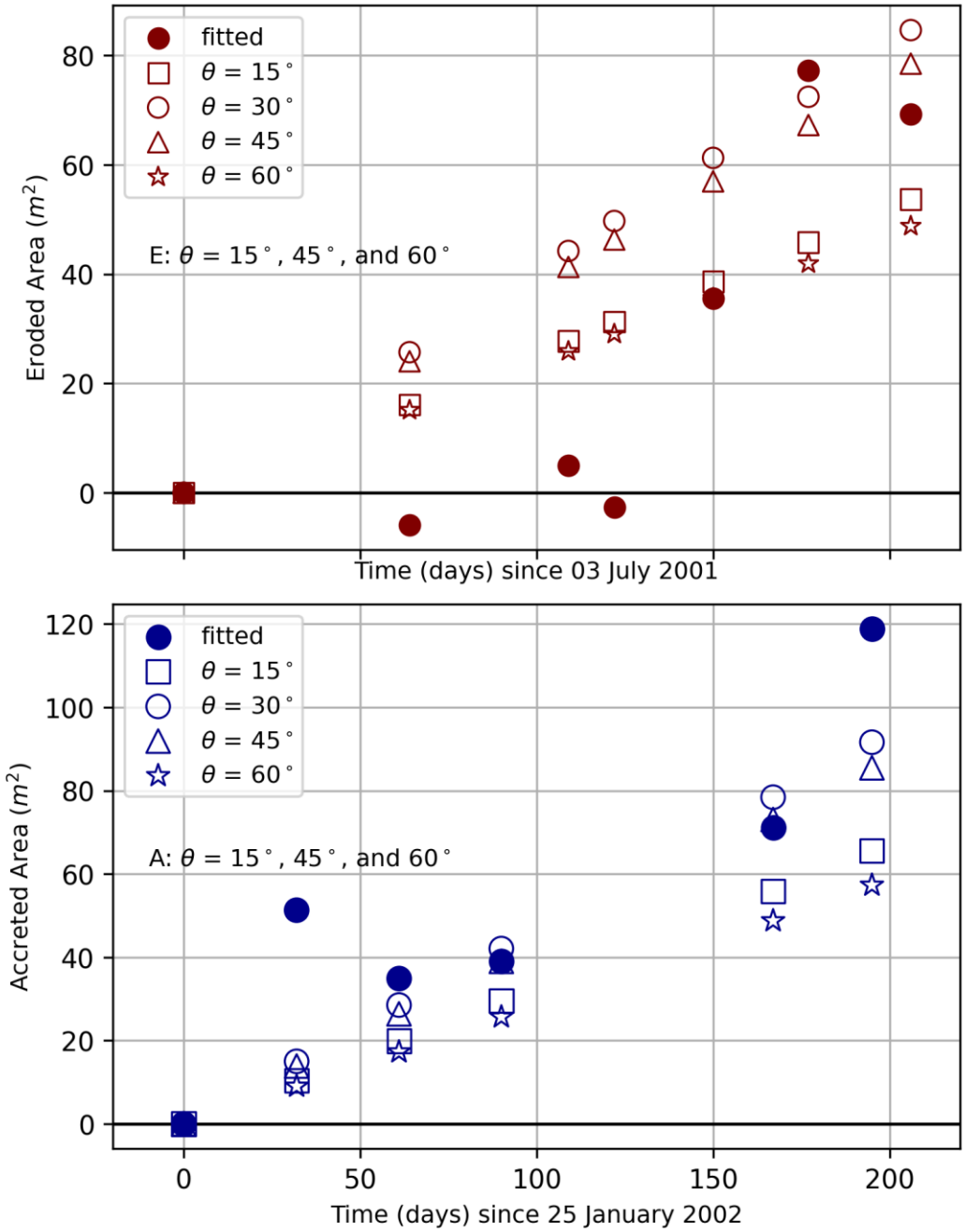


Figure 5.17: Comparison of fitted and computed eroded areas (negative implies net accretion) during E interval (top) and accreted areas during A interval (bottom) for wave angle $\theta$ = 15°, 30°, 45°, and 60°

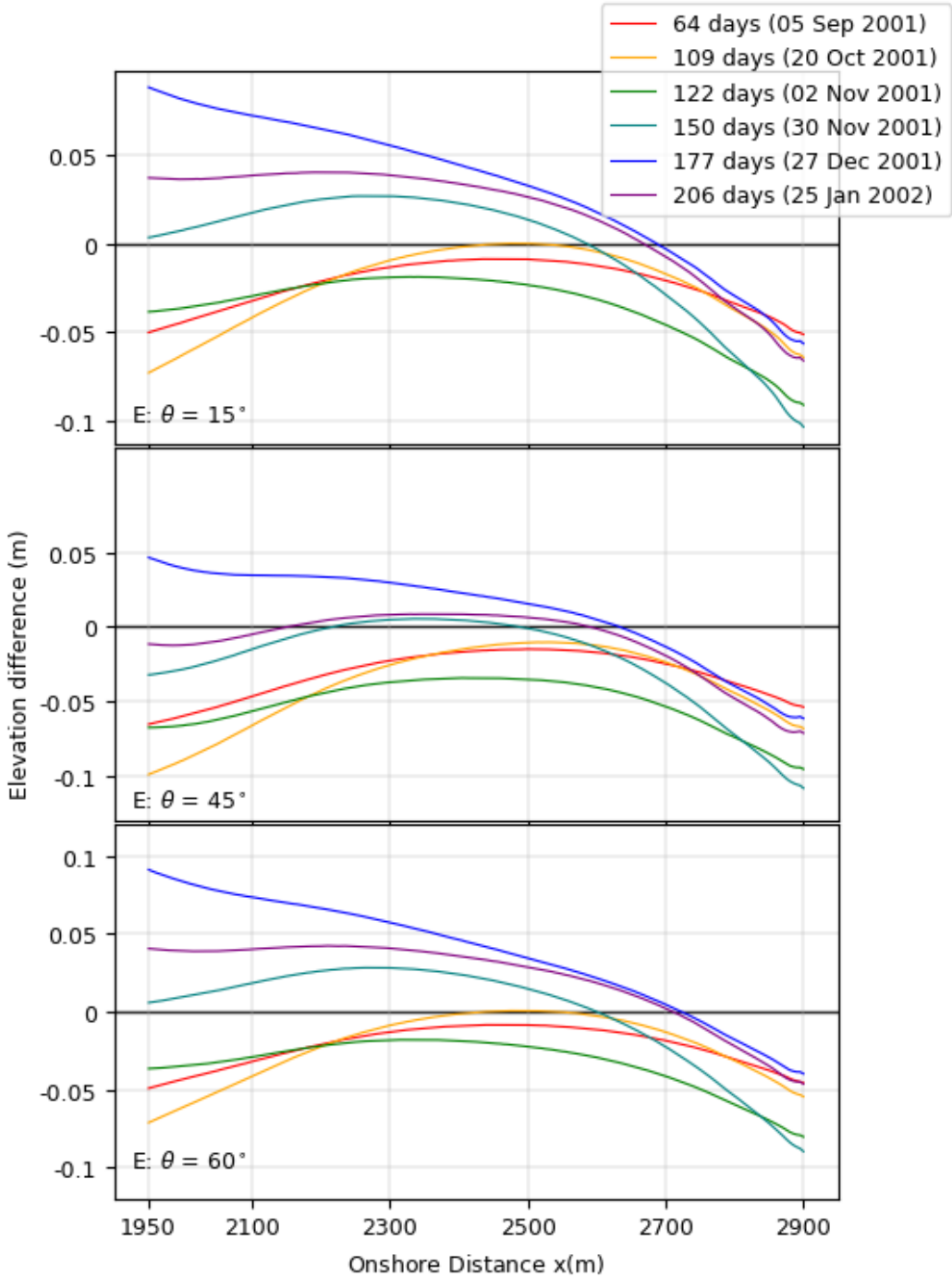


Figure 5.18: Deviation of computed mudflat profile from fitted profile at time $t$ = 64, 109, 122, 150, 177 and 206 days during E interval for $\theta$ = 15°, 45°, and 60°

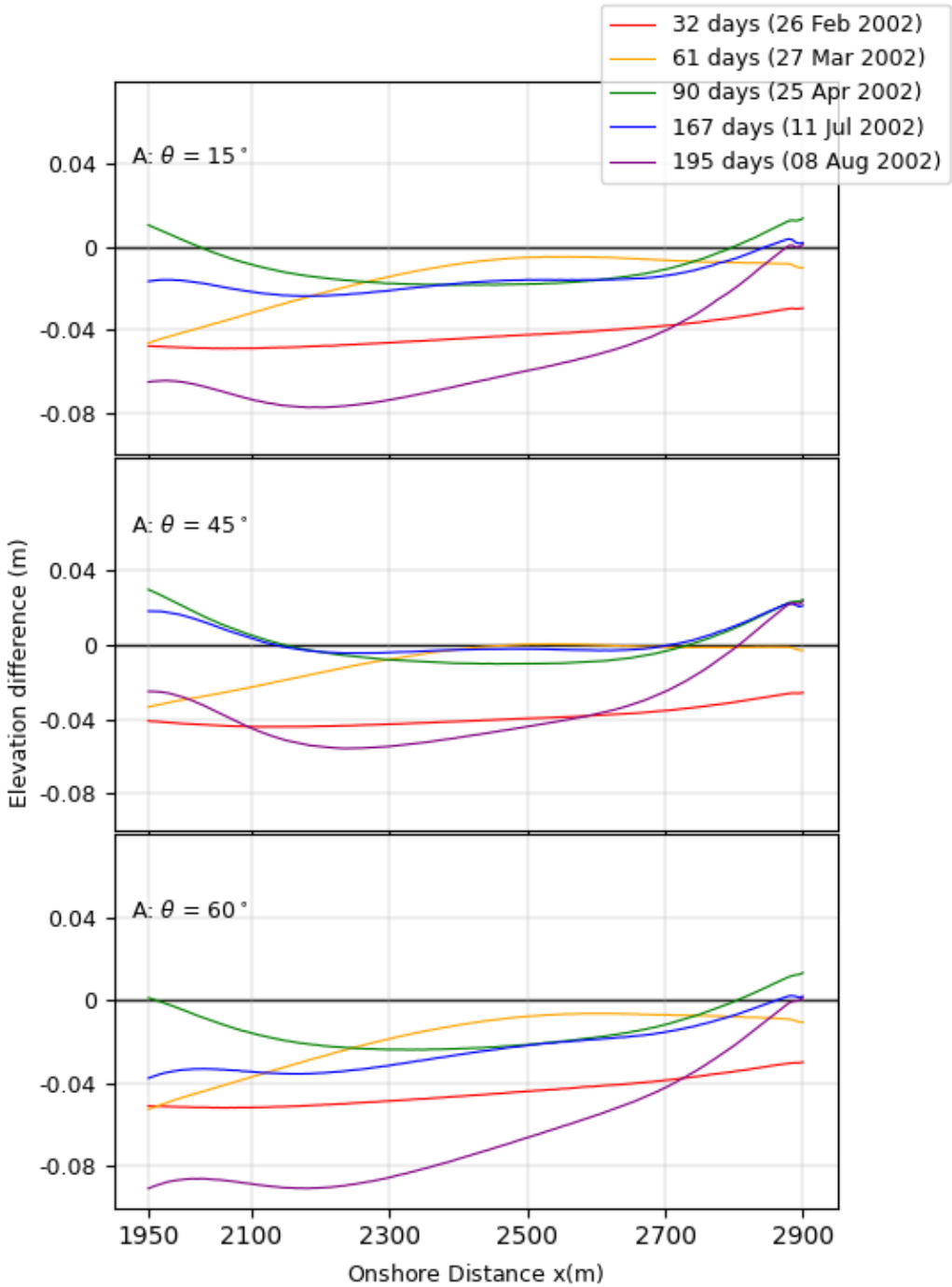


Figure 5.19: Deviation of computed mudflat profile from fitted profile at time $t$ = 32, 61, 90, 167 and 195 days during A interval for $\theta$ = 15°, 45°, and 60°

# Chapter 6

# OTHER EFFECTS ON MUDFLAT PROFILE CHANGES

The CSHORE calibrated for the E and A intervals was used to examine the effects of changing other parameters on the mudflat profile evolution. The following sections tested the mudflat profile shape in Eq. (1), the alongshore water level gradient $S_y$ in Eq. (4), and the wind shear stress in Eqs. (3) and (4).

## 6.1 Initial Profile Shape

Fig. 6.1 presents the initial convex profile based on the parameters in Tables 2.1 and 2.2 together with a hypothetical profile created by changing the sign of the convexity parameter $a$ while parameters $b$ and $c$ were selected to maintain same profile elevations at $x$ = 0 and 3,000 m.

Lee and Mehta (1997) examined the relationship between profile shape and wave forcing under normally incident waves. For this study, the computation of the basic case using the parameters in Table 3.1 was applied to the concave profile. The results were examined to quantify the effect of initial profile shape on computed profile changes.

The computed final profiles were compared with their corresponding initial profiles to obtain the computed erosion/accretion height for the E and A intervals, respectively, in Fig. 6.2. Wave breaking shifted landward on the concave profile and a larger erosion/accretion occurred in a narrower zone. Both intervals have an increase in computed erosion/accretion height of about 0.1 m.

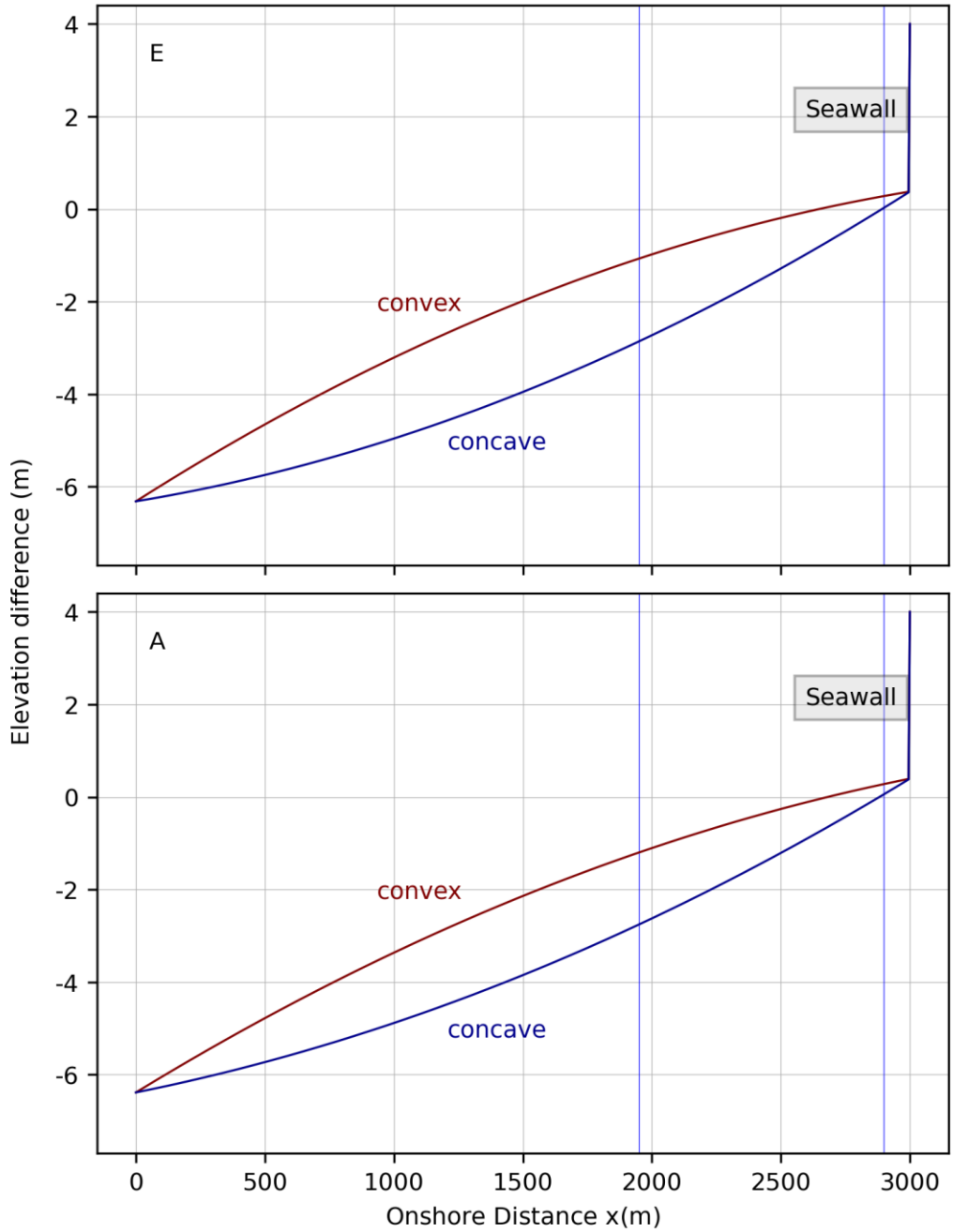


Figure 6.1: Convex initial profile with positive $a$ on 3 July 2001 for E (top) and 25 January 2002 for A (bottom) intervals and hypothetical concave profile with negative $a$ for same elevation at $x$ = 0 and 3,000 m

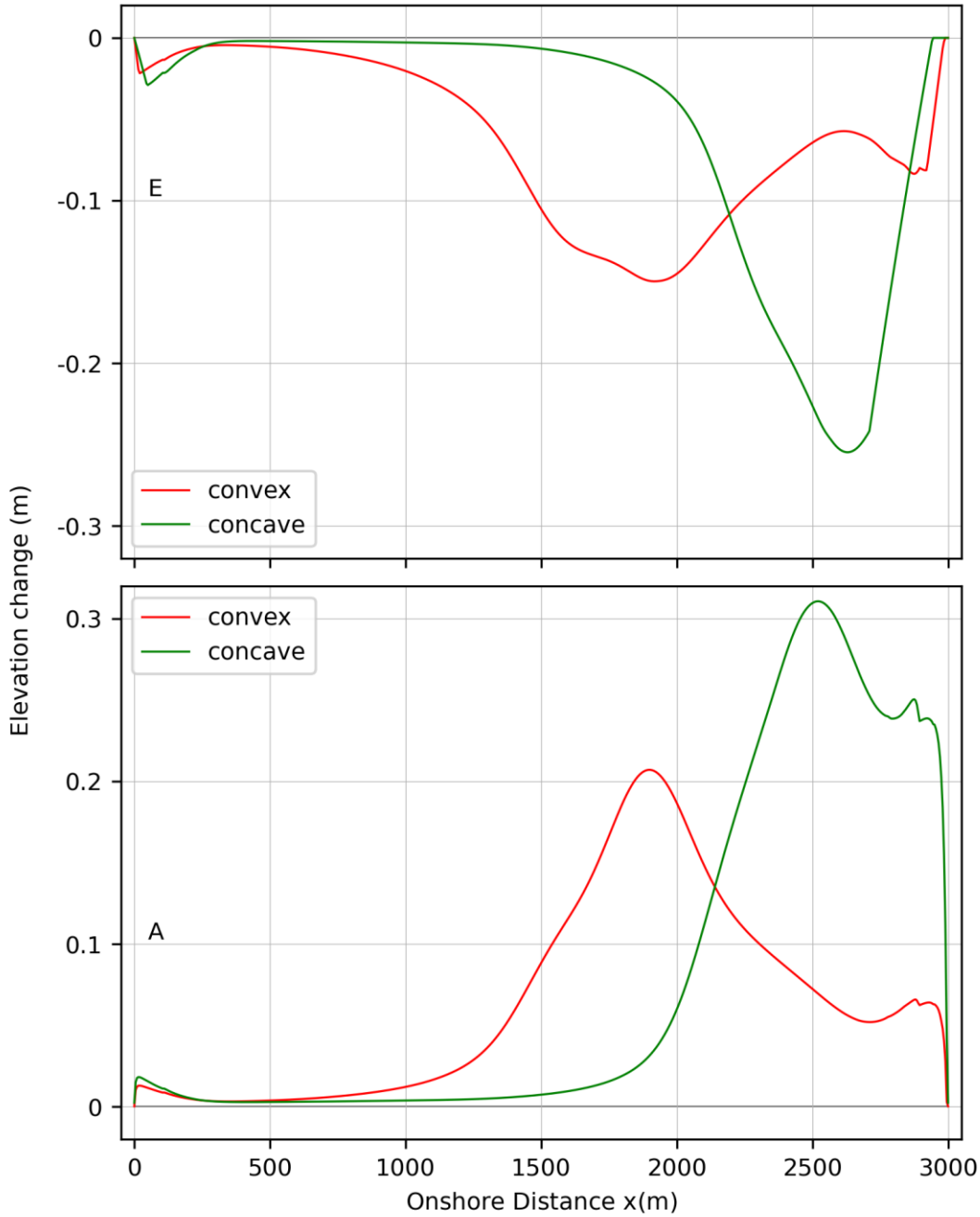


Figure 6.2: Computed mudflat elevation changes relative to the initial convex and concave profile at the end of the E (top) and A (bottom) intervals

## 6.2 Alongshore Water Level Gradient

Yamada et al. (2012) measured the southern longshore current and mud transport on the mudflat. It was estimated that the alongshore water level gradient was in the order of $10^{-6}$ or a water level difference of 1 mm over an alongshore distance of 1 km. This was the necessary gradient to produce a longshore current in the order of 0.1 $\mathrm{m/s}$. For their analysis, wind waves were not considered because the velocity and mud concentration measurements were limited to a depth of 0.3 m.

The basic case was recalculated with $S_y$ = –$10^{-6}$ in Eq. (4) where a negative $S_y$ increases the southward longshore current $\bar{V}$. The alongshore pressure gradient term in Eq. (4) became non-negligible in larger water depths with little wave breaking and wave-induced longshore current was negligible. The initial computed profile changes for the E and A intervals turned out to be too large and was reduced by a factor of about 4 by replacing $y_e$ = $\pm$100 with $\pm$400.

Fig. 6.3 presents the elevation difference between the initial and final computed profiles at the end of the E (top) and A (bottom) intervals for the case of IAWLG = 0 and 1. IAWLG = 0 corresponds to the case of no alongshore water level gradient or $S_y$ = 0 and $y_e$ = $\pm$100 m while IAWLG = 1 refers to the case where $S_y$ = – $10^{-6}$ and $y_e$ = $\pm$400 m.

Fig. 6.4 shows agreement is similar after the adjustment of the equivalent alongshore length $y_e$. For IAWLG = 1, erosion and accretion were too large near the seawall however, in reality, the value of $S_y$ is expected to vary with time and along the cross-shore line. The calibrated value of $y_e$ depends on the alongshore momentum equation used to compute the alongshore current $\bar{V}$.

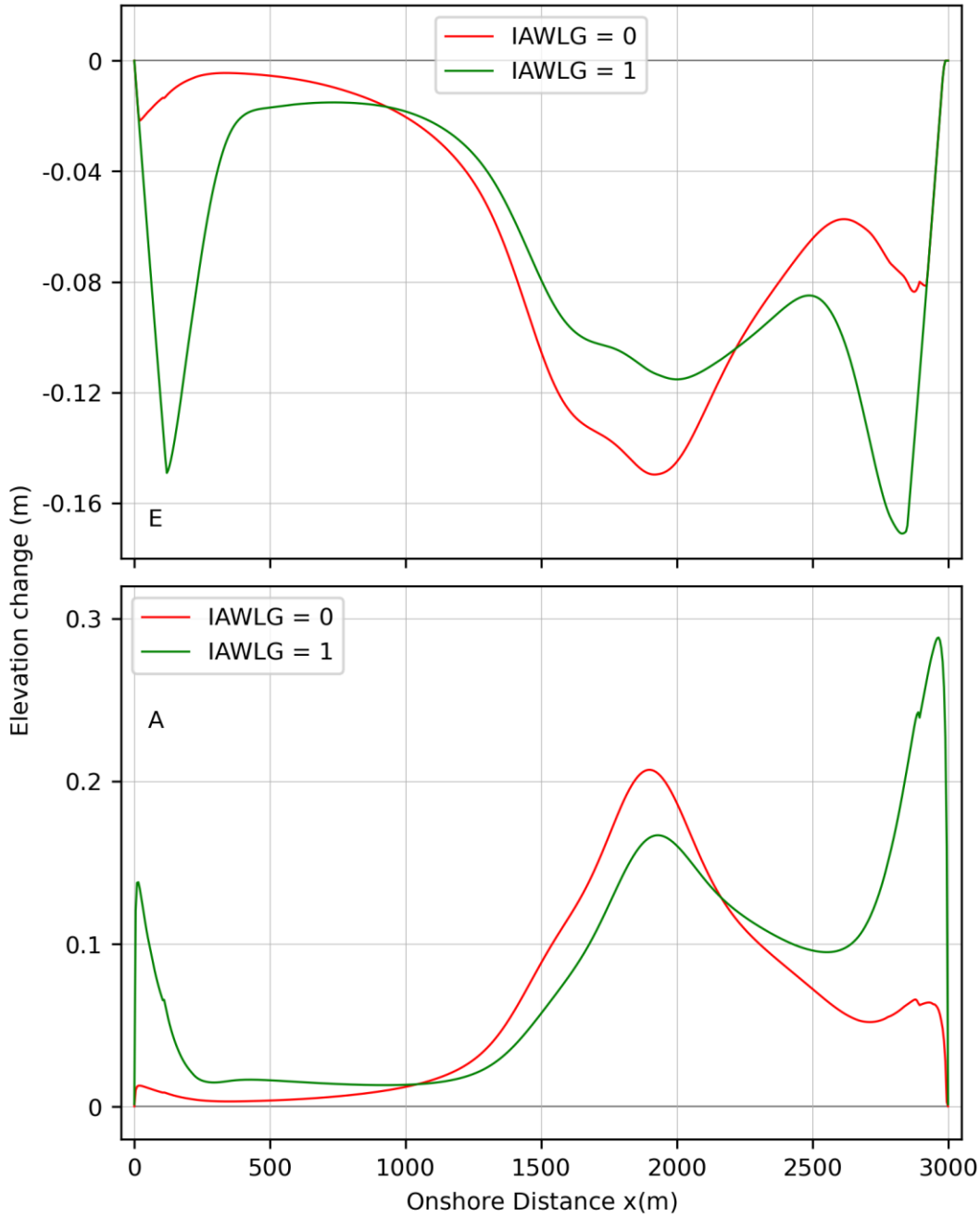


Figure 6.3: Computed mudflat elevation changes relative to the initial profile at the end of the E (top) and A (bottom) intervals for two cases of IAWLG = 0 and 1

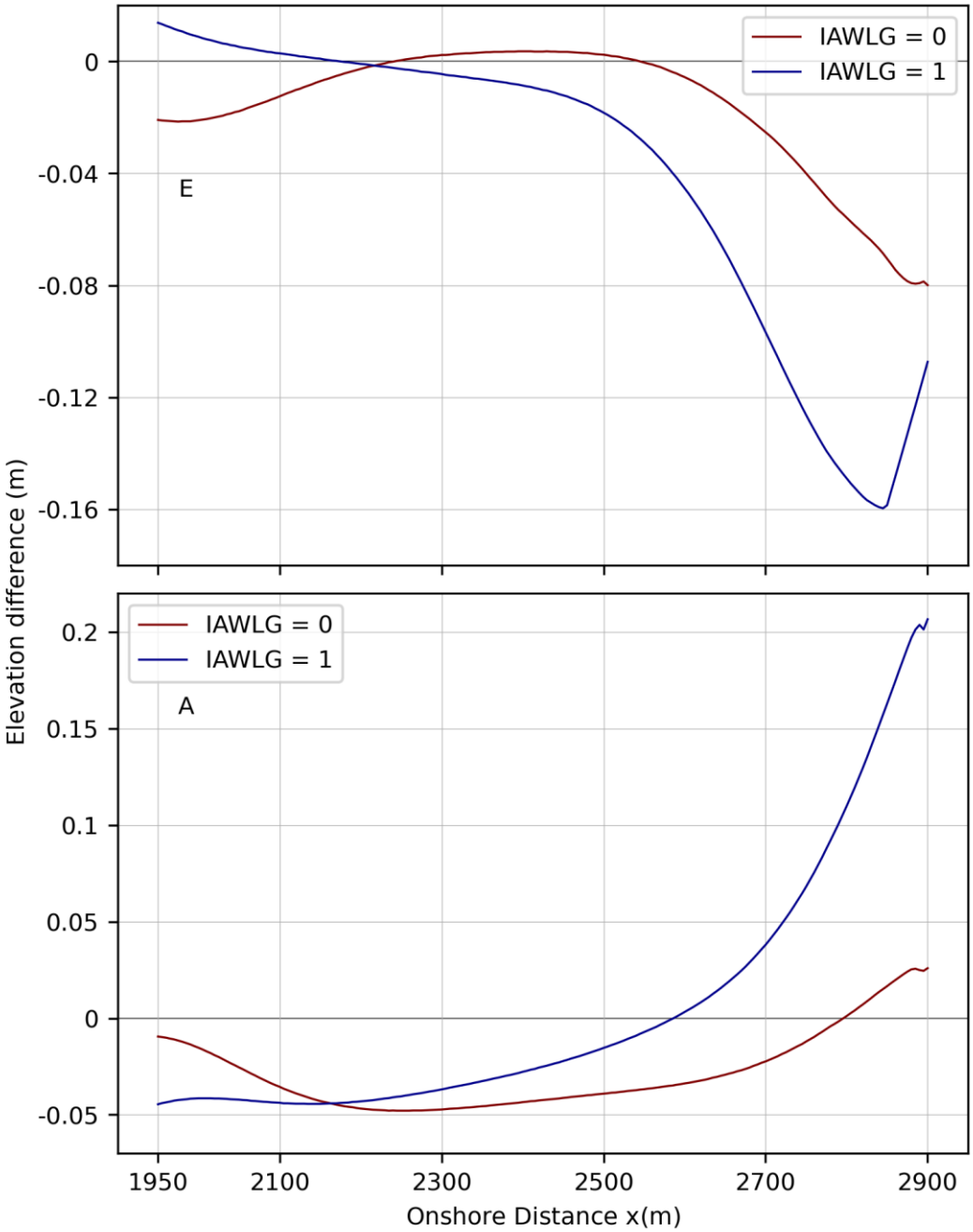


Figure 6.4: Deviation of computed final mudflat profile from fitted final profile at the end of E (top) and A (bottom) intervals for IAWLG = 0 and 1

## 6.3 Wind Shear Stresses

Finally, the effects of wind stresses were examined. The wind stresses were estimated using the average wind speed $W_{10}$ = 5 m/s and the wind direction $\theta$ = 30° (same as the wave direction).

The cross-shore wind stress $\tau_{sx}$ in Eq. (3) increased the mean water level $\bar{\eta}$ slightly however, the water level variation was dominated by the semidiurnal tide at this site.

The longshore wind stress $\tau_{sy}$ in Eq. (4) with no alongshore water level gradient was positive for $\theta$ = 30° which increased the southward longshore current $\bar{V}$. The value of $\tau_{sy}$ was constant unlike the term involving $S_y$ which was proportional to mean depth $\bar{h}$.

Similar to the case IAWLG = 1, the value of $y_e$ was adjusted from $\pm$100 m to $\pm$400 m to improve the agreement of the computed and fitted profiles. Figs. 6.5 and 6.6 showed the agreement is similar for both IWIND = 0 and 1, without and with wind stress, respectively, after adjusting the equivalent alongshore length $y_e$ by a factor of 4. The erosion and accretion close to the seawall was still too large.

In reality, the wind direction varies more than the wave direction. Because of this variability, the wind effect on the mudflat profile change is expected to be more subdued.

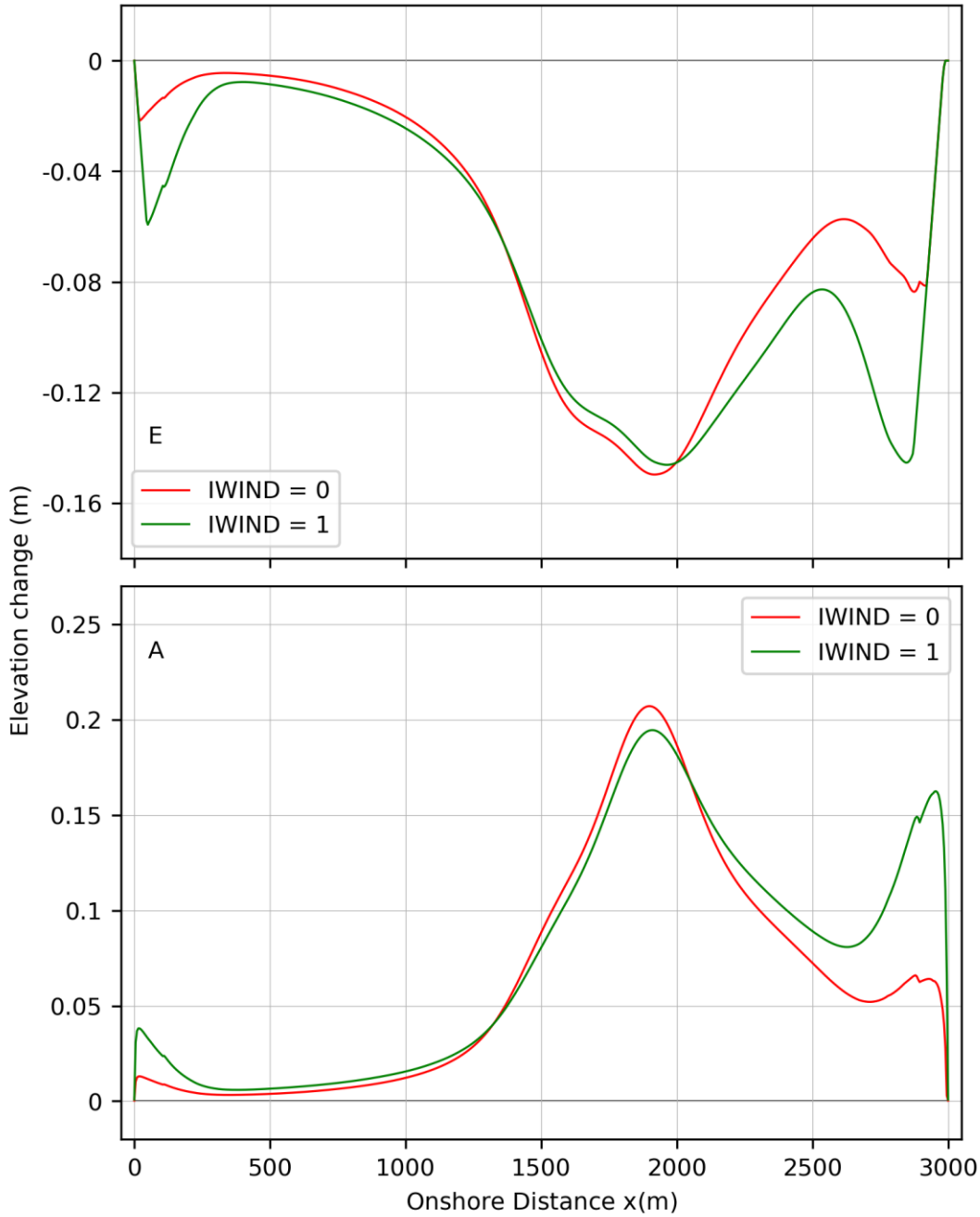


Figure 6.5: Computed mudflat elevation changes relative to the initial profile at the end of the E (top) and A (bottom) intervals for IWIND = 0 and 1

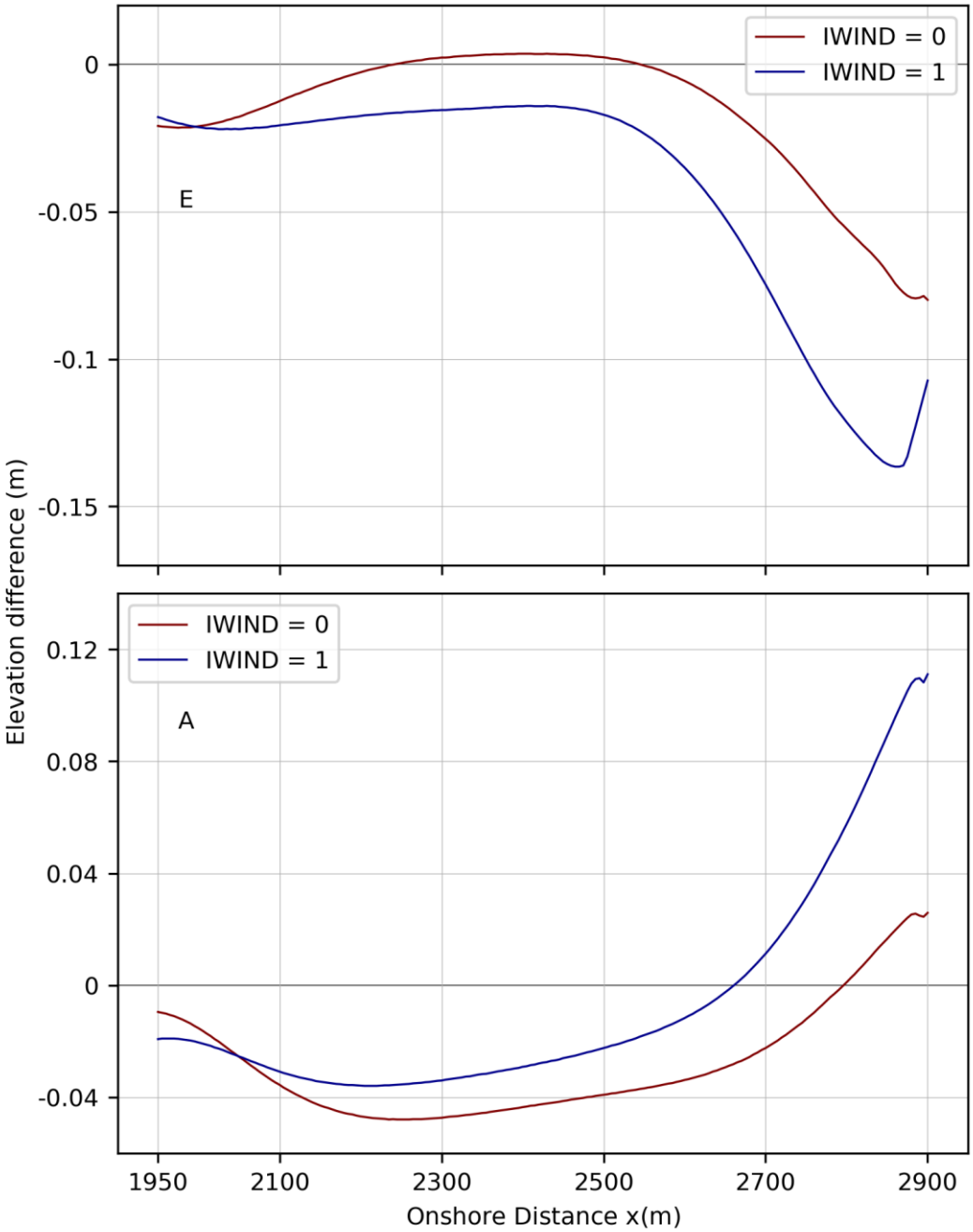


Figure 6.6: Deviation of computed final mudflat profile from fitted final profile at the end of E (top) and A (bottom) intervals for IWIND = 0 and 1

# Chapter 7

# CONCLUSIONS

The profile evolution of an intertidal mudflat under a semidiurnal tide range of almost 3 m and wind waves of about 0.2 m was examined using available data and the cross-shore numerical model CSHORE which was extended for a mixture of sand and mud. The mudflat profile changed by about 0.1 m during both the erosion and accretion intervals. The change coincided with the yearly water level variation of about 0.4 m meaning as the water level decreased or increased during the erosion or accretion interval, the profile eroded or accreted, respectively.

The extended CSHORE was applied to predict the cross-shore and longshore sediment (sand and mud) transport rates on the mudflat. The hourly sediment transport rates were affected by sediment suspension due to breaking waves in the surf zone, and by suspended sediment transport by semidiurnal tide currents. The semidiurnal migration of the still water shoreline and surf zone was resolved numerically to predict the net cross-shore and longshore sediment transport rates influenced by the cross-shore (undertow) and longshore currents induced by breaking waves.

To reproduce the erosion and accretion of the profile, the alongshore sediment loss or gain was included. An equivalent alongshore length associated with alongshore sediment gradient was calibrated. The calibration of the equivalent alongshore length is the major limitation of the numerical model.

The calibrated CSHORE was used to examine the sensitivity of the computed profile change to each input parameter.

The effective mud fall velocity and mud volume fraction affected the suspended mud volume and transport rate on the mudflat. A higher mud fall velocity resulted in lower transport rates. Similarly, a lower mud volume fraction produces lower transport rates. Mud characteristics are important but may be difficult to specify due to their spatial variation.

The yearly water level variation must have influenced sediment exchanges between the mudflat and adjacent river mouth. The direct effect of a yearly water level variation on the sediment transport along the surveyed profile line was computed to be negligible. The semidiurnal tide amplitude determined the intertidal zone and the surf zone of wave breaking on the mudflat in front of a seawall at this site. A smaller tide amplitude resulted in more wave breaking which drove sediment transport.

The incident wave height, period, and direction influence wave transformation, breaking, and wave-induced currents. The explicit effect of wave height and period on wave breaking and therefore, on sediment transport were evident. However, the effect of wave direction was less pronounced. The uncertainty associated with wave angle input for the numerical model is not critical.

Both tides and waves are important but their time series for long-term computations may not be available. In addition, alongshore water level gradient and wind stresses are not negligible in the momentum equations involving radiation stresses in CSHORE. These neglected effects significantly modify longshore current and ultimately, sediment transport. The calibrated equivalent alongshore length needs to be adjusted when these neglected effects are included.

The cumulative effects of the relatively small forcing terms are difficult to predict accurately and consistently. While surf zone of relatively small breaking waves

is not resolved in regional models, sediment transport in the surf zone can be important for mudflat profile evolution.

## REFERENCES


Dean, R. G., and R. A. Dalrymple. 2001. In *Coastal Processes with Engineering Applications* Cambridge University Press.

Do, K., N. Kobayashi, and K.-D. Suh. 2012. "Erosion and accretion on curved beach." In *Coastal Engineering*, edited by P. Lynett and J. M. Smith, 1–12. Reston, VA.: ASCE.

Farhadzadeh, A., N. Kobayashi, and M. B. Gravens. 2012. "Effect of breaking waves and external current on longshore sediment transport." *Journal of Waterway, Port, Coastal, and Ocean Engineering*, 138(3): 256–260. http://doi.org/10.1061/(asce)ww.1943-5460.0000123.

Friedrichs, C. T., and D. G. Aubrey. 1996. "Uniform bottom shear stress and equilibrium hyposometry of intertidal flats." In *Mixing in Estuaries and Coastal Seas*, edited by C. Pattiaratchi, 405–429. Washington, D.C: American Geophysical Union.

Giardino, A., E. Ibrahim, S. Adam, E. A. Toorman, and J. Monbaliu. 2009. "Hydrodynamics and cohesive sediment transport in the IJzer estuary, Belgium: case study." *Journal of Waterway, Port, Coastal, and Ocean Engineering*, 135(4): 176–184. http://doi.org/10.1061/(asce)0733-950x(2009)135:4(176).

Harris, C. K., C. R. Sherwood, R. P. Signell, A. J. Bever, and J. C. Warner. 2008. "Sediment dispersal in the northwestern Adriatic Sea." *Journal of Geophysical Research: Oceans*, 113(11): 1–18. http://doi.org/10.1029/2006JC003868.

Kobayashi, N. 2013. "Cross-shore numerical model CSHORE 2013 for sand beaches and coastal structures." *Research Report. No. CACR-13-01*. Newark, DE.: Center for Applied Coastal Research, University of Delaware.

Kobayashi, N. 2016. "Coastal sediment transport modeling for engineering applications." *Journal of Waterway, Port, Coastal, and Ocean Engineering*, 142(6): 03116001. http://doi.org/10.1061/(asce)ww.1943-5460.0000347.

Kobayashi, N., and H. Jung. 2012. “Beach erosion and recovery.” *Journal of Waterway, Port, Coastal, and Ocean Engineering*, 138(6): 473–483. http://doi.org/10.1061/(asce)ww.1943-5460.0000147.

Large, W. G., and S. Pond. 1981. “Open ocean momentum flux measurements in moderate to strong winds.” *Journal of Physical Oceanography*, 11(3): 324–336. http://doi.org/10.1175/1520-0485(1981)011<0324:OOMFMI>2.0.CO;2.

Lee, S.-C., and A. J. Mehta. 1997. “Problems in characterizing dynamics of mud shore profiles.” *Journal of Hydraulic Engineering*, 123(4): 351–361. http://doi.org/10.1061/(asce)0733-9429(1997)123:4(351).

McAlpin, J., C. Ross, and J. McKnight. 2019. “Houston ship channel and vicinity three- dimensional adaptive hydraulics ( AdH ) numerical model calibration / validation report.” *Report No. ERDC/CHL TR-19-10*. Vicksburg, MS: US Army Corp of Engineers, Coastal and Hydraulics Laboratory.

McAnally, W. H., A. J. Mehta, and A. J. Manning. 2021. “Observations on floc settling velocities in the Tamar estuary, United Kingdom.” *Journal of Waterway, Port, Coastal, and Ocean Engineering*, 147(5): 04021015. http://doi.org/10.1061/(asce)ww.1943-5460.0000649.

Pritchard, D., and A. J. Hogg. 2003. “Cross-shore sediment transport and the equilibrium morphology of mudflats under tidal currents.” *Journal of Geophysical Research*, 108(C10): 3313. http://doi.org/10.1029/2002JC001570.

Roberts, W., P. Le Hir, and R. J. S. Whitehouse. 2000. “Investigation using simple mathematical models of the effect of tidal currents and waves on the profile shape of intertidal mudflats.” *Continental Shelf Research*, 20(10–11): 1079–1097. Pergamon. http://doi.org/10.1016/S0278-4343(00)00013-3.

Shi, B., J. R. Cooper, P. D. Pratolongo, S. Gao, T. J. Bouma, G. Li, C. Li, S. L. Yang, and Y. P. Wang. 2017. “Erosion and accretion on a mudflat: the importance of very shallow-water effects.” *Journal of Geophysical Research: Oceans*, 122(12): 9476–9499. http://doi.org/10.1002/2016JC012316.

USACE. 2003. “Coastal engineering manual” Washington, D.C: U.S. Army Corps of Engineers.

Uzaki, K., and Y. Kuriyama. 2009. “Development of the three-dimensional numerical model of sediment transports and topographic changes of intertidal flats due to sands and cohesive sediments generated by tidal currents and wave-induced currents and an application to the field.” *Report of the Port and Airport Research Institute*. Yokosuka, Japan: Port and Airport Research Institute.

Yamada, F., and N. Kobayashi. 2003. "Parameterization of mudflat profile changes caused by seasonal tide level variations." *Research Report. No. CACR-03-02*. Newark, Delaware: Center for Applied Coastal Research, University of Delaware.

Yamada, F., and N. Kobayashi. 2004. "Annual variations of tide level and mudflat profile." *Journal of Waterway, Port, Coastal, and Ocean Engineering*, 130(3): 119–126. http://doi.org/10.1061/(asce)0733-950x(2004)130:3(119).

Yamada, F., N. Kobayashi, Y. Shirakawa, and Y. Sakanishi. 2011. "Sediment budgets based on the mass of silt and clay on intertidal flat adjacent to river mouth." In *Coastal Engineering*, edited by P. Lynett and J. M. Smith, 1–13. Reston, VA.: ASCE.

Yamada, F., N. Kobayashi, Y. Shirakawa, Y. Watabe, S. Sassa, and A. Tamaki. 2012. "Effects of Tide and River Discharge on Mud Transport on Intertidal Flat." *Journal of Waterway, Port, Coastal, and Ocean Engineering*, 138(2): 172–180. http://doi.org/10.1061/(asce)ww.1943-5460.0000108.

Zhu, T., and N. Kobayashi. 2021. "Modeling of Soft Cliff Erosion by Oblique Breaking Waves during a Storm." *Journal of Waterway, Port, Coastal, and Ocean Engineering*, 147(4): 1–8. http://doi.org/10.1061/(asce)ww.1943-5460.0000642.